CR 151216

(NASA-CR-151216) ASSESSMENT OF ANALYTICAL TECHNIQUES FOR PREDICTING SOLID PROPELLANT EXHAUST PLUMES AND PLUME IMPINGEMENT ENVIRONMENTS (Lockheed Missiles and Space Co.) 137 p HC A07/MF A01 CSCL 21H G3/20

N77-19164

Unclas
20497

MAR 1977
RECEIVED
NASA STI FACILITY
INPUT BRANCH

LMSC-HREC TR D497079

Lockheed
Missiles & Space Company, Inc.
HUNTSVILLE RESEARCH & ENGINEERING CENTER

Cummings Research Park
4800 Bradford Drive,
Huntsville, Alabama

ASSESSMENT OF ANALYTICAL TECHNIQUES FOR PREDICTING SOLID PROPELLANT EXHAUST PLUMES AND PLUME IMPINGEMENT ENVIRONMENTS

January 1977

Contract NAS9-14845

Prepared for National Aeronautics and Space Administration
Lyndon B. Johnson Spacecraft Center, Houston, Texas 77058

by

James A. Tevepaugh
Sheldon D. Smith
Morris M. Penny

APPROVED: Morris Penny
John W. Benefield, Supervisor
Advanced Systems Technology Section

J. S. Farrior
J.S. Farrior
Resident Director

FOREWORD

This document presents the results of an analysis performed by personnel of the Lockheed-Huntsville Research & Engineering Center for the Aerodynamic Systems Analysis Section of the NASA-Johnson Space Center, Houston, Texas, under the direction of Barney B. Roberts (Contract NAS9-14845). The work was performed in support of Space Shuttle exhaust plume analyses.

ACKNOWLEDGMENT

The authors are grateful to Dr. Terry F. Greenwood and Mr. David Seymour of Marshall Space Flight Center for their contributions to this study.

SUMMARY

Results are presented of an analysis of experimental nozzle, exhaust plume and exhaust plume impingement data. The data were obtained for subscale solid propellant motors with propellant Al loadings of 2, 10 and 15% exhausting to simulated altitudes of 50,000, 100,000 and 112,000 ft. Analytical predictions were made using a fully coupled two-phase method-of-characteristics numerical solution and a technique for defining thermal and pressure environments experienced by bodies immersed in two-phase exhaust plumes.

Comparisons of experimentally measured and analytically predicted nozzle wall static pressures are presented for each propellant Al loading. Radial distributions of pitot pressure and heating rates measured experimentally at axial stations of $x/D_{exit} = 5$, 12, 16 and 20 are compared with analytical predictions. Experimental plume impingement pressures and energy fluxes were obtained for a flat plate immersed in the exhaust plumes at various angles of attack and centered at axial stations of $x/D_{exit} = 5$, 12 and 20. Analytical predictions of the thermal and pressure environments on the flat plate are compared with the experimental data.

The validity of the empirical data input to the analytical calculations is investigated. The effects of mass mean particle size, particle size distribution and particle drag model on the comparison of experimental and analytical exhaust plume data are presented. Requirements for the adequate thermochemical modeling of two-phase nozzle and exhaust plume expansions are discussed.

CONTENTS

NOMENCLATURE

Symbol	Definition
C_p	gas specific heat at constant pressure
D	diameter
h	static enthalpy
H	total enthalpy
P	pressure
Pr	Prandtl number
$\dot{q}$	gas heating rate
R	radial distance from nozzle centerline
V	gas velocity
x	axial distance from nozzle exit plane
Y	distance along centerline of flat plate from center of plate
ρ	density
ϕ	ratio of the product of density and viscosity at the onset of chemical dissociation to the product of density and viscosity at the surface of the impinged body
ψ	flat plate inclination angle to the nozzle centerline
μ	viscosity

Subscripts

c	combustion chamber
d	chemical dissociation
exit	nozzle exit plane
p	particle
s	stagnation
w	surface of impinged body

1. INTRODUCTION

The Space Shuttle launch vehicle utilizes two large solid propellant rocket boosters and eight solid propellant motors mounted on each booster to effect separation of the spent booster stages from the orbiter vehicle. Launch vehicle aerodynamic tests have shown that the booster exhaust plumes significantly affect the vehicle aerodynamics. The exhaust plumes induce separation of the boundary layer from the orbiter vehicle, thus producing an adverse pressure gradient on the orbiter vehicle control surfaces. Aerodynamic control capability of the launch vehicle is reduced. During the staging sequence, exhaust plumes from the booster separation motors impinge on the orbiter fore and aft surfaces and the orbiter external fuel tank. Impinged surfaces are subjected to adverse and potentially damaging pressure and thermal environments. To obtain data for use in design applications, these aspects of the launch sequence have received considerable attention in test programs and analytical studies.

Numerical solutions have been developed to calculate the exhaust plume flow fields of solid propellant rocket motors and the pressure and thermal environments experienced by bodies immersed in these two-phase plumes. These numerical solutions are incorporated in the Lockheed-Huntsville RAMP computer code (Ref. 1). The RAMP code was developed by extending an existing nozzle-exhaust plume solution to include the treatment of two-phase flows. Modeling of two-phase effects relied heavily on the previous work of Kliegel, which has been extended (Ref. 1) to include reacting gas chemistry. Solid particle data used in the two-phase analysis are empirical and were developed primarily for nozzle performance applications. Since the RAMP computer code is being used to specify Space Shuttle design criteria, it was necessary to confirm the validity and accuracy of the code's empirical input data and calculational scheme.

Previous experimental measurements of gasdynamic properties in solid propellant rocket exhaust plumes were insufficient in quantity and quality to provide the necessary experimental data base. A test program was conceived to provide the necessary experimental data. Analysis of the test program data was intended to accomplish the following:

- Confirm the RAMP numerical flowfield solution
- Confirm the analytical thermochemical model
- Validate the solid particle empirical input data
- Validate the two-phase plume impingement model.

The test program used subscale solid propellant rocket motors with operating parameters (area ratio, propellant aluminum loading, etc.) typical of full-scale applications. Rocket motor operating parameters and test measurements were parametrically varied to provide a coherent but diverse data base. Multiple rocket firings were performed for each test condition to confirm experimental repeatability and raise the confidence level of the data.

The post-test analysis was organized to first confirm the RAMP exhaust plume model by comparison of analytical data with experimentally measured pitot pressures at various axial and radial locations. Exhaust plume impingement calculations using the Lockheed PLIMP computer code (Ref. 2) were then verified by comparison with experimentally measured impingement pressures and heating rates on a flat plate immersed in the solid propellant exhaust plumes.

The following discussion presents the results and conclusions derived from the post-test analysis.

2. DISCUSSION

2.1 TEST FACILITY

The solid propellant test program was conducted in the 50-foot-diameter sphere of the High Reynolds Number Wind Tunnel Test Facility (Fig. 1) at Marshall Space Flight Center. Details of the facility selection process are included in Ref. 2. Modifications to the facility to satisfy the requirements of the test program are discussed in detail in Ref. 3. Briefly, the 50-foot-diameter sphere was modified to maintain pressure equivalent to altitudes in excess of 100,000 ft. Vacuum pumps and associated control mechanisms allowed for the selection of any simulated altitude in the sphere from local elevation to an altitude of 112,000 ft. The large volume of the sphere resulted in a negligible increase in sphere ambient pressure during the firing of the subscale solid propellant rocket motors.

2.2 HARDWARE AND INSTRUMENTATION

The subscale rocket motors used in the test program consisted of a conical nozzle with a nominal area ratio of 7.6, a nozzle exit diameter of 0.12 ft, and a nozzle half angle of 15 deg. A combustion chamber was loaded with an ammonium perchlorate propellant (Table 1) in a cylindrical grain configuration to produce neutral burning. The rocket motor configuration is presented in Fig. 2. Three propellant formulations were used in the test program. The formulations differed in the amount of metallic aluminum (2, 10 and 15%. By using propellants with different amounts of aluminum, the variation of exhaust plume pressures and heating rates with propellant aluminum loading was observable. In relation to Space Shuttle applications, the solid rocket boosters (SRB) have an aluminum loading of 16% and the separation motors have an aluminum loading of 2%. Typical values of chamber pressure consistently varied with propellant Aℓ loading. Motors burning the 2% Aℓ propellant produced the lowest range of chamber pressures (720 to 800 psia) and motors burning the 15% Aℓ propellant produced the highest range of chamber pressure (950 to 1000 psia). Thus the exhaust plumes produced by the 2% Aℓ propellant were physically smaller than those produced by the 15% Aℓ propellant. Pressure transducer probes located at the fore and aft end of the combustion chamber provided two chamber pressure measurements for each motor firing. The solid propellant charges produced motor burn times of 300 to 500 msec. Static pressure taps located at three positions on the divergent portion of each nozzle provided a measurement of nozzle flowfield characteristics.

A variety of plume measurements was obtained at three altitudes and numerous axial and radial locations. A rake mechanism for performing radial plume surveys was equipped with pitot pressure probes and pressure transducers, heating rate gages, a total temperature thermocouple and a force gage. To obtain impingement pressure and heating rate data, a flat plate 5 ft in length and 1 ft in width was instrumented with pressure transducers and heating rate gages (Fig. 3). The flat plate was large with respect to the exhaust plumes of the subscale rocket motors. This condition is typical of Space Shuttle exhaust plume impingement problems. For several rocket firings during the test program, the flat plate was equipped with a solid particle capture mechanism.

Details of the instrumentation characteristics, operational considerations and data reduction techniques are presented in Ref. 3. This information will not be repeated in this document except as required to explain observed experimental phenomena.

2.3 TEST MATRIX

The original test matrix called for 90 rocket firings at two altitudes, 50,000 and 100,000 ft, with 30 firings with each of three propellants. Radial surveys of the exhaust plumes and plume impigement measurements were initially specified for two axial locations, $x/D_{exit} = 5$ and 20. For each test condition, three rocket firings were to be made for repeatability. Pitot pressure measurements at $x/D_{exit} = 20$ early in the test program revealed an unexpected anomaly in the radial distributions of pitot pressure. The anomaly was not present in measurements at $x/D_{exit} = 5$. At this time it was hypothesized that the anomaly was due to a build up in the viscous portion of the exhaust plumes with increasing axial distance from the nozzle exit plane. To further investigate this phenomenon, additional test conditions were specified. Motor firings with plume instrumentation at $x/D_{exit} = 12$ and 16 were conducted to see if the growth of the viscous region of the plume was evident. To increase the size of the plume inviscid core, motor firings were made at a simulated altitude of 112,000 ft with plume radial survey instrumentation at $x/D_{exit} = 12$. Excellent repeatability was obtained for pitot and impingement pressure measurements early in the test program. The philosophy of specifying three motor firings for each test condition was amended and only two firings were considered necessary for the remainder of the test program. The final matrix of test condition employed in the program is presented in Fig. 4. Each symbol in the figure represents a motor firing.

2.4 EXPERIMENTAL DATA QUALITY

Overall quality of the experimental pressure and heating rate data was good. The parametric matrix of pressure and heating rate data is the most complete set of solid propellant exhaust plume and plume impingement data available to date.

Instrumentation used in the test program was exposed to a severe environment created by the multi-phase plumes of the solid propellant rocket motors. The plume environments were especially severe at the near field axial location, $x/D_{exit} = 5$, and for the propellants with high aluminum loadings. Clogging of the nozzle wall pressure ports nearest to the nozzle throat with particulate matter was a persistent problem. In many cases, the pressure transducer near the nozzle exit plane was the only acceptable nozzle measurement. Clogging of the pitot pressure probes near the nozzle centerline with ignitor material or particulate matter occurred frequently. Data channels displaying information from transducers with clogged probes were discernable from the time history of the channel during a given firing. In Fig. 5, the time histories of three pressure transducer outputs are plotted for a propellant with a 10% Al loading. The transducer pitot probes were positioned at an axial location of $x/D_{exit} = 5$ and radial locations of 0, 1 and 2 in. from the nozzle centerline. The decreasing transducer output with time for the centerline and $R = 1$ transducers are indicative of clogged pitot probes. Data with time histories such as these were deleted from the experimental data base. The centerline pressure transducer output in Fig. 6 illustrates another phenomenon present in some of the experimental pressure data for transducers near the nozzle centerline. The output of the transducer did not reach a steady state value during the firing. One explanation is the output of the transducers near the nozzle centerline drifted due to heating. High-speed color film of rocket firings with the rake mechanism in position revealed an intense stagnation region near the nozzle centerline on the sheet metal structure shielding the pressure transducers and instrumentation wiring harness. In Fig. 7 it may also be observed that the pitot tube running from the probe to the transducer is exposed to the exhaust plume for a short distance. With 10 and 15% Al propellants, heating rates 300 to 900 Btu/ft^2-sec were measured near the nozzle centerline at $x/D_{exit} = 5$. The thermal sensivity of the 5 and 15 psia Statham pressure transducers used for plume measurements was 0.001 psia/R and 0.0015 psia/R, respectively. The operating temperature range of these transducers was 395 to 710 R. A change of only 200 R in transducer temperature would result in a drift of 0.2 psia and 0.3 psia, respectively. Pressures measured at $x/D_{exit} = 5$ near the nozzle centerline were on the order of 3 to 5 psia. The deviation in the measured value of pressure would be 6 to 10% for only a 200 R increase in transducer temperature. The stagnation temperature of the flow at $x/D_{exit} = 5$ was on the order of 4000 to 5000 R. Heat transfer to the transducers could be accomplished by hot ignition gases entering the pitot probe, conduction along the exposed pitot tube to the transducer and by radiation to the transducer from the shield. Another explanation of the phenomenon involves the heating of a gas at constant volume. The gas occupying the pitot tube exposed to the stagnating flow would be heated to a relatively high temperature. With increasing temperature, the pressure of the gas in the pitot tube would increase, thus accounting for the upward ramp in the centerline transducer time history of Fig. 6.

With the exception of anomalies in some data near the nozzle centerline, the pitot pressure data were excellent. Repeatability of pitot and impingement pressure measurements for successive rocket firings at the same conditions was very good as illustrated in Figs. 8 and 9. Most of the pitot pressure data used in the post-test analysis had time histories similar to the R = 2 position in Fig. 5. Plume heating rate and impingement heating rate data had more data scatter between firings than the pressure data but was still at an acceptable level (Figs. 10 and 11).

Response problems were encountered with the original total temperature probe early in the test program. A redesigned probe was constructed but was damaged by the severe plume environment. Although the thermocouple was replaced, subsequent data were suspect and not used in the post-test analysis.

A force gage was mounted on the rake mechanism to measure total pressure force in the two-phase plume due to both the gas and solid particles. The device was intended to confirm that the pitot pressure probes were measuring gas-only pressure and not a combination of gas and particle pressures. Ambiguities in the trends of force gage measurements prompted the test engineers to recommend the force gage data for qualitative rather than quantitative analysis. Force gage measurements were not investigated extensively in the post-test analysis.

The solid particle capture mechanism performed acceptably. Captured particles were analyzed from the perspective of establishing trends in population as a function of particle diameter for the three propellant aluminum loadings. The wax medium used to capture the particles was found to have contaminants of the same order of size as the collected solid particles. The particle size data was considered unacceptable for analysis.

High-speed color movies were obtained of 58 rocket firings. The movies were excellent and proved to be an outstanding qualitative tool in analyzing the test data.

2.5 ANALYTICAL APPROACH

Two-phase exhaust plume flow fields were calculated analytically using the Lockheed-Huntsville RAMP computer code. This fully coupled solution requires the following input for a given problem: nozzle geometry, freestream boundary conditions, gas thermodynamic and transport properties, particle size distribution, particle thermodynamic properties and particle drag coefficient as a function of Reynolds number.

Thirty nozzles with the nominal dimensions of Fig.2 were fabricated for the test program. After fabrication, each nozzle was carefully measured to determine the degree of fidelity to the nominal dimensions. The nozzles typically varied a small amount from the design specifications. Based on previous experience with subscale nozzle analyses, a decision was made to use the measured geometry for defining the geometric input for the RAMP analysis. The ambient test cell pressure measured prior to each rocket firing was used to define the freestream boundary conditions. A negligible change in ambient pressure was observed during the rocket firings as the propellant mass was exhausted to the test sphere. Gas thermodynamic properties for the three propellants of Table 1 were calculated using a modified version (Ref.4) of a NASA-Lewis computer code (Ref.5) for calculating the properties of a combusting gas mixture. The expansion of a two-phase mixture is characterized by an increase in entropy level and a decrease in total enthalpy level (Fig.12). To properly model the expansion, tables of thermodynamic properties used in the flow field analysis must reflect the changing entropy and total enthalpy of the system. Analytically, the data are generated by perturbing the total enthalpy of the gas (mass is held constant) and repeating the calculational scheme. The total enthalpy is perturbed a number of times and by an amount specified by the user. The result is an array of equilibrium expansion processes and corresponding gas transport properties, each table of the array representing a different degree of heat transfer between the particulate and gaseous phases. To account for the effects of the momentum transfer between phases, each total enthalpy computation is repeated for a chamber pressure which is an order of magnitude less than the actual chamber pressure. The resulting thermodynamic table thus represents a different entropy level at a given value of total enthalpy. For a given point in the two-phase flowfield solution, the RAMP code enters the thermodynamic tables with a velocity, entropy and total enthalpy and interpolates for the corresponding thermodynamic and transport properties. Thermodynamic properties of particulate $A\ell_2O_3$ were obtained from the JANNAF thermochemical tables (Ref. 6). Based on experience from previous two-phase analyses, the particle drag model developed by Kliegel (Ref. 7) was used to define particle drag coefficient as a function of Reynolds number. The choice of particle drag model is discussed in more detail in Section 3.3.2. Originally, a log normal distribution about a mass mean particle size correlated with nozzle throat diameter (Ref. 8) was chosen to represent the distribution of $A\ell_2O_3$ particle sizes. Several refinements were made to this distribution during the course of the analysis. This topic is discussed in more detail in Section 3.3.1.

The exhaust plume flow fields calculated with the RAMP code were stored on magnetic tape for use later with auxiliary computer codes to plot flowfield data and calculate plume impingement data. For comparison with experimental pitot pressure measurements at various axial and radial locations, a radial plot computer code (Ref. 9) was used to search a flowfield tape and plot the radial distribution of gasdynamic properties at a specified axial distance from the nozzle. A radial plot computer code for particle data, and a plume impingement computer code, PLIMP, were used to calculate radial distributions of particle energy flux and gas convective heating rates. These data were compared with measurements by heating rate gages mounted on the radial survey mechanism of Fig. 3. The Marvin-Diewert stagnation point heating rate model (Ref. 10) in the PLIMP code was used to calculate the gas convective heating rates to the heating rate gages. The kinetic and thermal energy flux of the Al_2O_3 particles normal to the heating rate gages was calculated using the particle radial plot code. The gaseous and particulate contributions were compared with the total heating rates measured by the gages. The PLIMP code was used to calculate impingement pressures and heating rates on the flat plate. The gaseous pressure was compared with the experimentally measured pressure on the flat plate. Gas convective heating rates to the flat plate were calculated with the PLIMP code using the Eckert reference enthalpy method (Ref. 10) for flat plates. Particulate contribution to the total flat plate heating rate was calculated by determining the particle energy flux at points on the flat plate in the plume and calculating the component of the energy flux normal to the plate.

3. RESULTS

3.1 TWO-PHASE EFFECTS

Solid particulates and molten droplets in the nozzle and exhaust plume flow fields of solid propellant motors significantly affect the gasdynamic properties of these flows. The particulate oxidants, e.g., Al_2O_3, of metals added to the solid propellant charge must be accelerated by the expanding gas. This exchange of momentum between the gas and particulate phases is reflected in a reduced gas phase pressure. Experimental pitot pressure data and nozzle wall pressure data obtained during the test program confirms this phenomenon. The effect of Al propellant loading on nozzle exit plane pressure is illustrated in Figs. 13, 14 and 15. The average experimentally measured nozzle wall static pressure is lower (P_c/P is higher) for the 2% Al propellant (Fig. 13) firings than for the 10% Al propellant (Fig. 14) firings. The difference in experimental static pressures between the 10 and 15% Al propellants is negligible. Nozzle exit plane pressures calculated analytically predict this trend, i.e., lower exit plane pressures for the 2% Al propellant. Pitot pressure measurements reflect the difference in expansions for propellants with different Al loadings. For pitot pressure measurements, the difference in Mach number dominates the difference in static pressure. Propellants with a low Al loading will exhibit a higher rate of expansion than propellants with a high Al loading. At a comparable point in the two expansions, the low Al propellant will produce a higher Mach number and a lower static pressure than the high Al propellant. Momentum and energy exchange between the gas and particle phases results in a decreasing rate of expansion for increasing propellant Al Loading. Thus the higher propellant Al loading is, the higher the nozzle exit static pressure. The nozzle wall pressure comparisons indicate that the analytical model is adequate for predicting two-phase nozzle expansions. In Fig. 16, radial distributions of experimental pitot pressure are plotted for propellants with 2, 10 and 15%

Al loadings. At $x/D_{exit} = 12$, the 2% Al propellant distribution has a higher pitot pressure than the 10 and 15% Al propellant distributions. The 15% Al propellant has the lowest pitot pressure. In Fig. 17, the analytical pitot pressure distributions calculated with the RAMP code are presented for the three Al propellant loadings at $x/D_{exit} = 12$. The results are qualitatively in agreement with the experimental data of Fig. 16. The 2% Al propellant has the highest calculated pitot pressure distribution and the 15% Al propellant the lowest. Different chamber pressures account for the differences in ambient to chamber pressure ratio for the three propellants. The 2% Al propellant consistently produced chamber pressures in the 720 to 800 psia range, the 10% Al propellant in the 850 to 950 psia range and the 15% Al propellant in the 950 to 1000 psia range.

The molten and solid particulates in two-phase flows remain at a higher temperature than the surrounding gas. As the expanding gas cools, the higher temperature particles transfer energy to the gas through convective heat transfer. The high thermal energy retained by the particulates produce an increasingly hostile thermal environment for increasing Al propellant loading. Figure 18 presents plots of radial distributions of measured energy flux for the three Al propellant loadings at $x/D_{exit} = 20$. The 15% Al propellant produced the most severe thermal environment and the 2% Al propellant the least severe environment. Figures 19 and 20 present the analytically calculated thermal environments created by the gas and particle phases, respectively. Analytically, the qualitative trends agree with the experimental measurements. The calculated thermal environment is most severe for the 15% Al propellant loading.

3.2 THERMOCHEMICAL MODEL

Correct analytical prediction of gasdynamic properties in rocket exhaust plumes is strongly dependent on correctly modeling the thermodynamic properties of the propellant involved. Experience in modeling rocket exhaust plumes indicates that many chemical systems experience a transition from equilibrium to frozen chemistry during the expansion process. It was necessary to determine the pressure ratio at which this transition occurred for the three propellants investigated. A nozzle solution was generated for each propellant using the nonequilibrium chemistry version of the RAMP code.

The nonequilibrium chemistry package utilizes finite difference techniques and reaction mechanisms of the involved chemical species to calculate the thermodynamic properties of a fluid system at a given temperature. For each propellant, the species mole fractions of the system constituents were plotted as a function of axial distance along the nozzle centerline. In Fig. 21, results for tne 2% Al propellant are presented. The concentrations of the major species (H_2, CO, HCl, H_2O, N_2) remain nearly constant from the nozzle throat. Minor species such as OH and Cl are the only constituents changing significantly in the nozzle expansion. Due to their low concentrations, these species would have a negligible effect on the system thermodynamics. Species concentrations for the 15 and 10% Al propellants were similar to those in Fig. 21. Based on this analysis the chemistry model for all three propellants was chemically frozen at the pressure ratio corresponding to the nozzle throat.

Another chemistry model frequently used in exhaust plume analysis is the constant thermodynamic property or "ideal gas" mode. A constant ratio of specific heats, γ, and gas constant are assumed throughout the flowfield solution. One exhaust plume was calculated in this analysis using this thermochemical model. The plume was calculated for the 2% Al propellant exhausting to a simulated altitude of 100,000 ft. A comparison was made between analytical and experimental pitot pressure distributions at $x/D_{exit} = 20$. The results are presented in Fig. 22. The data comparisons are poor especially when considered in light of the excellent comparisons obtained for this case when the equilibrium chemistry model was used (Fig. 31). It was concluded that the constant thermodynamic property model is inadequate for predicting gasdynamic properties in two-phase exhaust plumes.

3.3 EMPIRICAL INPUT DATA

Implicit analytical solutions have not been developed to calculate a priori the distribution of solid particle sizes present in the nozzle and exhaust plume of a given solid propellant rocket motor. Neither are there closed form analytical solutions for calculating the drag coefficient and heat transfer coefficient of particles in two-phase exhaust plumes. Particle size, drag and heat transfer coefficient data for input to the RAMP flowfield solution are developed empirically. One of the purposes of the solid propellant test program was to verify the empirical correlations used to produce these data.

3.3.1 Mass Mean Particle Size

Preliminary analytical flowfield calculations were generated using a mass mean particle diameter obtained from an empirical correlation in Ref. 8. The mass mean particle diameter is correlated with nozzle throat diameter. For the nominal nozzle geometry used in the test program, the correlation produced a mass mean diameter of 3.0 microns. A log normal distribution of six particle sizes was generated about the mean diameter. Flowfield calculations performed with this particle distribution produced excessively large variations in system entropy, total enthalpy and particle velocity lags. Results of experimental/analytical pitot pressure and heating rate data comparisons were poor. Closer scrutiny of the throat diameter correlation revealed that the applicable range of the correlation terminated at a nozzle throat diameter of 0.083 ft. The throat diameter of the test program nozzles was 0.043 ft. A search was made to locate another empirical correlation which would be applicable to subscale solid propellant motors. The following correlation was obtained from Ref. 11:

$$D_p = 0.454 (P_c)^{1/3} (\xi)^{1/3} \left[1 - e^{-0.004 L^*}\right] (1 + 0.045 D_t)$$

D_p = mass mean particle diameter
ξ = mole fraction of condensed phase
L^* = chamber volume parameter
D_t = nozzle throat diameter

This correlation accounts for variation in mass mean particle diameter with chamber pressure, percent Al loading, nozzle throat diameter and motor, L^*. Although very little data had been generated using this correlation for subscale motors, there were not apparent limitations in the range of parameters for the test program motors. The correlation predicts a variation in mass mean particle diameter with Al loading and yielded the following results for the three propellants:

15% Al propellant – 1.67 microns
10% Al propellant – 1.44 microns
2% Al propellant – 0.80 microns

Log normal distributions of 6 particle sizes were calculated for each mean diameter. Numerous nozzle and exhaust plume flow fields were calculated using these distributions. Comparison of analytical and experimental pitot pressures resulted in excellent agreement fot the 2% Aℓ propellant and improved but still unsatisfactory agreement for the 10 and 15% Aℓ propellants. Comparisons of experimental and analytical radial pitot pressure distributions are presented in Fig.23 for the 10% Aℓ propellant at $x/D_{exit} = 5$. The dashed line represents an analytical calculation with a mean particle diameter of 1.44 microns. The agreement with experimental data is greatly improved over the 3.0 micron mean diameter data but is still unsatisfactory. Consequently, empirical input data to the RAMP code was further scrutinized to determine the cause of the discrepancy.

3.3.2 Particle Drag Model

The particle drag model is another empirical input which influences the momentum exchange between the gas and particle phases and thus the gas Mach number and static pressure. Particle drag data are input to the RAMP code in the form of particle drag coefficient as a function of particle Reynolds number. From previous analyses a drag model developed by Kliegel (Ref. 7) was selected for preliminary calculations. To investigate the sensitivity of the analytical/experimental data comparisons to particle drag model, a nozzle and plume flow field was calculated using the drag model developed by Crowe (Ref.12). In Fig.24 radial distributions of pitot pressure at $x/D_{exit} = 5$ are compared with experimentally measured data for the 10% Aℓ propellant. At lower Reynolds numbers corresponding to flow in the plume core, the analytical data calculated with the Kliegel drag model compared more favorably with the experimental measurements. At the higher particle Reynolds numbers characteristic of flow near the plume boundary, the Kliegel and Crowe drag models produced identical results. It was concluded that the Kliegel drag model was more applicable for the flow regimes being investigated. The sensitivity of the data comparisons to the magnitude of the particle drag coefficient was investigated. Nozzle and plume solutions were calculated for the 10% Aℓ propellant using values for the particle drag coefficient calculated by multiplying the Kliegel drag coefficient by 0.2 and 2.0, respectively. Figure 25 compares the results of the analytical calculations with experimental data at $x/D_{exit} = 5$. At lower particle Reynolds numbers, the calculation with $0.2 \times C_D$ produces somewhat better agreement with the experimental data than the calculation with $2.0 \times C_D$ produces somewhat worse agreement. At higher particle Reynolds numbers near the plume boundary, the calculation with $0.2 \times C_D$ produces worse agreement with the experimental measurements and the calculation with $2.0 \times C_D$ produces improved agreement. Several conclusions were drawn from these results. The Kliegel drag model overpredicts the magnitude of the particle drag coefficient at low Reynolds numbers and underpredicts the magnitude at high Reynolds numbers. The result is overprediction of particle related momentum losses near the nozzle centerline and underprediction of momentum losses near the plume boundary. Large perturbations in particle drag coefficient do not produce corresponding perturbations in gas pitot pressure. Inadequacies in the particle drag model alone could not account for the difference in the measured and predicted pitot pressures of Fig. 25.

The difference in pitot pressure comparisons for the 10 and 15% Aℓ propellants appeared to be caused by discrepancy in the analytical modeling of the momentum losses in the gas resulting from the $A\ell_2O_3$ particles. Two empirical input parameters govern the momentum exchange between phases, particle drag coefficient and particle size distribution. After investigating the effect of particle drag coefficient, a further refinement of the particle size distribution was attempted. Experimental data collected by the Air Force is illustrated in Fig. 26. Mass mean particle diameter is presented as a function of motor L^*. The solid propellant motors used in the test program had an L^* of approximately 53. From the data in Fig. 26, a mass mean particle diameter of 0.8 microns corresponds to an L^* in this range. This mean diameter is identical to the one calculated from the Cheung-Cohen correlation for the 2% Aℓ propellant. A nozzle and plume flow field was calculated for the 10% Aℓ propellant using a log normal six particle size distribution about a mass mean diameter of 0.8 microns. Figure 23 presents the results of a comparison of pitot pressure distributions at $x/D_{exit} = 5$. The analytical/experimental data agreement is significantly improved over results obtained previously with a mass mean diameter of 1.44 microns. Nozzle and plume flow fields calculated for the 15% Aℓ propellant using a mean diameter of 0.8 microns also resulted in improved data agreement.

Previous researchers have concluded that the solid particles emerging from a solid propellant motor vary in size. The dispersion of sizes is thought to be estimated by a log normal distribution. The computer run time for a RAMP flowfield calculation becomes measurably longer as the number of different particle sizes is increased. Each calculation involving particle properties must be repeated for each different particle size. It is thus expedient to reduce the number of particle sizes. Other researchers have also stated that a single mean particle size is adequate for two-phase flowfield calculations. With these points in mind, a RAMP solution was generated for the 2% Aℓ propellant using a single particle size with a diameter of 0.8 microns. In Fig. 27 radial distributions of pitot pressure at $x/D_{exit} = 12$ calculated with the single particle size and the six particle log normal distribution are compared with experimental measurements. The single particle size calculation did not compare as well with the experimental pitot pressures as the six particle calculation. It was concluded that multiple particle distributions more adequately model the effect of particulates on the flowfield pressures.

3.4 NOZZLE WALL PRESSURES

Three static pressure taps were included in each nozzle used in the test program (Fig. 2). The two pressure taps located nearest to the nozzle throat were frequently plugged by particulate matter. In the following discussion, comparisons will be presented only for the pressure taps nearest to the nozzle exit plane. Analytical calculations of the nozzle wall static pressure was limited to the inviscid RAMP solution. No effort was made to account for the presence of a boundary layer (gas and/or particle) on the nozzle wall. In Figs. 13, 14 and 15 the results of typical RAMP nozzle calculations are compared with experimental measurements for several nozzles and rocket firings with the 2, 10 and 15% Aℓ propellants, respectively. Note that the analytical calculation represents the results for only one nozzle geometry. The analytical curve would vary somewhat for each different nozzle geometry. In Fig. 13, the analytical calculation for the 2% Al propellant passes through the upper portion of the experimental data cluster. In Fig. 14, the analytical calculation for the 10% Al propellant indicates similar results. As pointed out in Section 3.1, the nozzle wall static pressure near the exit plane is significantly higher for the 10% Al propellant that the 2% Al propellant for both the experimental and analytical data. The analytical curve passes through the experimental data cluster in Fig. 15 for the 15% Al propellant. The 15% Al data exhibited a greater variation in magnitude than the 2 or 10% Al data. The difference in the experimental measurements for the 10 and 15% Al propellants is negligible. A significant particle ladden boundary layer was present in the nozzles for the 10 and 15% Al propellant firings. This was deduced from inspection of the nozzles following the firings (Ref. 3). Significantly larger amounts of particulate slag were deposited on the nozzles used with the 15% Al propellant. It was concluded that increased particle interaction with the nozzle wall contributed to the negligible difference in measured pressures for the 10 and 15% Al propellants, i.e., the effect of particle interaction with the nozzle wall dominated the effect due to the change in Al loading. Based on these data comparisons, it was concluded that the RAMP two-phase nozzle solution performed satisfactorily.

3.5 EXHAUST PLUME DATA COMPARISONS

Verification of the RAMP flowfield solution was achieved by comparison of analytical and experimental pitot pressure and heating rate distributions. Pitot pressure is a gasdynamic property easily measured in supersonic flows. Pitot pressure measurements are relatively insensitive to local flow angle and thus there was no effort to align the pitot probes with the local gas streamlines. There was no evidence of flow angle effect on the measured data at different radial locations.

3.5.1 Pitot Pressure Comparisons

The original test matrix specified the measurement of pitot pressures at two axial distances from the nozzle exit plane, $x/D_{exit} = 5$ and 20. Test measurements were first obtained in the less severe environment at x/D_{exit} = 20. Pitot pressure data exhibited an unexpected variation with radial distance from the nozzle centerline. In Fig. 28, a disturbance defined by an increase in pitot pressure penetrates to within two nozzle diameters of the nozzle centerline. The phenomenon is apparently a characteristic of gas expansions since the effect is present for the 2% Aℓ propellant. It was hypothesized that the lip shock was being moved inboard by a large viscous region. The peak in pitot pressure in Fig. 28 would be due to the lip shock. The sloping pressure distribution outboard of the shock would be due to decreasing flow velocity in the viscous region as the flow decelerated to quiescent ambient conditions. If this hypothesis was correct, the inviscid core of the plume would include a greater portion of the total plume flow and the lip shock would move closer to the plume boundary with decreasing distance from the nozzle exit. Additional plume radial surveys at x/D_{exit} = 12 and 16 were specified to investigate this phenomena.

Radial distributions of experimentally measured pitot pressure at several axial locations are presented in Figs. 29 and 30 for the 2 and 10% Aℓ propellants, respectively. Included in both figures is a typical RAMP exhaust plume boundary corresponding to the experimental test conditions. As anticipated, the size of the viscous region decreases and the location of the peak pressure moves closer to the plume boundary as the radial surveys moved closer to the nozzle exit plane. A two-phase effect is discernable when Figs. 29 and 30 are compared. The compression and viscous regions appear to be more smeared for the 10% Aℓ propellant than the 2% Aℓ propellant. The peak pressures for the 10% Aℓ propellant are lower than the peak pressures for the 2% Aℓ propellant.

The observed phenomenon is well documented in analyses of far plume flow fields. An inviscid core flow exists in highly expanded plumes from the nozzle to x/D_{exit} = 20 to 40. At this point viscous effects have penetrated to the nozzle centerline, and the plume flowfield can no longer be accurately modeled by inviscid analytical techniques. Figures 29 and 30 clearly show the change from a predominantly inviscid plume to an increasingly viscous plume as the distance from the nozzle exit plane increases.

The RAMP inviscid flowfield solution produces good agreement with measured pitot pressures in the inviscid portion of the exhaust plumes at the three altitudes, for the three Aℓ propellant loadings at the four axial stations. Figure 31 compares analytical/experimental pitot pressure for the 2% Aℓ propellant at $x/D_{exit} = 16$ and 20. The data comparisons are excellent in the inviscid region of the plume. Note the larger inviscid region at $x/D_{exit} = 16$. In Figs. 32 and 33 pitot pressure comparisons at $x/D_{exit} = 20$ are presented for the 10 and 15% Aℓ propellants respectively. At $x/D_{exit} = 16$, the 10% Aℓ propellant produced the distribution in Fig. 34. Data comparisons are acceptable in the inviscid portions of the plume.

Two simulated altitudes, 100,000 and 112, 000 ft, were used to obtain radial survey data at $x/D_{exit} = 12$. The 112,000 ft altitude was specified to increase the size of the inviscid region of the plumes. Comparisons of the analytical and experimental pitot pressures at a simulated altitude of 100,000 ft are presented in Figs. 35, 36 and 37 for the 2, 10 and 15% Aℓ propellants, respectively. Data comparisons for the 2 and 10% Aℓ propellants are excellent in the inviscid region of the plume. The 15% Aℓ propellant pitot pressure comparison is acceptable although the analytical and experimental distributions have a somewhat different slope from the nozzle centerline to $R/D_{exit} = 4$. For an altitude of 112,000 ft, analytical/experimental pitot pressure comparisons are presented in Figs. 38, 39 and 40 for the 2, 10 and 15% Aℓ propellants, respectively. With the exception of experimental data at $R/D_{exit} = 1.39$ and 1.66, the pitot pressure comparisons are excellent for all three propellant loadings. The experimental data for each propellant at these two radial locations have a different slope than the remainder of the distribution. Referring to Figs. 35, 36 and 37, the corresponding experimental data for an altitude of 100,000 ft do not exhibit this phenomenon. The time histories of the transducers in question are acceptable and do not show any anomalies. Experimental data for the two different altitudes were obtained at different times in the test program with somewhat different instrumentation configurations. It was concluded that the experimental measurements at these two radial locations were in error. At the time of this writing, the cause of the error is unknown.

The results presented in Figs. 38, 39 and 40 support the conclusion that the RAMP two-phase flowfield solution is an adequate model for inviscid flows. The analytical calculations agreed with the experimental measurements for a greater radial distance from the nozzle centerline than for the 100,000 ft altitude test conditions.

Figure 41 shows radial distributions of pitot pressure at $x/D_{exit} = 5$ for the 10 and 15% Aℓ propellants exhausting to an altitude of 100,000 ft. There were no rocket firings using the 2% Aℓ propellant at these test conditions. Both data comparisons are good. The analytical 15% Aℓ pitot pressure distribution has a somewhat different slope than the experimental data which suggests the need for a small refinement in the particle size distribution and/or the particle drag model. Radial distributions of pitot pressure at $x/D_{exit} = 5$ and a simulated altitude of 50,000 are presented in Figs. 42 and 43. The difference in gas pressure caused by the presence of solid particles in the expansion is clearly illustrated in Fig. 42. Analytical and experimental pitot pressures for the 15% Aℓ propellant are significantly lower than those for the 2% Aℓ propellant. Location of the lip shock in the experimental plumes can be approximated by the location of the peak pitot pressure in the radial distribution of measured pressures. The RAMP code predicts the shock location for the 2% Aℓ propellant but does not appear to predict the shoc location very well for the 15% Aℓ propellant. The experimental distribution for the 2% Aℓ propellant is very similar to pitot pressure distributions obtained in a previous test program at $x/D_{exit} = 1.5$ using air as the working fluid. The pressure distribution radially outboard of the peak pressure due to the lip shock is the pressure decay through a shear layer created as the plume flow decelerates from a supersonic velocity to the quiescent ambient environment. The shear layer appears to increase in size with increasing Aℓ loading in Figs. 42 and 43. This qualitative trend is also evident when the pitot pressure distributions for the 2 and 10% Al propellants in Figs.29 and 30 are compared.

3.5.2 Energy Flux Distributions

Experimental plume energy flux data were obtained at several radial locations for each plume axial station radially surveyed with the rake mechanism. Slug calorimeters mounted on cylindrical probes measured energy flux at points in the plume. Energy flux data from points in the viscous portion of the plumes were not included in the data comparisons. In laminar flow regimes, convective energy fluxes are proportional to the square root of pressure. If experimental and analytical pressures do not compare at a given point, the energy flux at a corresponding radial location may still be compared by adjusting the analytical energy flux by the square root of the ratio of experimental to analytical pressure. This simple correction is not applicable in a complex flow regime such as the viscous mixing region of a plume. To compare with the total plume energy flux measured by the calorimeters, the analytical particle energy flux normal to the calorimeters and the gas convective energy flux were calculated. For each test condition investigated, the analytical particle and gas energy fluxes were plotted separately as a function of radial distance from the nozzle centerline. To obtain the total calculated energy flux at a given radial location, the values of the particle and gas energy fluxes are summed. Typically the calculated value of total energy flux is larger than the measured value in two-phase exhaust plumes. This effect is more pronounced with increased Al propellant loading. This well-documented phenomenon is thought to be the result of a particle debris layer forming on the heat transfer probe and shielding it from the total energy flux in the plume. An accommodation coefficient has been applied to RAMP and PLIMP impingement energy flux calculations in the past to account for the shielding phenomenon. The particle energy flux calculated analytically is multiplied by a constant fraction (typically 0.3 to 0.5) before being added to the gas convective energy flux to obtain the total predicted energy flux. A primary objective in the analysis of the test program energy flux data was to determine the actual accommodation coefficient (α) for different test conditions.

To determine α from the analytical/experimental data comparisons, the calculated value of gas convective energy flux was subtracted from the measured energy flux value and the resulting figure divided by the predicted particle energy flux normal to the probe. Comparisons of calculated gas convective energy flux and particle energy flux with measured total energy flux are presented in Figs.44 through 57. Table 3 contains a cross reference guide for the heating rate figures as a function of altitude, propellant loading and axial station. Because of the small size of the plumes, only one data point was obtained in the inviscid portion of the plumes at a simulated altitude of 50,000 ft. Several calorimeters were destroyed or rendered inoperable by the severe impingement environments in the plumes at $x/D_{exit} = 5$ and an altitude of 50,000 ft.

Figures 47, 48 and 49 show the analytical/experimental energy flux comparisons at $x/D_{exit} = 12$ and an altitude of 100,000 ft for the 2, 10 and 15% Al propellants. Comparison of these figures indicates the relative contribution of the gas and particulate phases to the total plume energy flux for various propellant Al loadings. The total energy flux increases significantly with increasing Al loading (both experimentally and analytically). The particulate contribution to the total energy flux increases significantly with increasing Al loading. For the 10 and 15% Al propellants, the particle energy flux dominates the thermal environment. The gas convective flux is greater than the particle energy flux for the 2% Al propellant. The gas convective energy flux for the 15% Al propellant is somewhat greater (even after compensation for differencies in chamber pressure) than the fluxes for the 10 and 2% Al propellants. Particles in a gas expansion typically remain at a higher temperature than the gas and transfer thermal energy to the gas phase. At a specified axial station in comparable plumes, the gas temperature is greater for a propellant with a higher loading of solid particles. In the Marvin-Diewert stagnation point heat transfer model, temperature effect is reflected primarily in the change in specific heat at constant pressure, C_p. Prandtl number, Pr, and enthalpy, h_D, H_s and h_w, contain C_p to the first power in the following relation:

$$\dot{q} = \frac{0.324}{Pr_w} \sqrt{2 \rho_w \mu_w \left(\frac{dV}{dR}\right)} \left[\frac{1 + \phi_D}{h_D/H_s - h_w/H_s}\right]^{-0.15} (H_s - h_w)$$

At a given point in comparable plumes, the gas temperature and C_p are higher for a 15% Aℓ propellant than for a 2% Aℓ propellant.

The particle energy flux at a given axial station in comparable plumes is a function of the gas expansion but predominantly a function of percent Aℓ loading. The analytical variation in particle energy flux with propellant Aℓ loading is evident at each axial station. Comparison of Figs. 45 and 46 reveals that the particle energy flux for the 15% Aℓ propellant is significantly greater than the flux for the 10% Aℓ propellant at $x/D_{exit} = 5$. This trend is still evident in Figs. 56 and 57 at $x/D_{exit} = 20$. The more severe thermal environment in the 15% Aℓ plume is evident experimentally not only in the higher measured energy fluxes but also in the photographs of the rocket firings. In Fig. 58 photographs reproduced from color movies of the rocket firings are presented for the 10 and 15% Aℓ plumes impinging on the flat plate. The test sphere was not illuminated with a lighting source. Visible radiation recorded on the photographs is entirely from the rocket firings. The 2% Aℓ propellant produced sufficient radiation to be visible on the color film but insufficient visible radiation to appear in the black and white reproductions. Photographs of the 2% Aℓ rocket firings are available but could not be included in this report because of the aforementioned reproduction difficulties. The visible radiation in the photographs of Fig. 58 is emitted from the particles (the 2% Aℓ plumes were almost invisible due to the small number of particles) which are at a sufficiently high temperature to emit visible radiation. There is a significant visible difference in the radiation level from the plumes with different Aℓ propellant loadings.

At the $x/D_{exit} = 20$ axial station, the measured energy fluxes in the inviscid portion of the 2 and 10% Aℓ plumes were somewhat higher than the total predicted energy flux. Comparing energy fluxes at $x/D_{exit} = 16$ and 20 in Figs. 53 and 55 for the 2% Aℓ propellant and Figs. 54 and 56 for the 10%

Al propellant, it is observed that the particle energy flux decreases by a larger percentage than the gas convective flux between $x/D_{exit} = 16$ and 20. This observation suggests that a deficiency in modeling the particle phenomena is responsible. Preliminary flowfield calculations in the post-test analysis employed a particle size distribution with a mass mean diameter of three microns. In Fig. 59, energy flux distributions are compared for plume calculations using different mass mean particle sizes. With a particle distribution about a mean diameter of three microns, the gas convective energy flux is less than the flux calculated with a mean diameter of 0.8 microns. The particle energy flux near the nozzle centerline is an order of magnitude greater for the calculation with the three micron mean particle diameter. Particle energy flux is sharply peaked near the nozzle centerline and decreases rapidly with increasing radial distance from the nozzle centerline. Limiting streamlines for the larger particles are located nearer to the nozzle centerline for the plume calculated with a larger mass mean particle diameter. Thus, a greater amount of particle kinetic and thermal energy is present near the nozzle centerline. A small increase in the mean particle diameter would provide the necessary particulate energy to increase the total predicted energy flux to the measured level. In the analytical model, the energy coupling between the gas and particulate phases is more sensitive to particle size than the momentum coupling. A particle distribution input to the analytical model might be adequately refined to accurately predict pressures in the plume but not adequately refined to accurately predict total energy flux. This deficiency would be especially evident in the plume far field where particle mass fluxes are low and the analytical predications approach the measured value of total energy flux, i.e., small amounts of particulate matter to produce shielding and debris layer effects. This trend in decreased shielding effects with decreased particle mass flux is evident in Fig. 60. Particle mass flux is plotted as a function of energy flux accommodation coefficient. The data approach an accommodation coefficient of 1.0 as the particle mass flux decreases toward zero. At the time of this writing, it was concluded that a slight refinement in the particle size distribution would correct the discrepancy in the $x/D_{exit} = 20$ energy flux comparisons.

3.6 IMPINGEMENT DATA COMPARISONS

The flat plate apparatus depicted in Fig. 3 was used to obtain impingement pressure and heating rate data at $x/D_{exit} = 5$, 12 and 20 with the flat plate at several angles of attack with respect to the nozzle centerline. Orientations of the flat plate that were analyzed are defined in the schematic diagrams of Fig. 61. As indicated in the photographs of Figs. 62 and 63, the two-phase flow field in the vicinity of the flat plate is quite complex. The flow complexity is a result of the large size of the plate relative to the plume as well as the coupling between the gas and particulate phases downstream of the shock standing off the plate. The variation in impingement phenomena with angle of attack of the body is illustrated in Fig. 62. With the flat plate at several inclination angles, the shock structure and boundary layer on the plate are significantly different. As the flat plate approached an inclination angle of 90 deg, the standoff shock became normal to the plume flow. The shock standoff distance increased with increasing inclination angle. With the flat plate at 90 deg and centered at $x/D_{exit} = 20$, the normal shock is approximately seven nozzle diameters upstream of the flat plate. The gas-particle coupling behind the standoff shock was beyond the scope of this project and was not investigated. The PLIMP code does not model the shock with a large standoff distance. PLIMP impingement calculations assume that the impingement shock is very close to the body surface. The complex two-phase flow field behind the shock is not modeled by the PLIMP code. At the high-body angles of attack, the effect on impingement pressures and heating rates of the standoff shock structure is significant. Impingement pressure and heating rate comparisons, presented later in the text graphically illustrate this point. In Fig. 63, the size of the visible boundary layer on the plate varies with propellant $A\ell$ loading. Apparently the size of the boundary layer increases with increasing $A\ell$ loading. The more solid particles that are present in the plume, the more particles that are entrained in the plate boundary layer. The PLIMP impingement model does not account for the additional boundary layer thickness resulting from increased propellant $A\ell$ loading. One accommodation coefficient is used in the present analysis to account for all mechanisms (shocks, debris layers, particle effects, etc.) which affect the transfer of energy from the plume to the surface of an impinged body. One purpose of this analysis is to determine the value of this accommodation coefficient for heating rate comparisons for various test configurations and propellant Al loadings.

3.6.1 Impingement Pressure Comparisons

In Figs. 64, 65 and 66, analytical and experimental impingement pressures are compared for the flat plate at $x/D_{exit} = 5$ with the flat plate inclined at 45 deg to the nozzle centerline. The experimental data were obtained at a simulated altitude of 50,000 ft. Comparison of the experimental data for the three propellant Al loadings indicate that the impingement pressure is a function of Al loading. For the same experimental conditions, the 2% Al propellant produced the highest impingement pressure and the 15% Al propellant produced the lowest impingement pressure. This trend is the same as that observed in the radial surveys of gas pitot pressure. It was concluded that gas effects dominate the impingement pressure measurements. Comparisons of the experimental and analytical flat plate impingement pressures are good at $x/D_{exit} = 5$ for all three propellant Al loadings exhausting to a simulated altitude of 50,000 ft. The photographs of Fig. 63 correspond to these test conditions for the 2 and 15% Al propellant loadings. Analytical impingement pressure calculations agreed in magnitude and trend with the experimental data at $x/D_{exit} = 5$ and a simulated altitude of 100,000 ft. Impingement pressure comparisons along the flat plate centerline are plotted for the 2 and 10% Al propellants in Figs. 67 and 68, respectively.

Figure 69 illustrates schematically the impingement of a plume on the flat plate located in the plume at $x/D_{exit} = 20$. The plume radial pitot pressure surveys revealed that the viscous region of the plume comprises a significant portion of the plume flow at $x/D_{exit} = 20$. Local pitot pressure in the viscous region increased to a value significantly higher than that predicted inviscidly. The same phenomenon was observed in the flat plate impingement measurements at $x/D_{exit} = 12$ and 20. Analytical/experimental impingement pressure data comparisons at $x/D_{exit} = 12$ are presented in Figs. 70, 71 and 72 for the 2, 10 and 15% Al propellants, respectively. The impingement pressures calculated analytically agree fairly well with the experimental data on the portion of the plate located in the inviscid portion of the plumes, although the location of the shock somewhat upstream of the surface of the plate may explain the measured core impact pressures being higher than predicted. Measured impingement pressures on the flat plate located in the viscous portion of the plumes are significantly higher than the pressures predicted inviscidly. This trend is observed again in the impingement pressure data comparisons at $x/D_{exit} = 20$. Impingement pressure comparisons for the plate inclined at 30 deg and centered at $x/D_{exit} = 20$ are presented in Figs. 73, 74 and 75. Comparisons for the flat plate inclined at 45 deg are presented in Figs. 76, 77 and 78 for the 2, 10 and 15% $A\ell$ propellants, respectively. Data comparisons for the flat plate positioned normal to the nozzle centerline at $x/D_{exit} = 20$ are presented in Figs. 79, 80 and 81. Predicted impingement pressures at $x/D_{exit} = 20$ are significantly lower than the measured pressures in each case over the entire length of the plate. In Fig. 62, it is observed that a normal shock is standing off the plate at a distance of 5 to 7 nozzle diamters. A PLIMP calculation at $x/D_{exit} = 15$ in Fig. 79 produced excellent agreement in the inviscid portion of the plume. The normal shock structure standing off the plate significantly affects the environment seen by the plate. From the results presented in Fig. 79, it appears that the stagnation pressure seen by the flat plate is approximately equal to the stagnation pressure behind the normal shock. The PLIMP model assumes that the shock is located physically close to the impinged body. The model does not calculate the large shock standoff distance associated with bodies at high angles of attack or the gasdynamic properties of the expansion behind the shock. A cursory investigation of the problem indicates that the gas-particle flow behind a shock may exhibit significantly different characteristics than the flow in a typical expansion. There is a possibility that the gas is "shocked down" in velocity when passing through a shock but the particles are not "shocked down" as much. The net result downstream of the shock could be a reversal of the energy and momentum transfer between the gaseous and particulate phases. The particles would transfer momentum to the gas and the gas (now at a higher temperature than the particles) would transfer thermal energy to the particles. These phenomena would significantly affect the actual pressures and heat transfer rates experienced by an impinged body. Further refinement of the impingement analysis is necessary to accurately predict the impingement environment experienced by large bodies at high angles of attack immersed in small plumes.

3.6.2 Impingement Energy Flux Comparisons

In Figs. 82 and 83, analytical and experimental impingement heating are compared along the centerline of the flat plate at $x/D_{exit} = 5$ with the plate inclined at 45 deg to the nozzle centerline. Comparison of the experimental data for the 2 and 10% propellant Aℓ loadings indicates that the impingement energy fluxes are a strong function of Aℓ loading. For the same experimental conditions, the 10% Aℓ propellant produced the highest impingement energy flux and the 2% Aℓ propellant produced the lowest. This trend is the same as that observed in the radial surveys of plume energy fluxes. Comparisons of experimental and analytical impingement energy fluxes at a simulated altitude of 50,000 ft are not presented. The exhaust plumes were small and did not impinge directly on any calorimeters. For this test condition, energy flux due only to upwash and downwash on the plate was measured experimentally. Experimental impingement data was not obtained for the simulated altitude of 112,000 ft.

Impingement energy flux comparisons for the flat plate (45 deg inclination) centered at $x/D_{exit} = 12$ are presented in Figs. 84, 85 and 86 for the 2, 10 and 15% Aℓ propellants, respectively. The trend of increasing analytical impingement energy flux with propellant Aℓ loading is evident. The increase in experimental energy flux with Aℓ loading is smaller than that predicted analytically. This reflects the increased shielding of the flat plate surface by a gas and particulate debris boundary layer with increased propellant Aℓ loading.

Far field impingement energy flux comparisons are presented in Figs. 87 through 95 for the three propellants impinging on the flat plate inclined at angles of 30, 45 and 90 deg. Figure 87 shows that the experimental energy flux at Y = 1.25 ft is higher than the sum of the gas convective and particle energy fluxes. Apparently the lip shock impinged directly on the calorimeter or the shear layer was present at Y = -1.25 ft resulting in a very high energy flux.

The heat transfer model that was used to calculate the gas convective heating rate distributions was Eckert's Reference Enthalpy method for flat plates. For low angles of attack (30 deg flat plate cases) this method gives reasonable distributions of heating rate; however, at high angles of attack (on the upstream portion of the plate) the results are questionable and perhaps another theory should have been used. The convective heating rates are important since it is necessary to have an accurate prediction in order to calculate meaningful accommodation coefficients for the amount of particle energy flux transferred to the surface. For the 2% aluminum loading a relatively small error or change in convective heating rate may result in a large difference in accommodation coefficient since the gaseous heating in the regions of the plume for which impingement heating data was taken in the larger portion of the total energy flux.

A large portion (75%) of the impingement heating rate data measurements were taken in the shear region of the plume, although the data comparisons were made using the inviscid plume results. The data shown that are not in the shear layer are: $x/D = 5, \alpha = 45, x = -0.5$ ft; $x/D = 12, \alpha = 45, x = -0.5$ and 0.5; $x/D = 20, \alpha = 30$ and 45, $x = -0.5$ ft. All of the 90 deg impingement heating data at $x/D = 20$ is in the shear region. The shear layer will affect the data comparison for all cases since the large shear region will be captured by the plate and flow down the plate.

The effect of the standoff shock on the heating rate predictions to the plate is probably very important. All the heating and pressure calculations made with the PLIMP code assume that the shock is parallel and close to the surface being impinged upon. Most of the heating rate data was taken on a region of the plate where the shock is at a higher angle than predicted and is located a considerable distance away from the surface. There is strong coupling between the gas and particle phases downstream of the shock. The gas-particle coupling results in local particle energy fluxes which are probably significantly different than those predicted in the undisturbed flow field. The effects of this coupling increase with increasing aluminum loading.

The previously mentioned factors and the large number of particles which are captured by the plate and flow down the plate severely complicate the analysis to calculate heating rates to a large surface impinged upon by a small two-phase plume. It was therefore difficult to calculate a consistent set of accommodation coefficients that would result in good data agreement for all points.

It should be noted that despite the complicating factor in the heating analysis, the results of the 2% aluminum cases in the inviscid region were fairly good. These results would give some credence to previous calculations made for the Space Shuttle separation motor impingement.

4. CONCLUSIONS

The following conclusions were drawn from the results of the post-test analysis:

- Overall, the RAMP numerical flowfield solution adequately predicts gasdynamic properties in the inviscid portion of two-phase exhaust plumes.
- Prediction of exhaust plume gas pressures requires an adequate model of the flowfield thermodynamics. The assumption of constant thermodynamic properties was found to be inadequate. Results indicated the expansions were chemically frozen. The gas thermodynamics were found to be a strong function of the change in entropy and gas total enthalpy levels caused by the momentum and energy exchange between the gas and particulate phases.
- Present methods of calculating mass mean particle sizes for small (L^* less than 100) solid propellant motors are marginal. Empirical data from Air Force test data proved adequate for predicting far-field plume energy fluxes. The commonly used nozzle throat diameter correlation with mass mean particle size is not applicable for nozzles with a throat diameter of less than 1 in.
- Analytical calculations assuming one particle size distributed over the exhaust plume flow field does not compare as well with experimental data as calculations assuming a log normal distribution of particle sizes about a mass mean size.
- Analytical calculations using the empirical particle drag model developed by Crowe do not produce as good of experimental/analytical data comparisons at low particle Reynolds number as calculations using the Kliegel drag model. At high propellant Al loadings, calculations using the Kliegel drag model overpredict two-phase momentum exchange at low particle Reynolds number and underpredict two-phase momentum exchange at high particle Reynolds number.
- Particle energy flux accommodation coefficient for plume energy fluxes is a strong function of particle mass flux. The magnitude of the accommodation coefficient varies inversely with particle mass flux.
- The PLIMP code adequately predicts impingement pressure on bodies at low angles of attack. Impingement pressure is a strong function of the impinged body shock structure. The PLIMP code

does not adequately model the body shock structure and thus the impingement environment of large bodies at high angles of attack in small plumes.

- Impingement energy fluxes are modified significantly by the shielding effect of the two-phase boundary layer on the impinged body. Analytical impingement energy flux calculations using the PLIMP code are conservative with respect to the actual environment experienced by the impinged body.

5. RECOMMENDATIONS

5.1 FURTHER INVESTIGATIONS

- Investigate the viscous exhaust plume phenomena observed in the test program.
- Investigate the two-phase phenomena downstream of normal and oblique shocks standing off impinged bodies.
- Develop an analytical model to adequately predict impingement environments experienced by bodies at high angles of attack with respect to the impinging exhaust plumes.

5.2 ANALYTICAL PROCEDURE

- Generate thermodynamic properties assuming an equilibrium chemistry model with a chemical freeze point.
- Use multiple tables of thermodynamic properties. The tables should be expanded from chamber conditions corresponding to several chamber enthalpies and two entropy levels for each chamber enthalpy. The range of total enthalpies and entropies should encompass the range of values calculated for the two-phase expansion.
- Use the Kliegel drag model to calculate particle drag coefficients.
- For nozzles with a throat diameter greater than one inch, calculate the mass mean particle diameter with the throat diameter correlation (Ref. 8).
- For nozzles with a throat diameter less than one inch, calculate the mass mean particle diameter based on motor L^* (Ref. 11).
- Model the distribution of particle sizes with a log normal distribution about the mass mean diameter.
- Use Fig. 60 to determine the accommodation coefficient for predicting exhaust plume heating rates from calculated values.

REFERENCES

1. Penny, M.M., S.D. Smith et al., "Supersonic Flow of Chemically Reacting Gas-Particle Mixtures — Vol. II — RAMP a Computer Code for Analysis of Chemically Peacting Gas-Particle Flows," LMSC-HREC TR D496555-II, Lockheed Missiles & Space Company, Huntsville, Ala., January 1976.
2. Tevepaugh, J.A., M.M. Penny and S.D. Smith, "Two-Phase Verification Test Program — Pretest Analysis," LMSC-HREC TM D390903, Lockheed Missiles & Space Company, Huntsville, Ala., August 1975.
3. Hair, L.M., and R.E. Somers, "Test Data from Small Solid Propellant Rocket Motor Plume Measurements," TRT 016-4, REMTECH Inc., Huntsville, Ala., June 1976.
4. Sulyma, P.R., and L.R. Baker, "User's Guide for TRAN72 Computer Code Modified for Use with RAMP and VOFMOC Flowfield Codes," LMSC-HREC TM D390409, Lockheed Missiles & Space Company, Huntsville, Ala., October 1974.
5. McBride, Bonnie J., and Gordon Sanford, "Computer Program for Calculation of Complex Chemical Equilibrium Compositions, Rocket Performance, Incident and Reflected Shocks and Chapman-Jouquet Detonations," SP-273, NASA-Lewis Research Center, Cleveland, Ohio, 1971.
6. Stull, D.R., and H. Prophet, "JANNAF Thermochemical Tables — Second Edition," National Bureau of Standards, Washington, D.C., June 1971.
7. Kliegel, J.R., and G.R. Nickerson, "Axisymmetric Two-Phase Perfect Gas Performance Program, Vol. I," NASA CR 92069, April 1967.
8. Delaney, Lawrence J., "Particle Characteristics in Two-Phase Plumes," Martin Marietta Corporation, Friendship International Airport, Md.
9. Smith, S.D., "Description of a Computer Program to Prepare an Axisymmetric Flowfield Tape for the Gaseous Radiation Program," LMSC-HREC D225763, Lockheed Missiles & Space Company, Huntsville, Ala., March 1972.
10. Wojciechowski, C.J., and M.M. Penny, "Development of High Altitude Plume Impingement Analysis for Calculating Heating Rates, Forces and Moments," LMSC-HREC D162867-I, Lockheed Missiles & Space Company, Huntsville, Ala., March 1971.
11 Coats, D.E. et al., "A Computer Program for the Prediction of Solid Propellant P ket Motor Performance, Vol. I," AFRPL-TR-75-36, Wright-Patterson AFB, Ohio, July 1975.
12. Crowe, C.J., "Drag Coefficients of Particles in a Rocket Nozzle," AIAA J., Vol. 5, No. 5, May 1967.

Table 1

PROPELLANT FORMULATIONS

Propellant	Component	Percent by Weight
2% Aluminum	Aluminum	2.00
	AP	82.00
	HTPB Binder	11.35
	MT4 Binding Agent	0.15
	IPDI Curing Agent	1.00
	Polybutene Plasticizer	3.50
10% Aluminum	Aluminum	10.00
	AP	74.00
	HTPB Binder	11.35
	MT4 Binding Agent	0.15
	IPDI Curing Agent	1.00
	Polybutene Plasticizer	3.50
15% Aluminum	Aluminum	15.00
	AP	69.00
	HTPB Binder	11.35
	MT4 Binding Agent	0.15
	IPDI Curing Agent	1.00
	Polybutene Plasticizer	3.50

Table 2

CROSS-REFERENCE GUIDE OF FIGURE NUMBERS FOR FIGURES WITH ANALYTICAL AND EXPERIMENTAL PITOT PRESSURE COMPARISONS

	x/D_{exit} =	5	12	16	20
Altitude	50,000 ft	41, 42	——	——	——
	100,000 ft	19, 20, 21, 40	23, 34, 35, 36	30, 33	18, 30, 31, 32
	112,000 ft	——	37, 38, 39	——	——
Aℓ Propellant Loading	2%	41	23, 34, 37	30	18, 23, 30
	10%	19, 20, 21, 40 42	35, 38	33	31
	15%	40, 41, 42	36, 39	——	32

Table 3

CROSS-REFERENCE GUIDE OF FIGURE NUMBERS FOR FIGURES WITH ANALYTICAL AND EXPERIMENTAL HEATING RATE COMPARISONS

	x/D_{exit} =	5	12	16	20
Altitude	50,000 ft	43	——	——	——
	100,000 ft	44, 45	46, 47, 48	52, 53	54, 55, 56
	112,000 ft	——	49, 50, 51	——	——
Aℓ Propellant Loading	2%		46, 49	52	54
	10%	44	47, 49	53	55
	15%	43, 45	48, 51	——	56

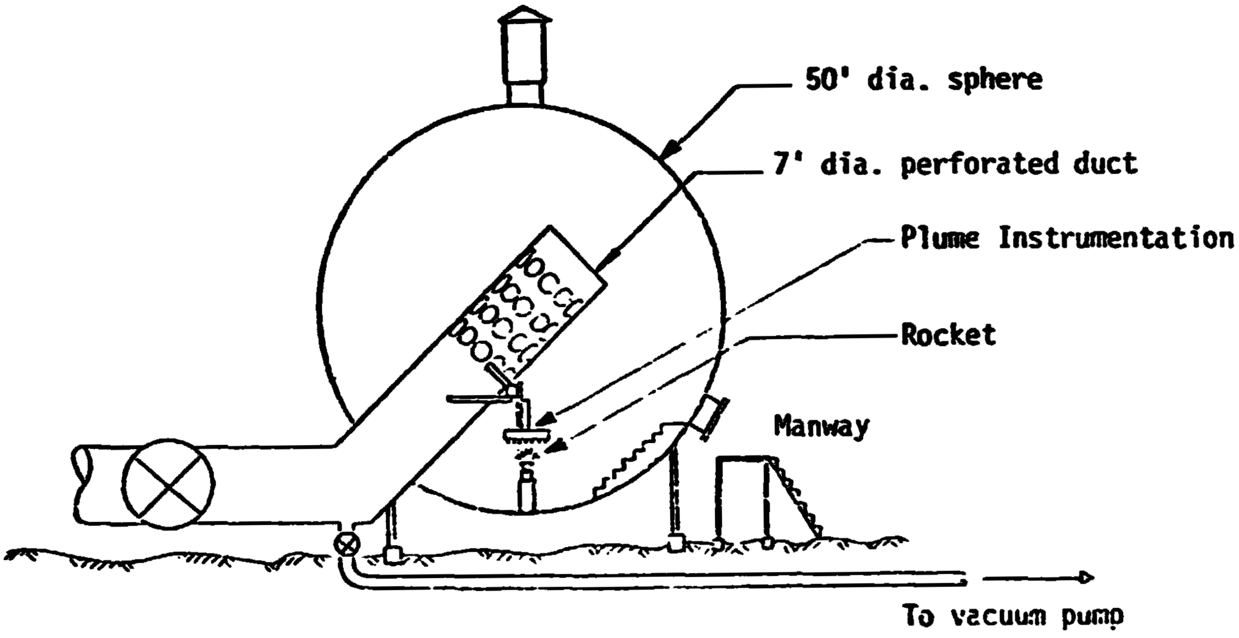

Fig. 1 - Test Facility (Ref. 3)

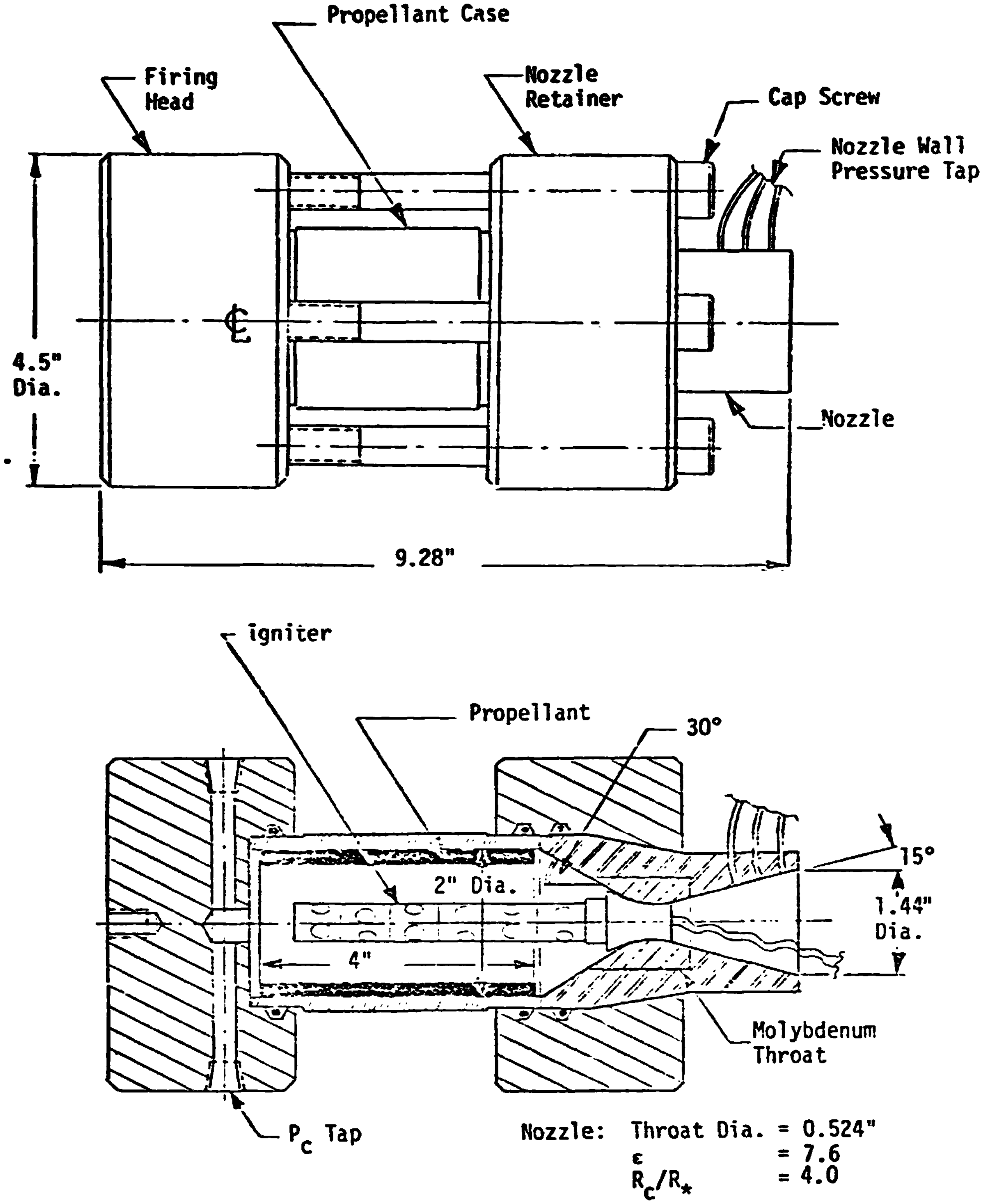

Nozzle: Throat Dia. = 0.524"

ε = 7.6

R_c/R_* = 4.0

Fig. 2 - Rocket Motor (Ref. 3)

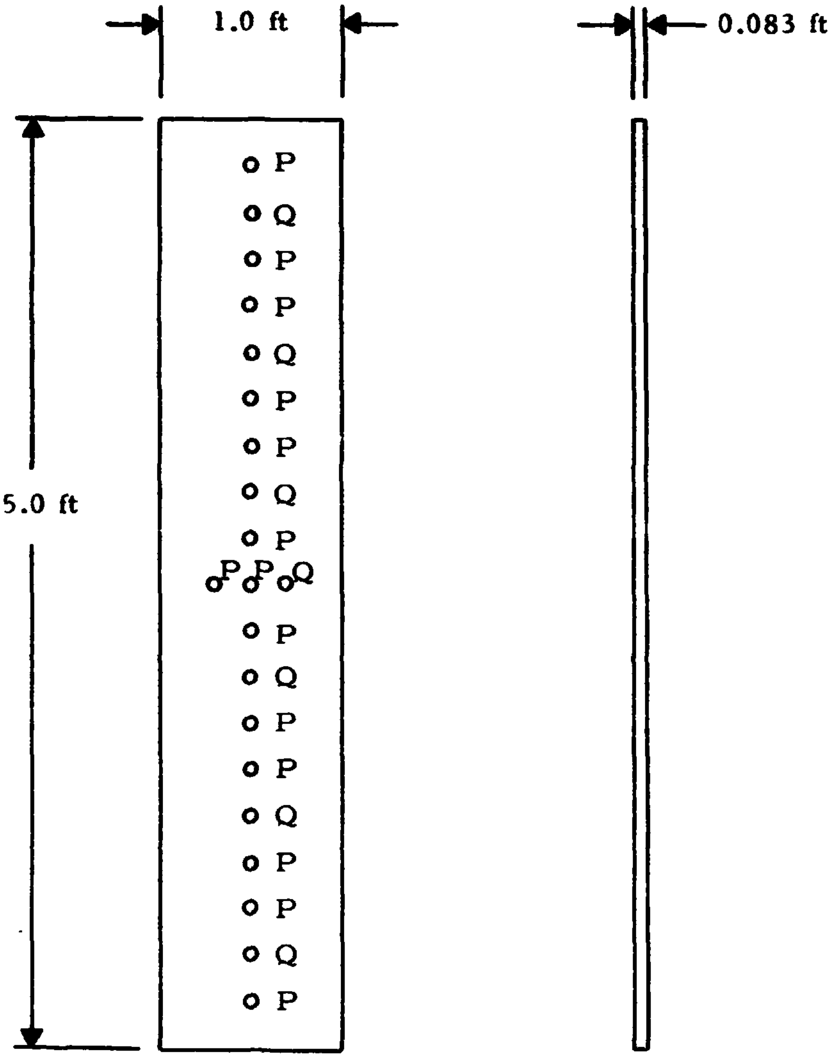

Note: P = pressure transducer; Q = heat rate gage.

Fig. 3 - Diagram of Flat Plate and Flat Plate Instrumentation

Simulated Altitude (ft)

○ 50,000

□ 100,000

◇ 112,000

	$x/D_{exit} = 5$			$x/D_{exit} = 12$			$x/D_{exit} = 16$		$x/D_{exit} = 20$		
Aluminum Loading	2%	10%	15%	2%	10%	15%	2%	10%	2%	10%	15%
Radial Surveys	○ ○	○ ○ □ □	○○○ □□	□ □ ◇	□ ◇ ◇	□□ ◇◇◇	□ □	□□□	□□□ ◇	□ □ ◇	□ □
Flat Plate $\psi = 30^o$									□□□	□ □	□ □
Flat Plate $\psi = 45^o$	○ ○ □ □	○ ○ □ □	○○ □□	□ □	□ □	□ □			□ □	□ □	□ □
Flat Plate $\psi = 60^o$									□ □	□ □	□ □
Flat Plate $\psi = 90^o$									□ □	□ □	□□□
Solid Propellant Capture				□ □	□	□			□ □	□ □	□ □

Fig.4 - Matrix of Test Conditions Investigated

REPRODUCIBILITY OF THE
ORIGINAL PAGE IS POOR

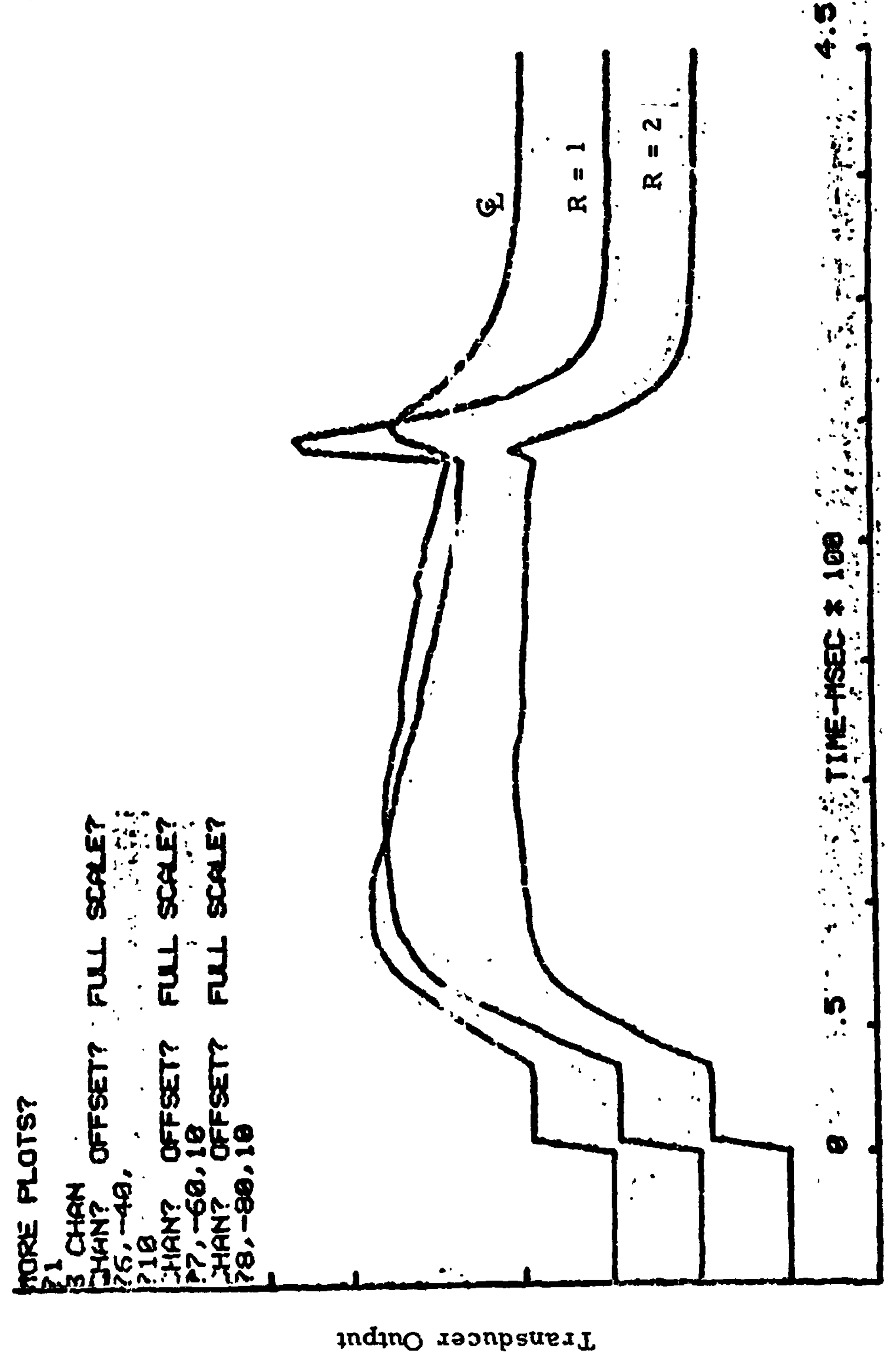

```
MORE PLOTS?
?1
3 CHAN
CHAN?  OFFSET?  FULL SCALE?
?6,-40,
?10
CHAN?  OFFSET?  FULL SCALE?
?7,-60,10
CHAN?  OFFSET?  FULL SCALE?
?8,-80,10
```

Fig. 5 - Pressure Transducer Output as a Function of Time for 10% Al Propellant

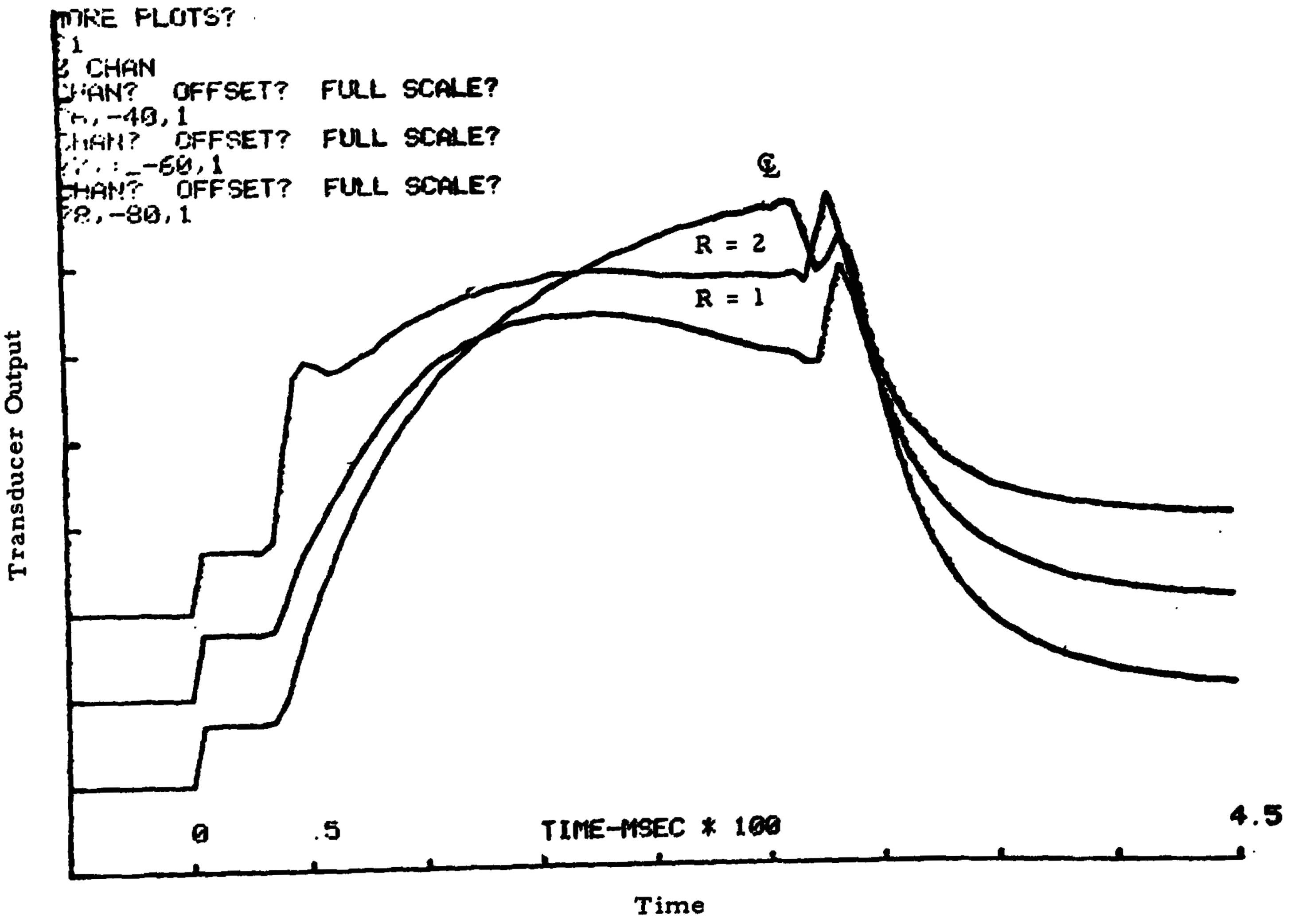

Fig. 6 - Pressure Transducer Output as a Function of Time for 15% Al Propellant

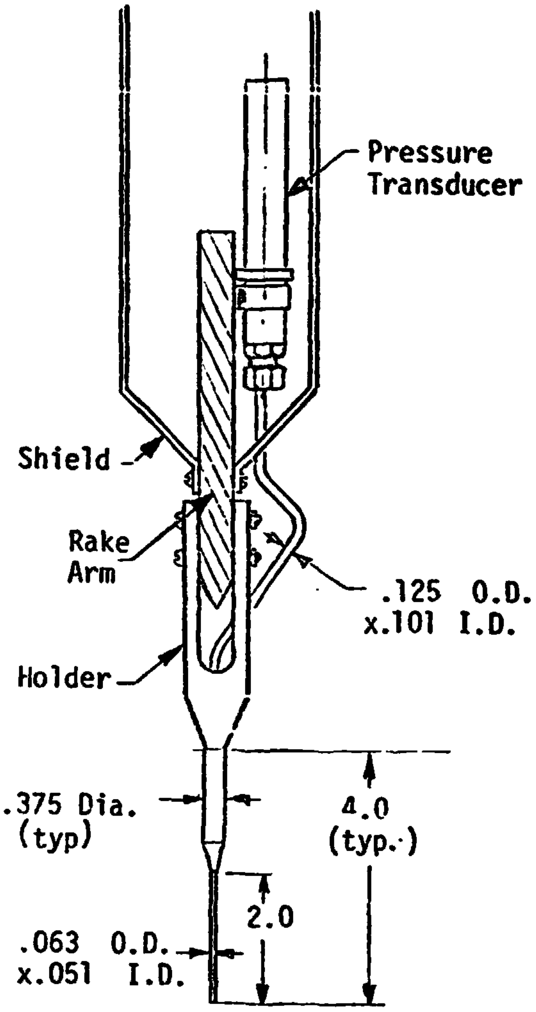

Fig. 7 - Pitot Pressure Probe Assembly (Ref. 3)

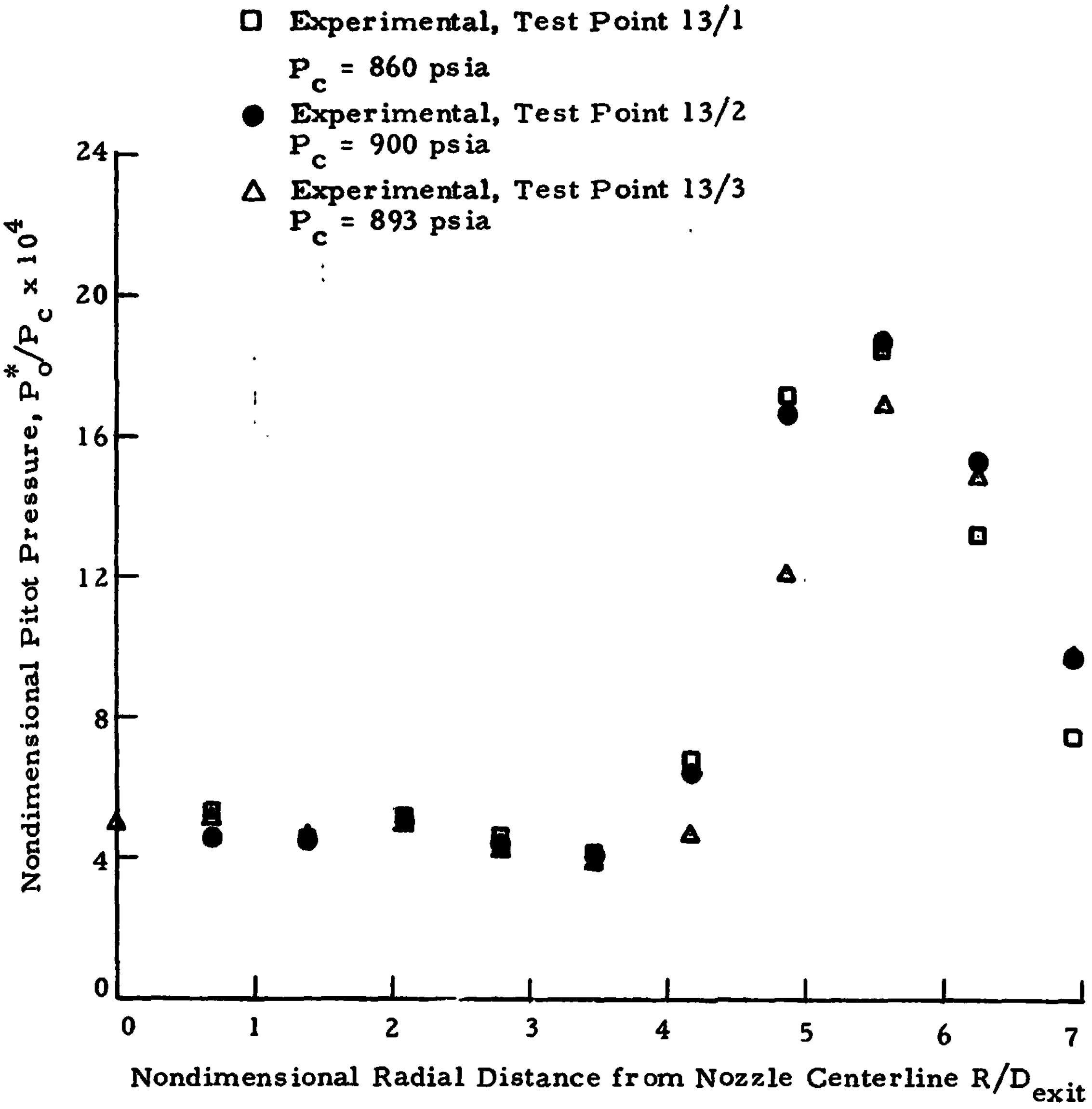

Fig. 8 - Radial Distributions of Nondimensional Pitot Pressure at x/D_{exit} = 16, 10% Aluminum Loading and an Altitude of 100,000 ft

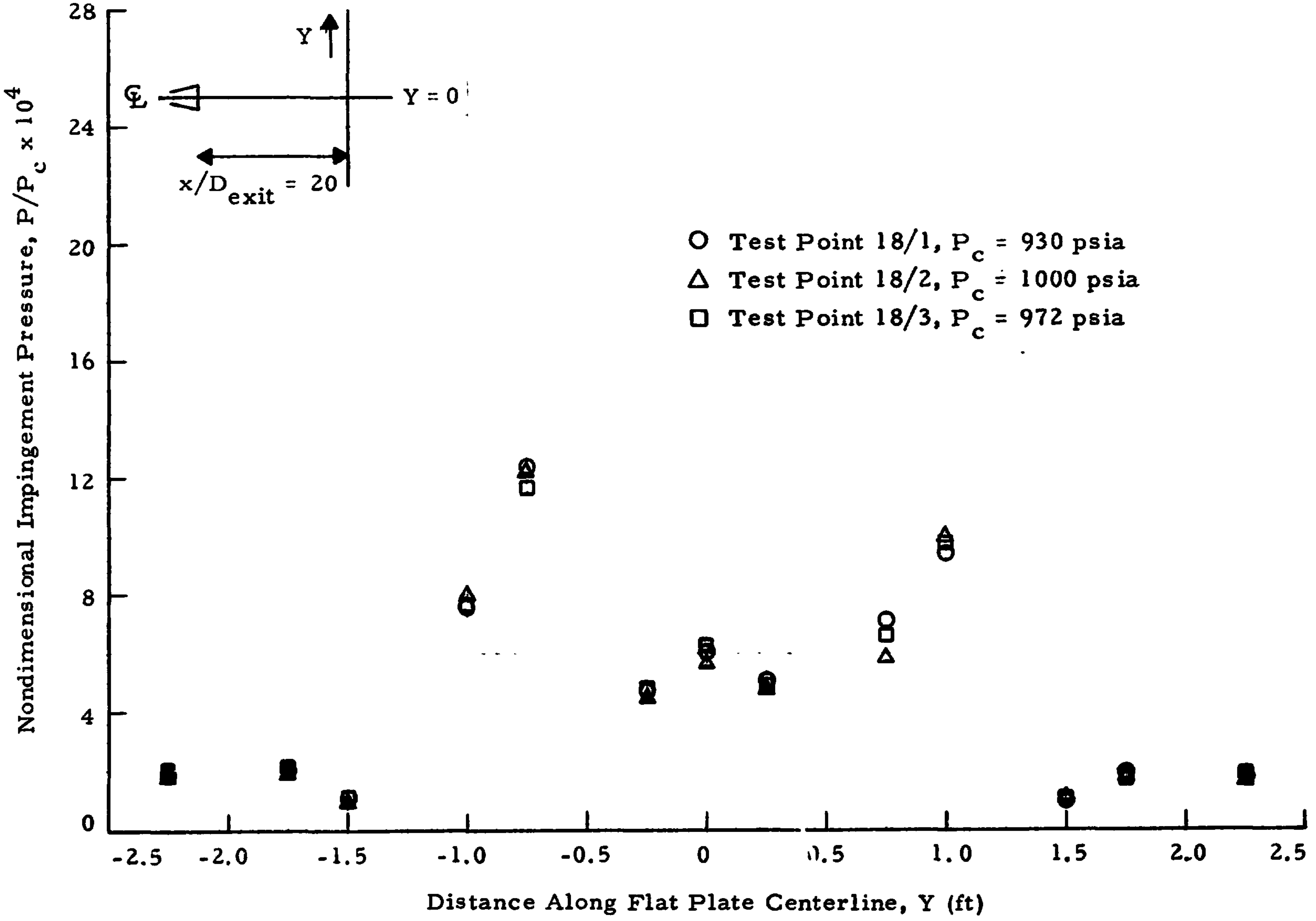

Fig. 9 - Nondimensional Impingement Pressure Along Flat Plate Centerline at x/D_{exit} 20, 15% Aluminum Loading and an Altitude of 100,000 ft

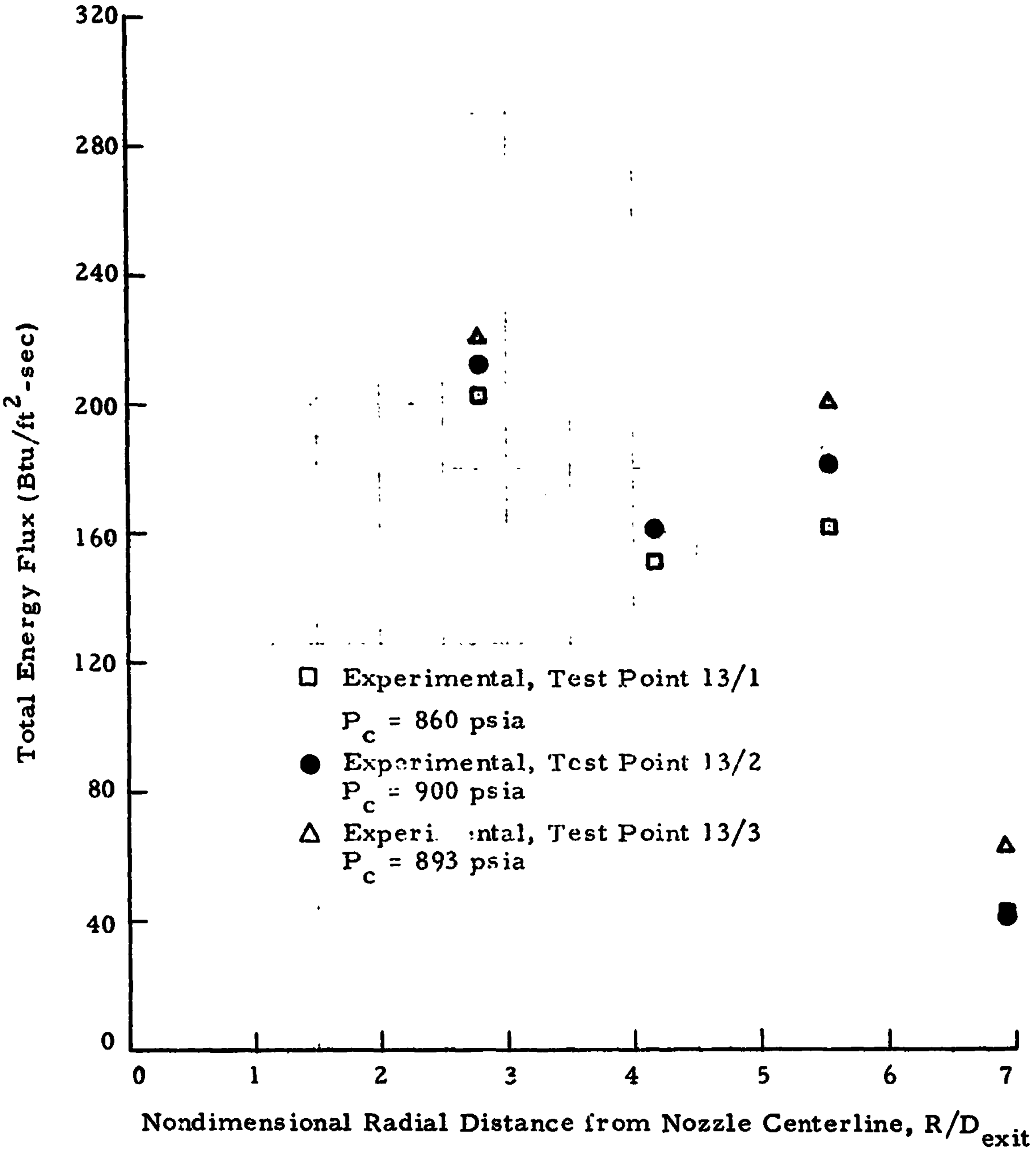

Fig. 10 - Radial Distributions of Total Energy Flux at x/D_{exit} = 16 for 10% Aluminum Loading and an Altitude of 100,000 ft

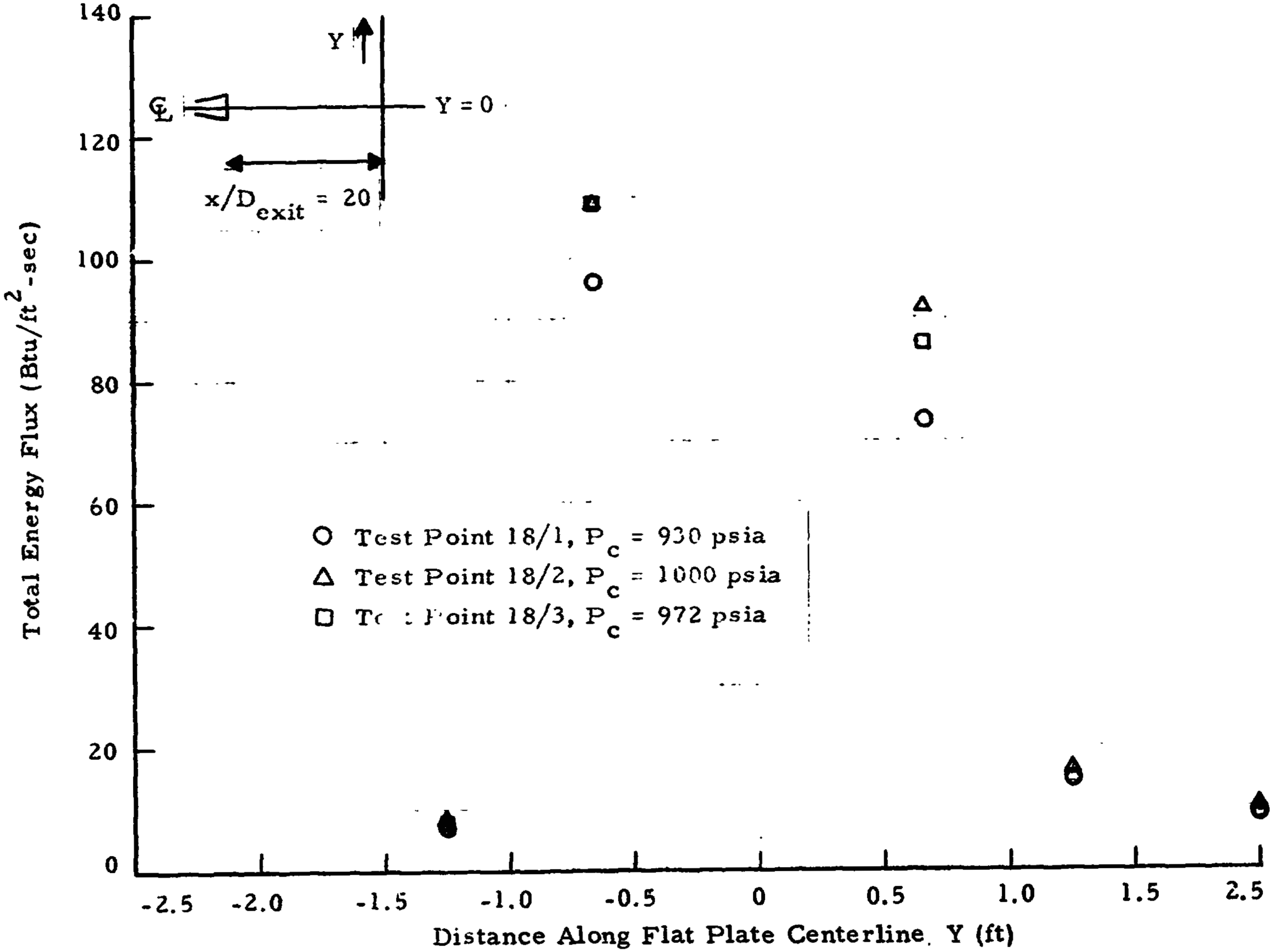

Fig. 11 - Total Energy Flux Along Flat Plate Centerline at x/D_{exit} = 20, 15% Aluminum Loading and an Altitude of 100,000 ft

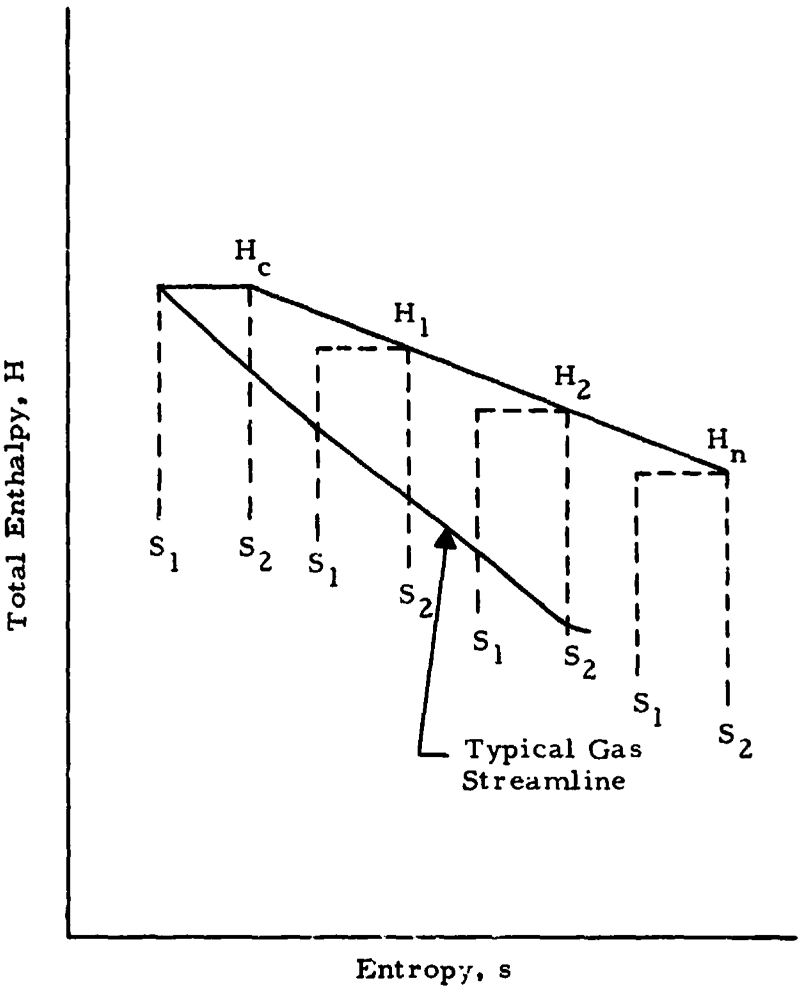

Fig. 12 - Thermodynamic Characteristics of Two-Phase Expansion and RAMP Thermochemical Table Construction

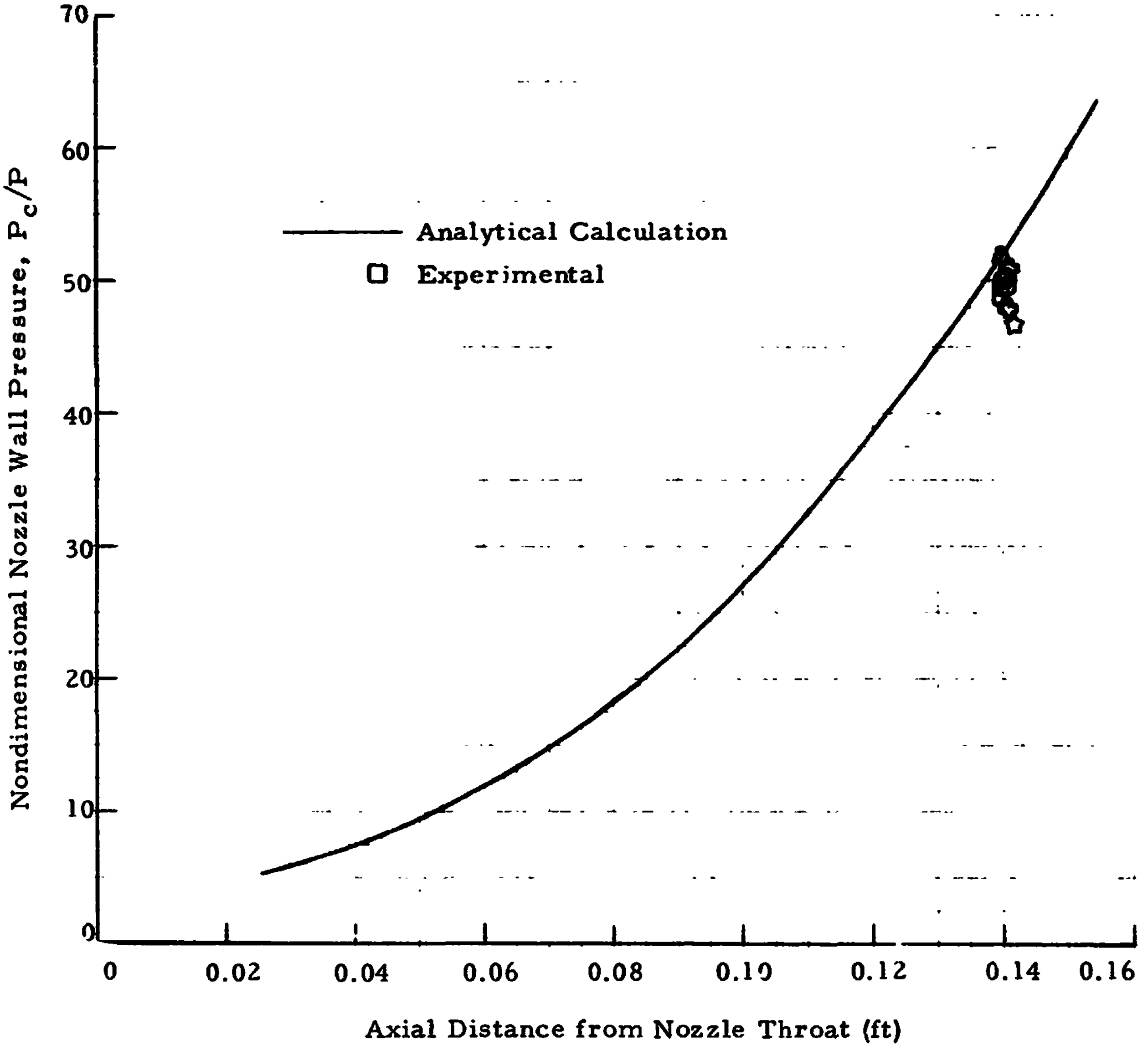

Fig. 13 - Comparison of Analytical Nozzle Wall Static Pressure with Experimental Pressure Measurements for Several Nozzles and 2% Al Propellant

REPRODUCIBILITY OF THE ORIGINAL PAGE IS POOR

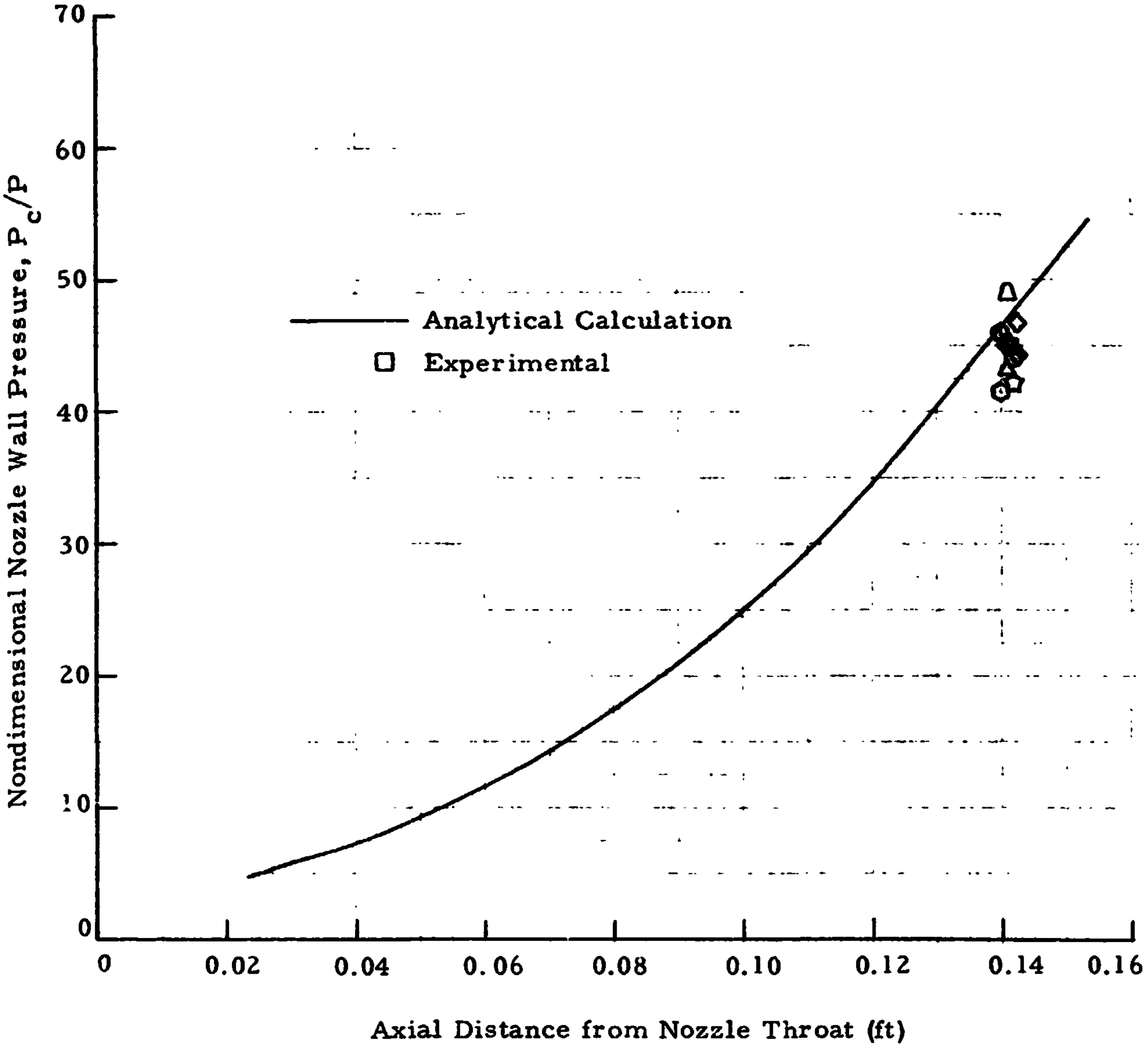

Fig. 14 - Comparison of Analytical Nozzle Wall Static Pressure with Experimental Pressure Measurements for Several Nozzles and 10% Al Propellant

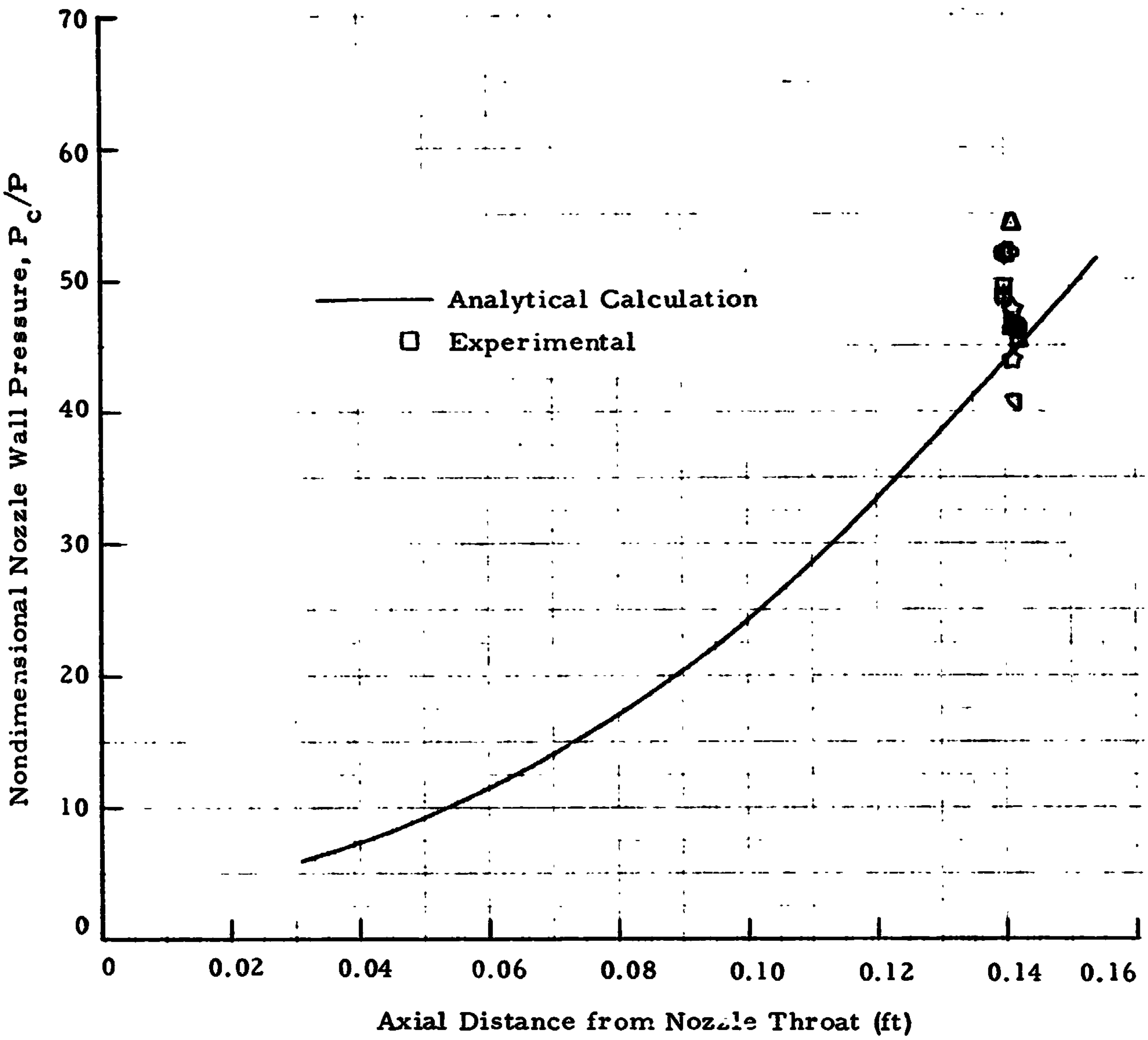

Fig. 15 - Comparison of Analytical Nozzle Wall Static Pressure with Experimental Pressure Measurements for Several Nozzles and 15% Al Propellant

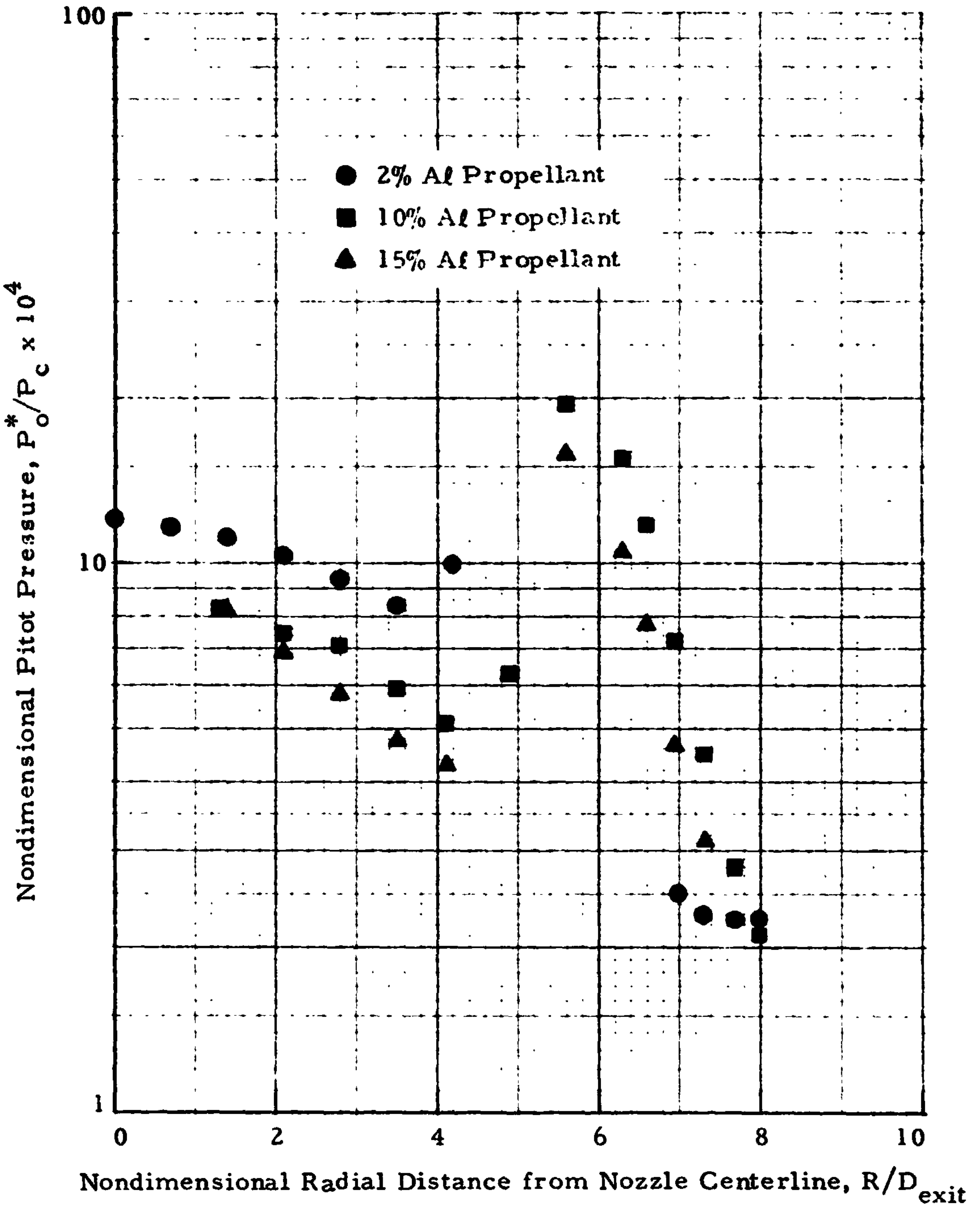

Fig. 16 - Radial Distributions of Experimental Pitot Pressure at x/D_{exit} = 12 and a Simulated Altitude of 100,000 ft

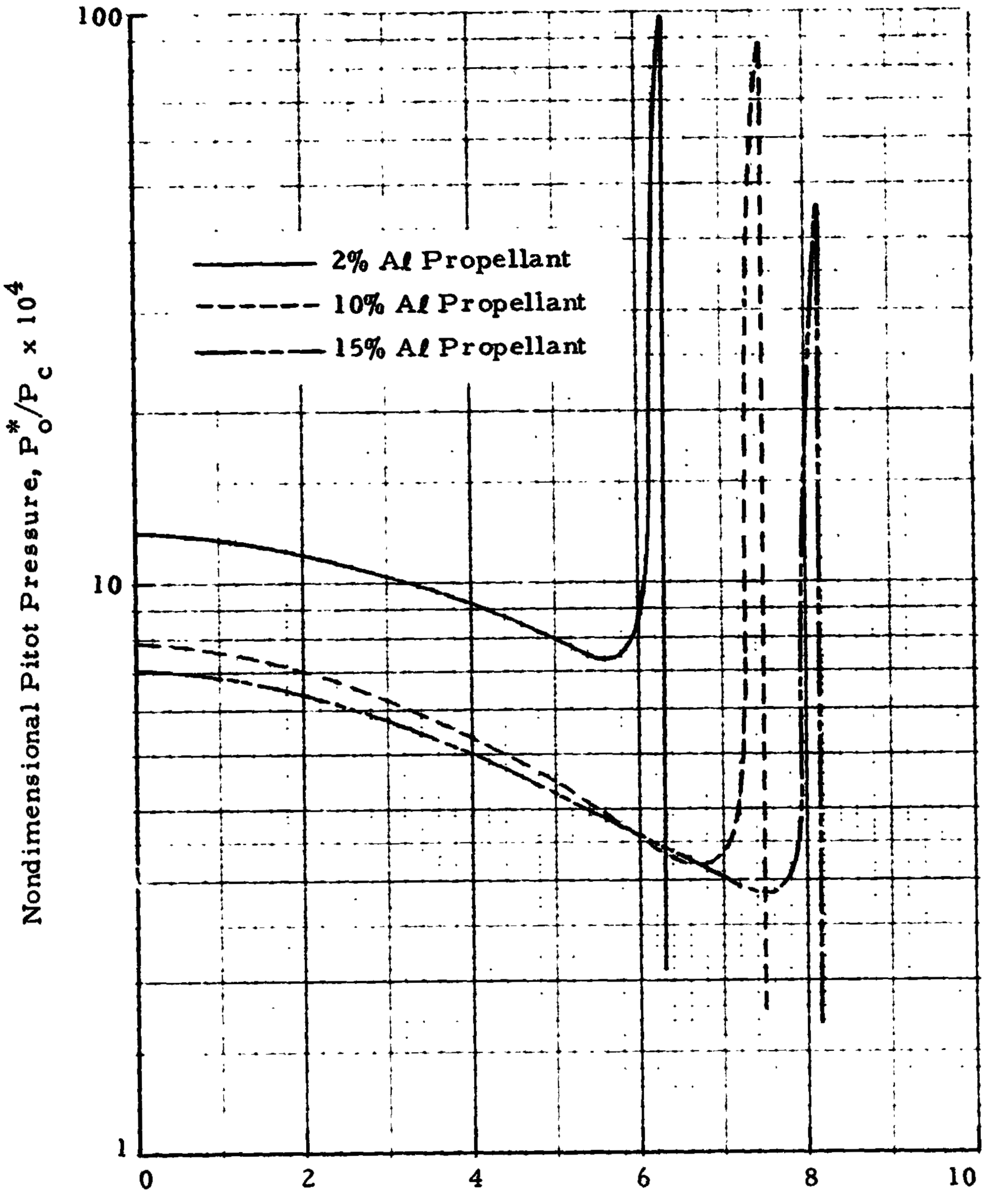

Fig. 17 - Radial Distributions of Analytical Pitot Pressure at $x/D_{exit} = 12$ and a Simulated Altitude of 100,000 ft

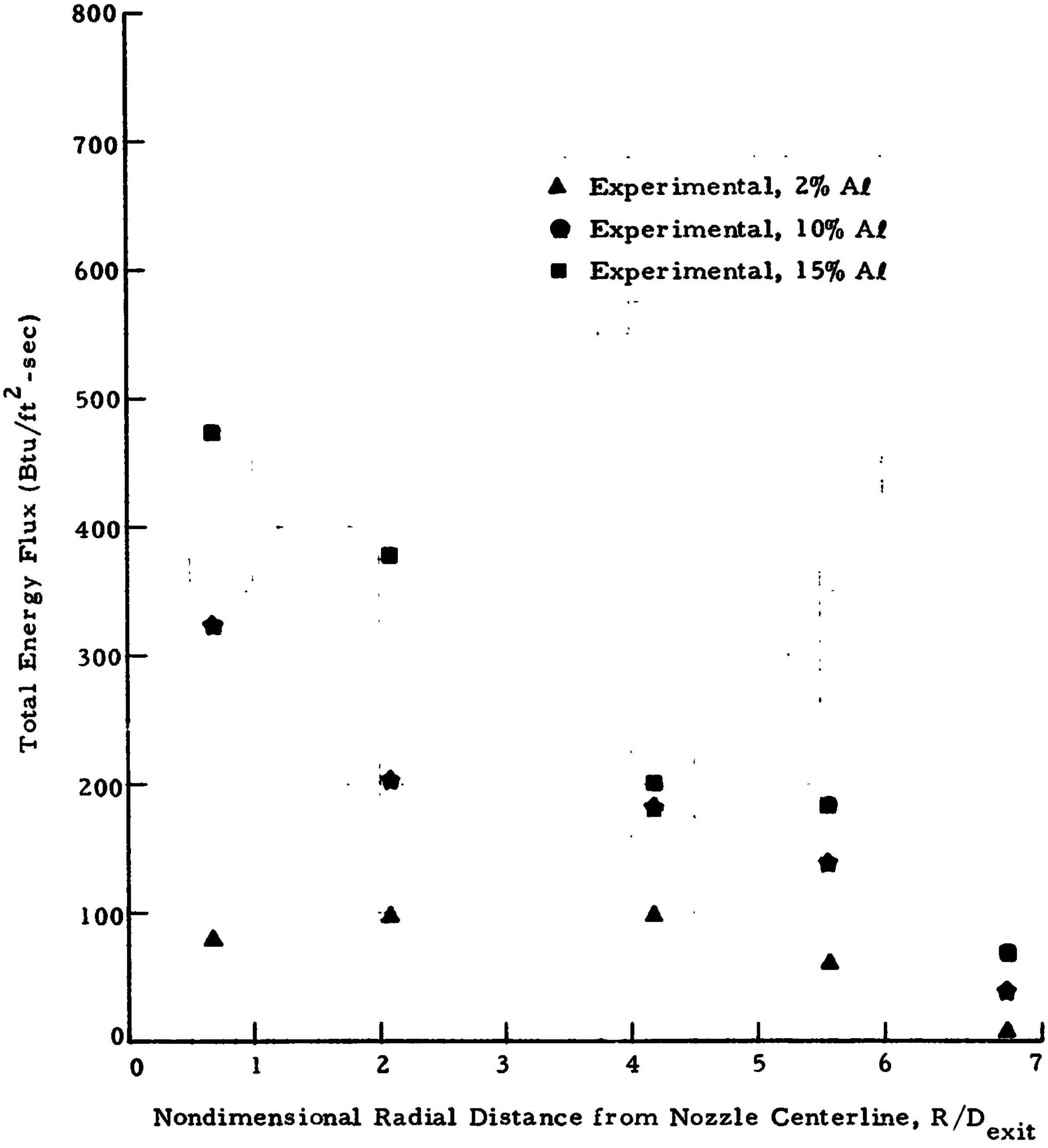

Fig. 18 - Radial Distributions of Measured Total Energy Flux for Various Propellant Al Loadings at x/D$_{exit}$ = 20 and a Simulated Altitude of 100,000 ft

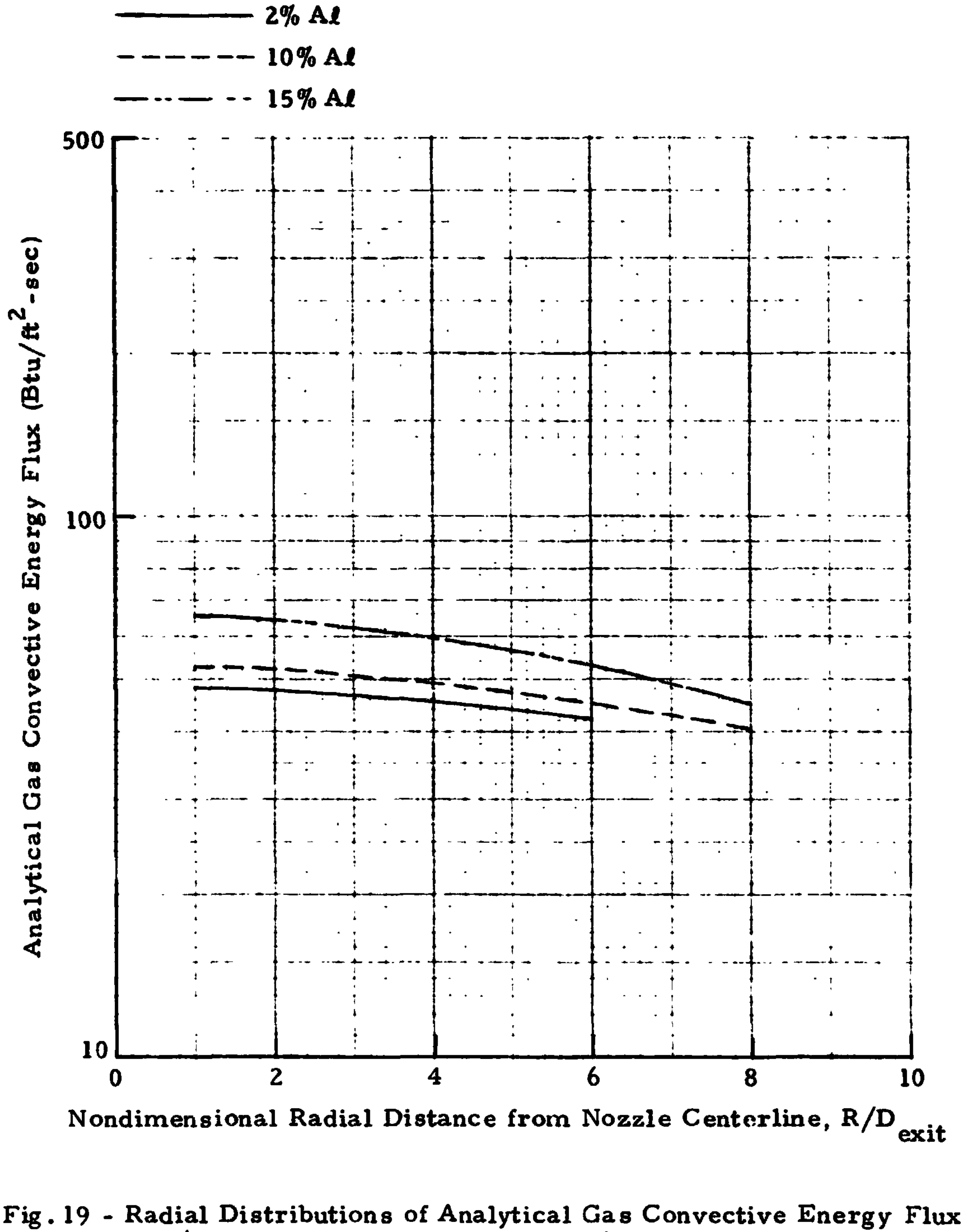

Fig. 19 - Radial Distributions of Analytical Gas Convective Energy Flux at $x/D_{exit} = 20$ for the 2, 10 and 15% Al Propellants at a Simulated Altitude of 100,000 ft

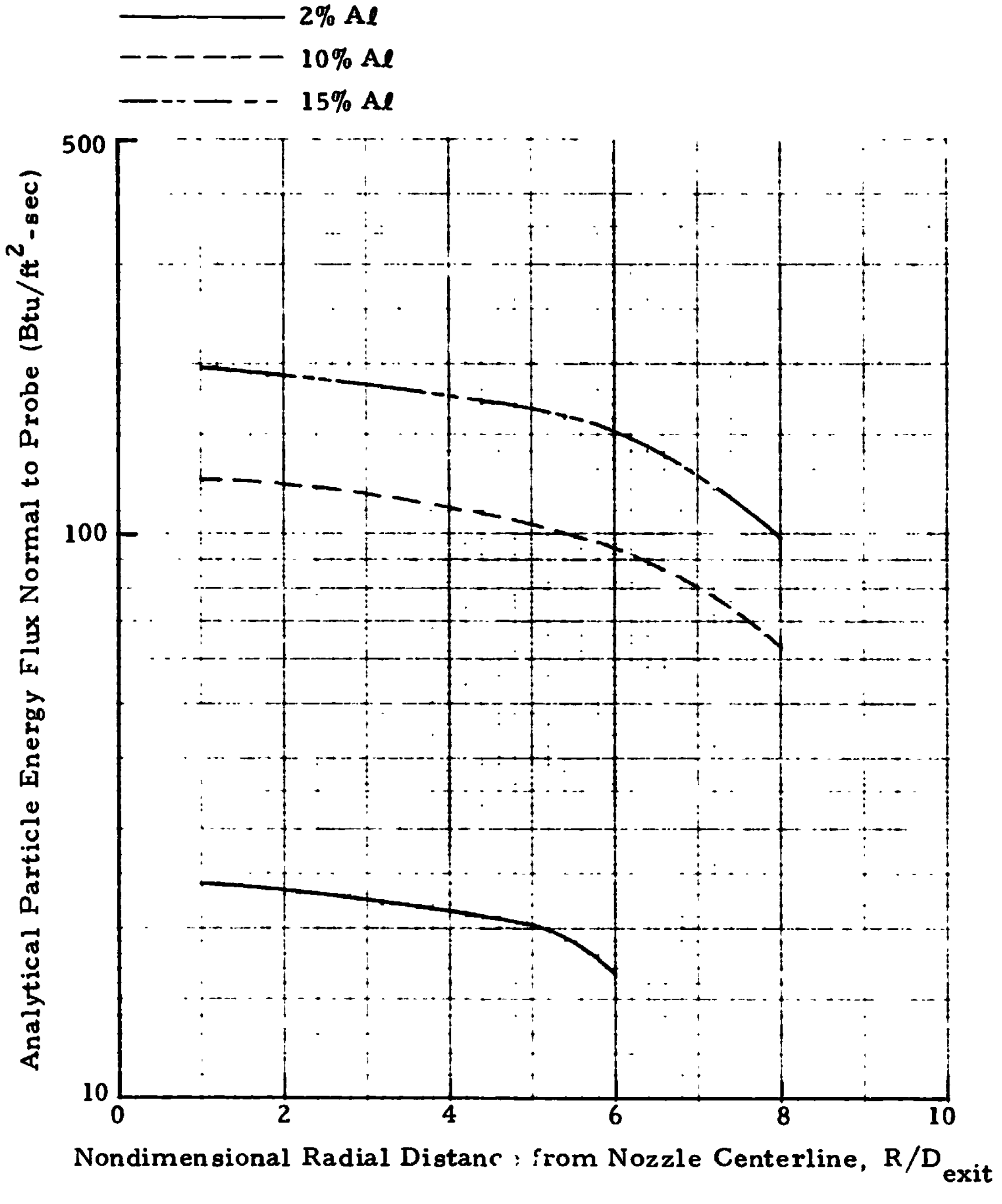

Fig. 20 - Radial Distributions of Analytical Particle Energy Flux Normal to Probes at $x/D_{exit} = 20$ for the 2, 10 and 15% Al Propellants at a Simulated Altitude of 100,000 ft

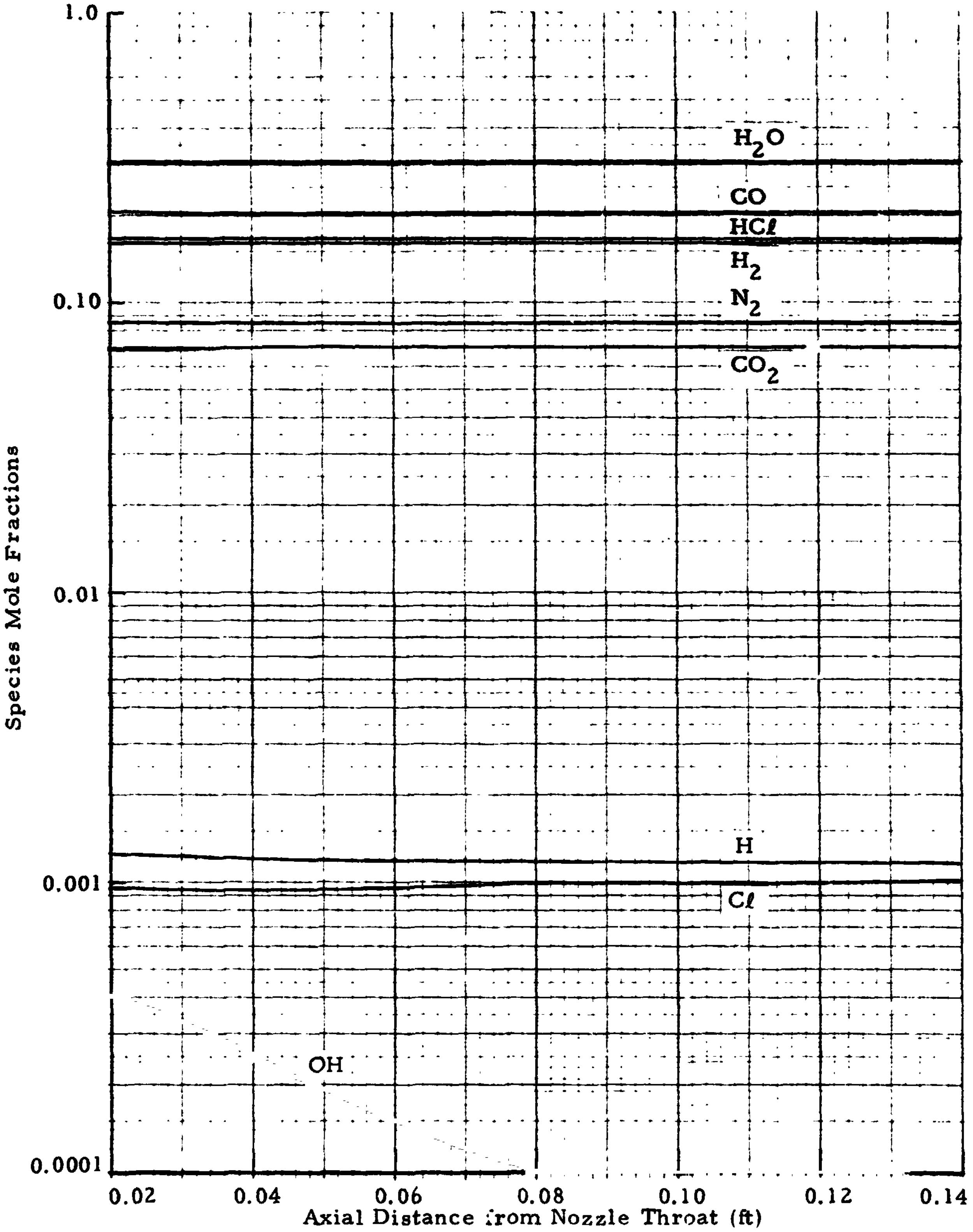

Fig. 21 - Species Mole Fractions Along Nozzle Centerline for 2% Aℓ Propellant Chamber Pressure of 783 psia, Nonequilibrium Chemistry

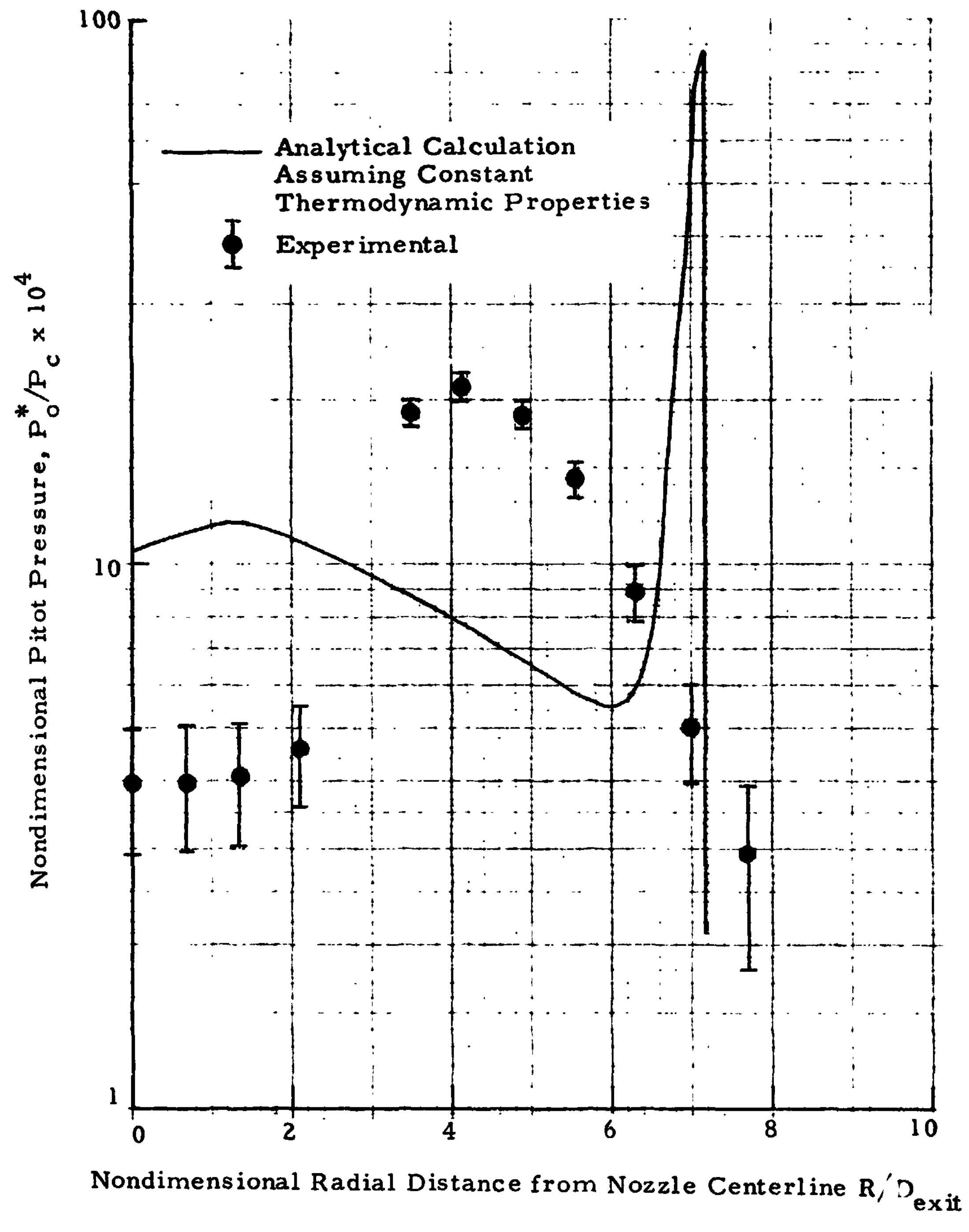

Fig. 22 - Comparison of Experimental and Analytical Pitot Pressure Distributions for the 2% Aℓ Propellant at x/D_{exit} = 20 and a Simulated Altitude of 100,000 ft

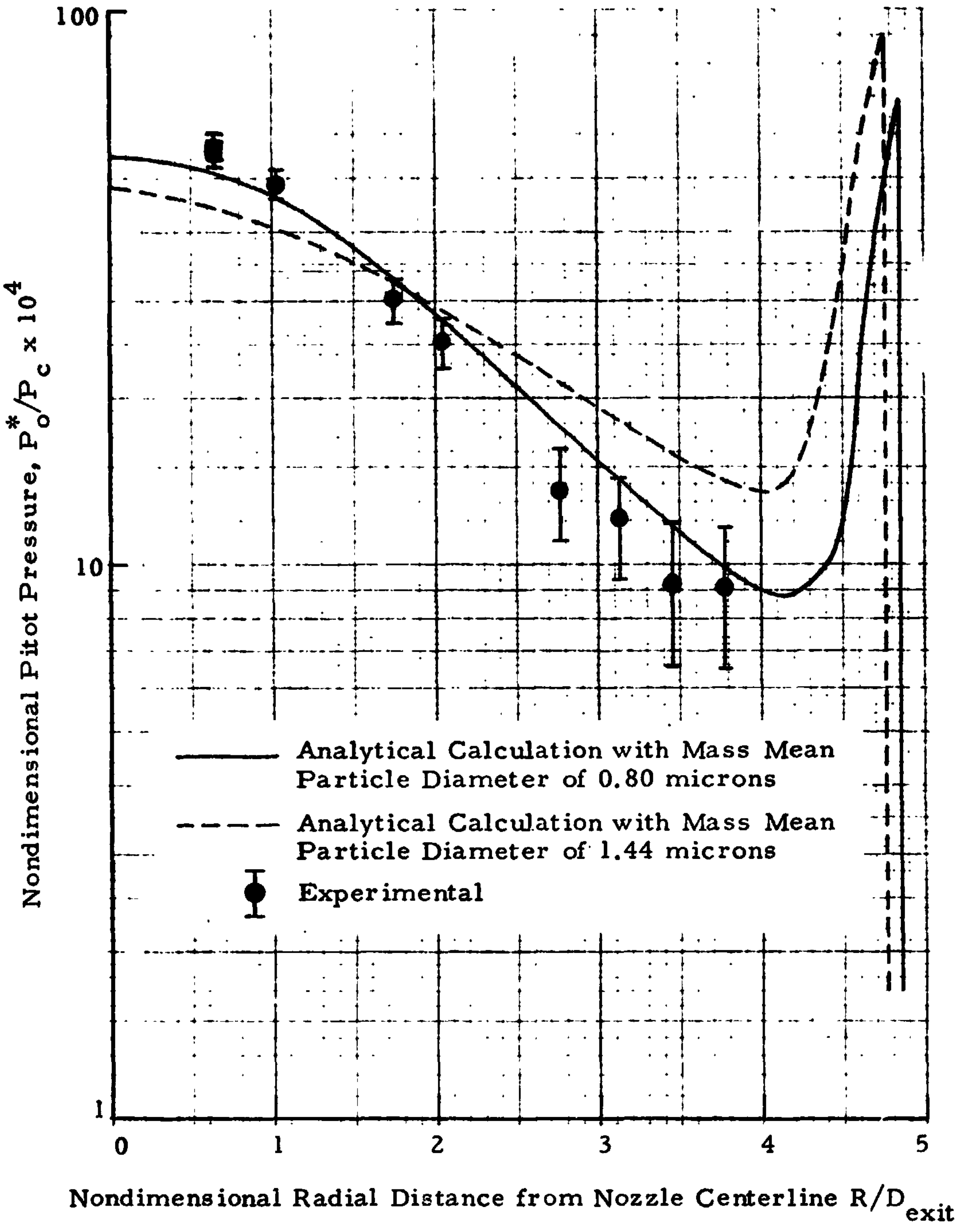

Fig. 23 - Comparison of Experimental Pitot Pressure Measurements with Analytical Calculations Using Log Normal Particle Size Distributions About Different Mean Particle Diameters for the 10% Aℓ Propellant at $x/D_{exit} = 5$ and a Simulated Altitude of 100,000 ft

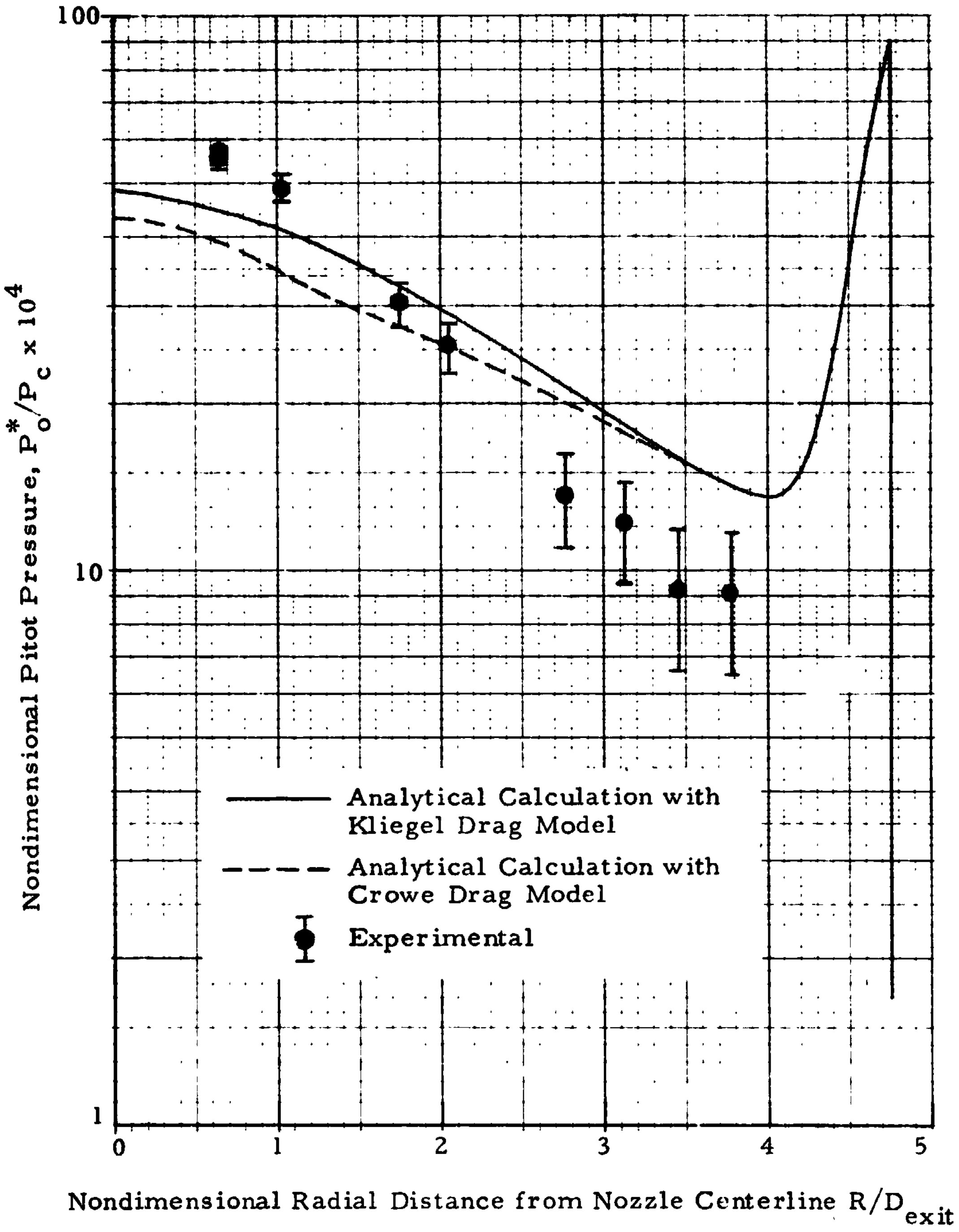

Fig. 24 - Comparison of Experimental Pitot Pressure Measurements with Analytical Calculations Using Different Empirical Particle Drag Models for the 10% $A\ell$ Propellant at $x/D_{exit} = 5$ and a Simulated Altitude of 100,000 ft

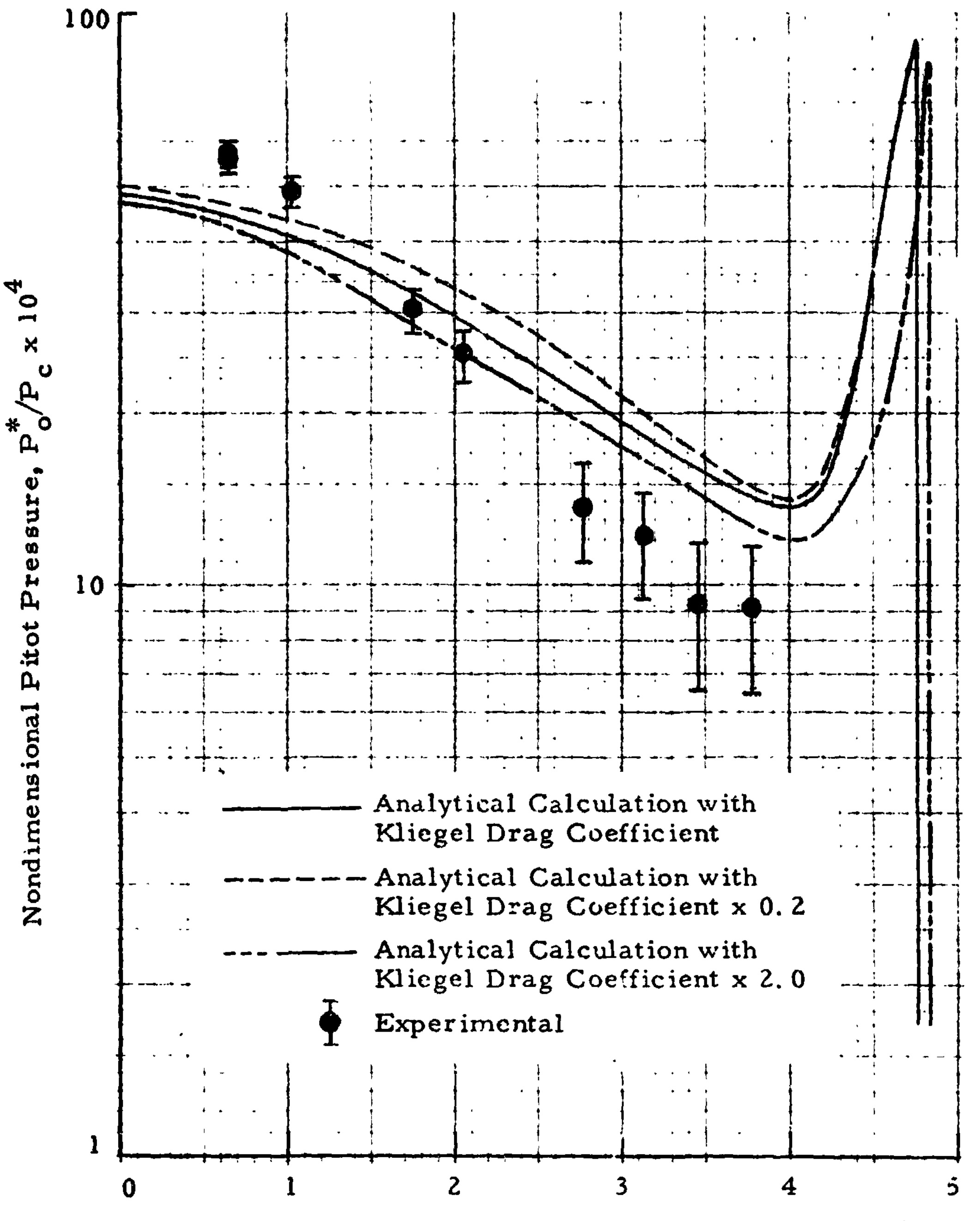

Fig. 25 - Comparison of Experimental Pitot Pressure Measurements with Analytical Calculations Using Different Values of Particle Drag Coefficient for the 10% Al Propellant at $x/D_{exit} = 5$ and a Simulated Altitude of 100,000 ft

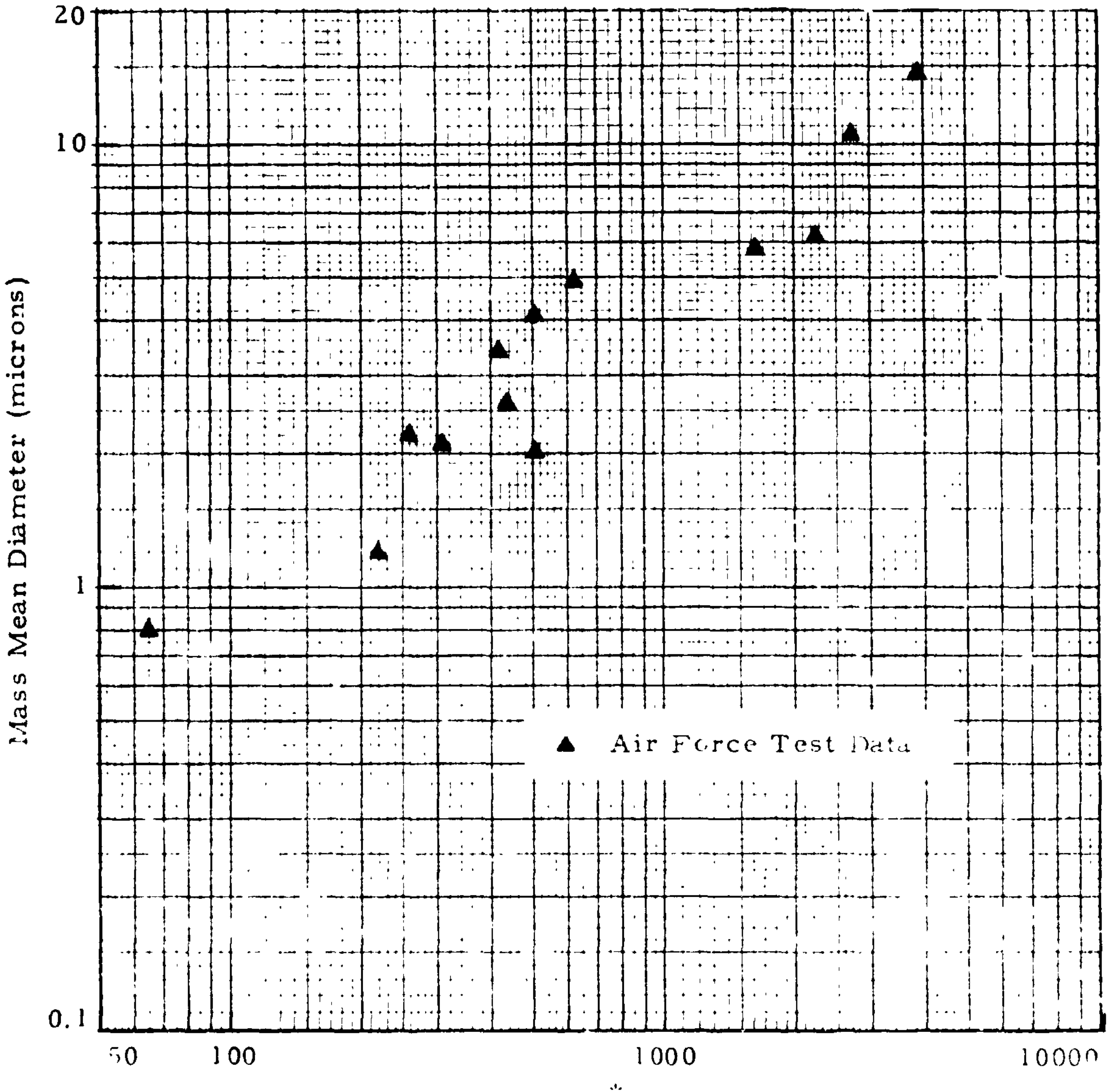

Fig. 26 - Mass Mean Particle Diameter as a Function of Motor, L*

REPRODUCIBILITY OF THE
ORIGINAL PAGE IS POOR

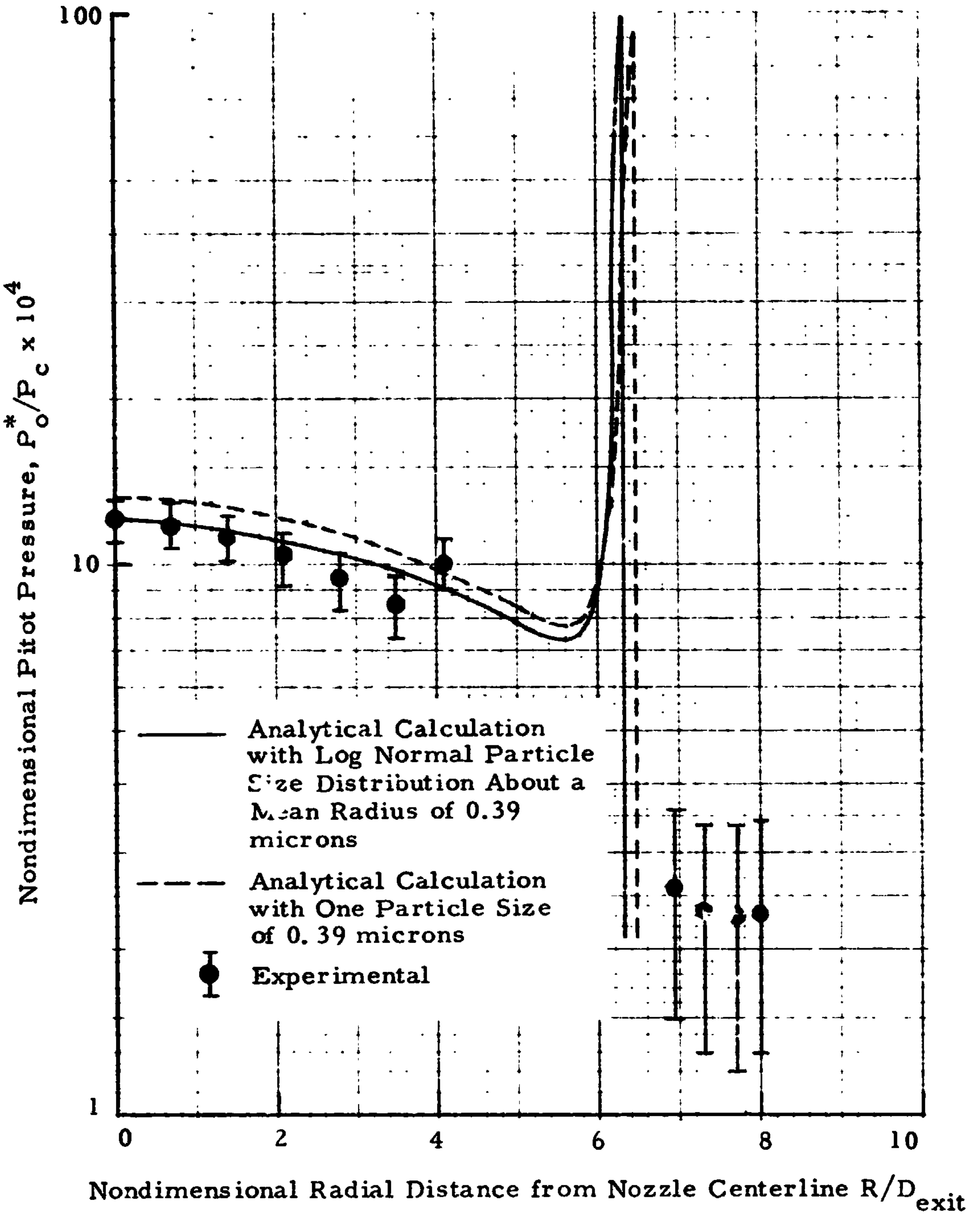

Fig. 27 Comparison of Experimental Pitot Pressure Measurements with Analytical Calculations Using Different Particle Size Distributions for 2% Aℓ Propellant at $x/D_{exit} = 12$ and a Simulated Altitude of 100,000 ft

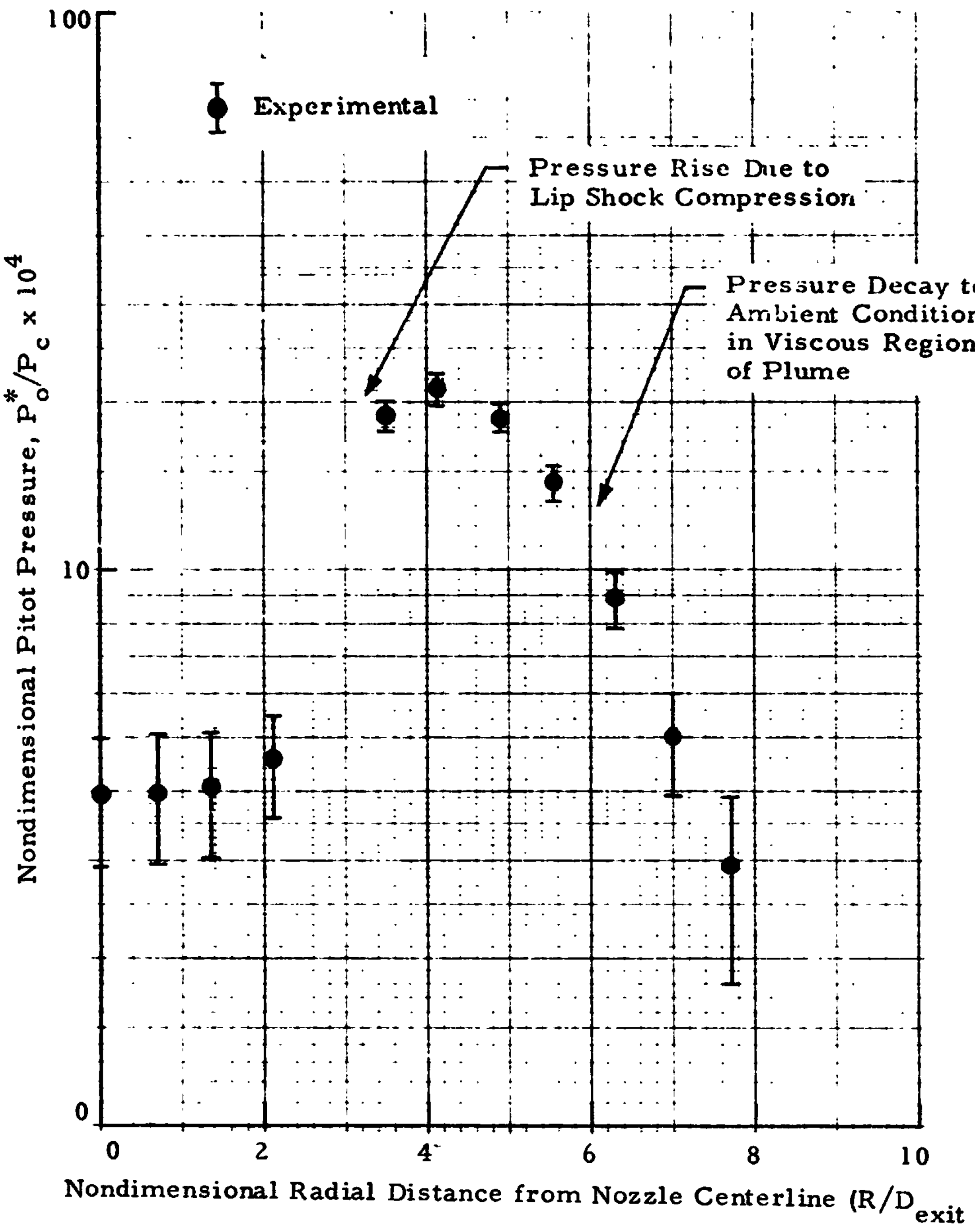

Fig. 28 Experimental Distribution of Pitot Pressure at $x/D_{exit} = 20$ for the 2% Al Propellant and a Simulated Altitude of 100, ft

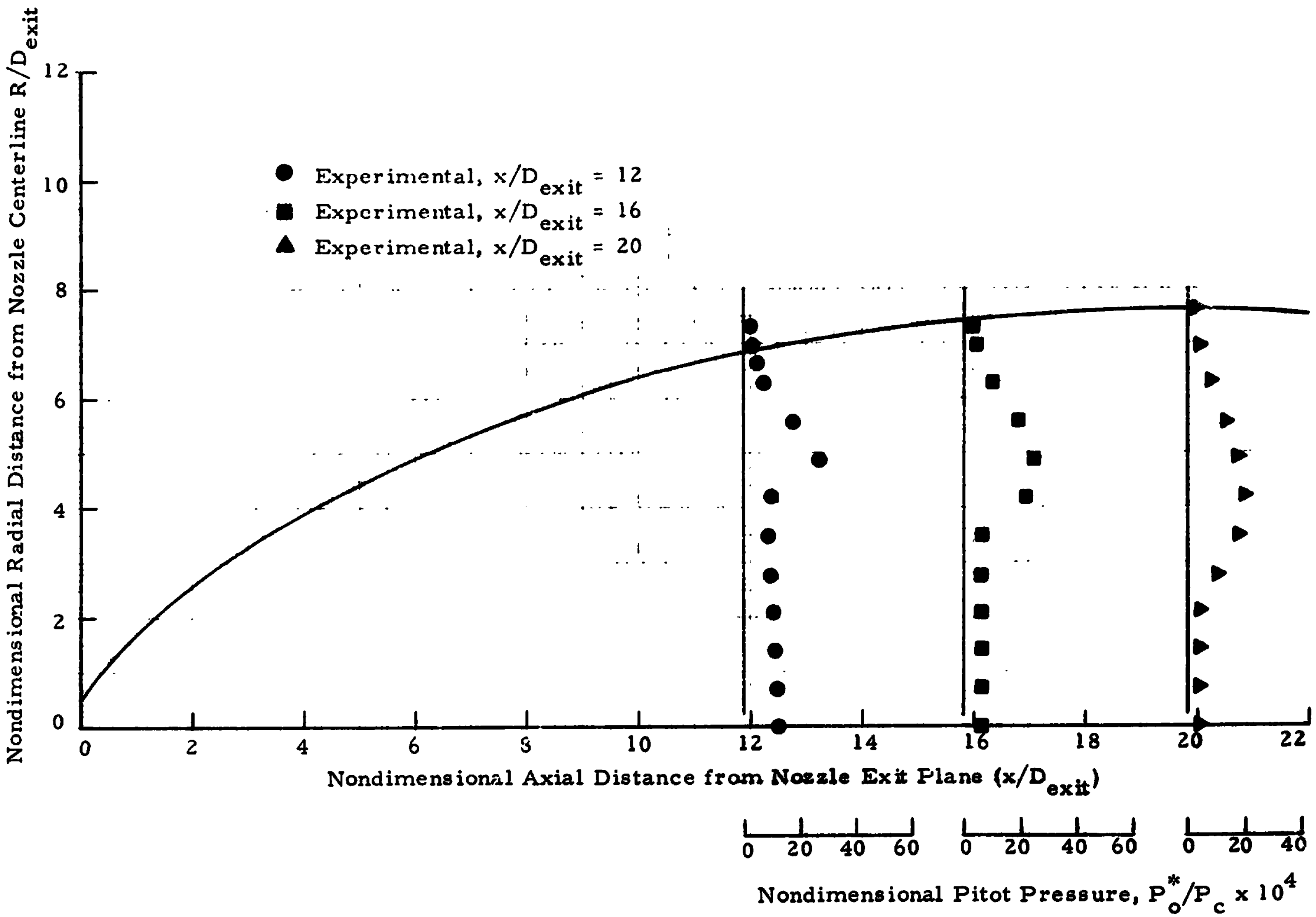

Fig. 29 - Radial Distributions of Nondimensional Pitot Pressure at $x/D_{exit} = 12, 16$ and 20 for 2% Al Propellant and a Simulated Altitude of 100,000 ft

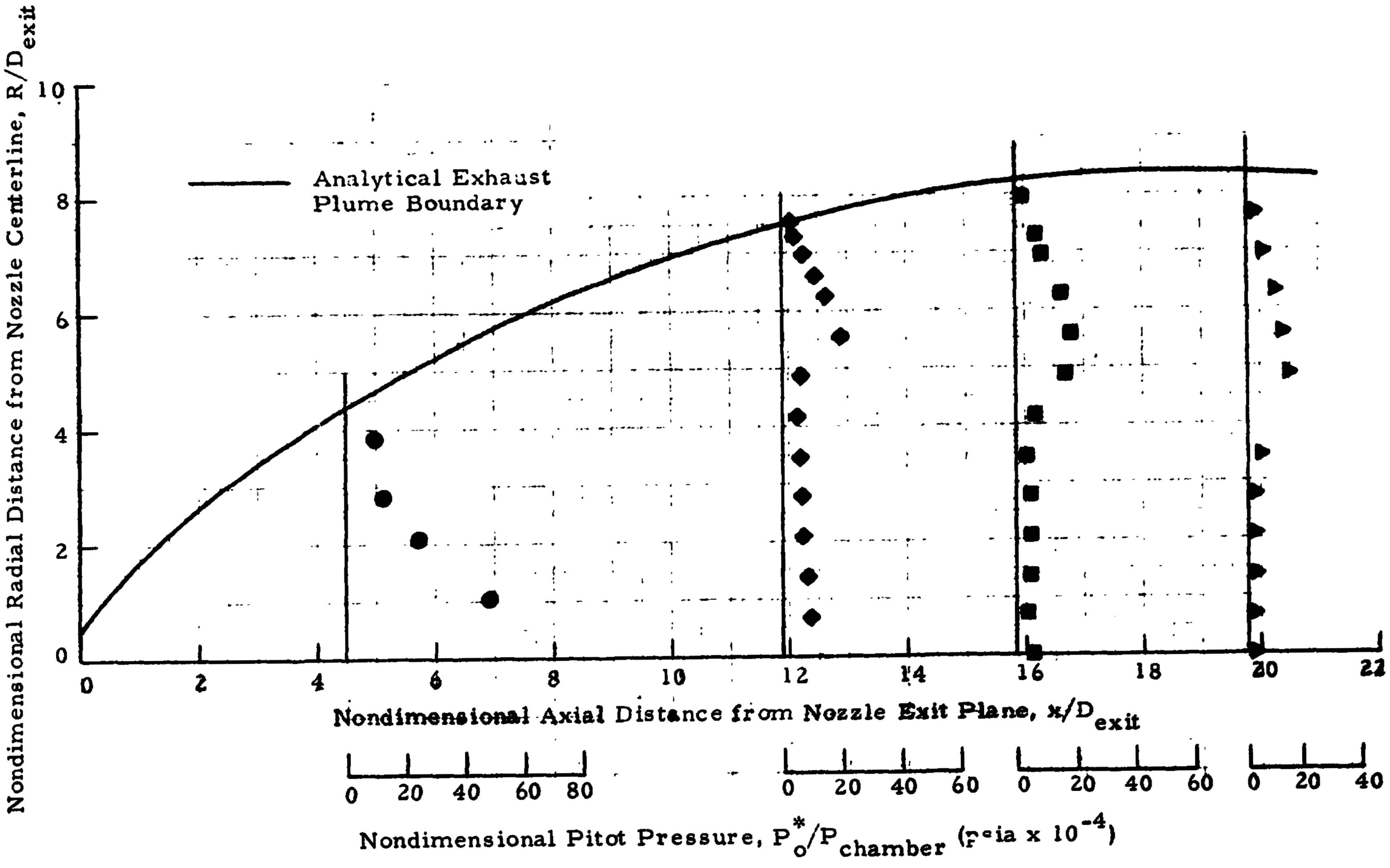

Fig. 30 - Radial Distributions of Nondimensional Pitot Pressure at x/D_{exit} = 5, 12, 16 and 20 for 10% Al Loading and an Altitude of 100,000 ft

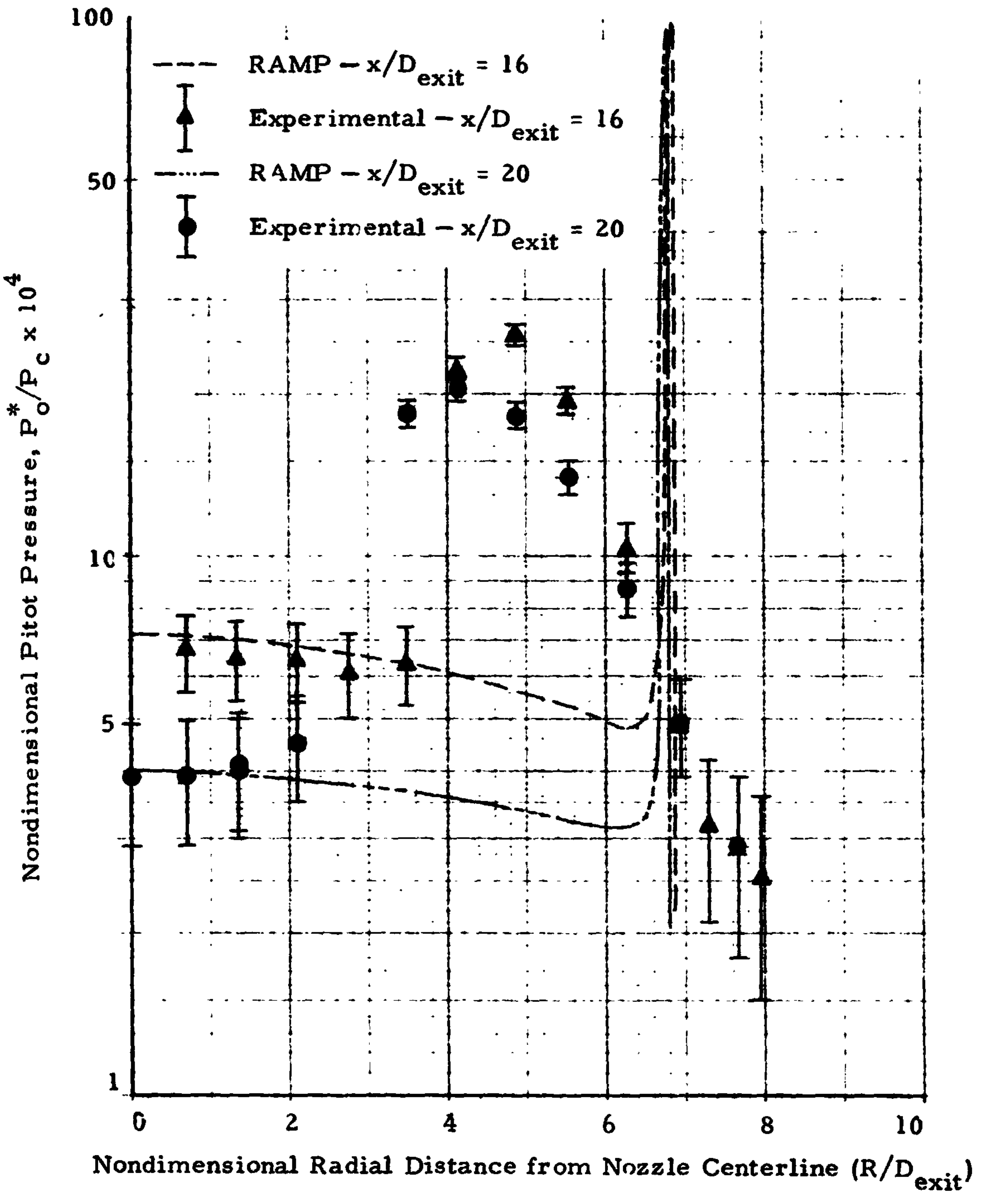

Fig. 31 - Radial Distributions of Nondimensional Pitot Pressure for 2% Al Propellant at an Altitude of 100,000 ft at x/D_{exit} = 16 and 20

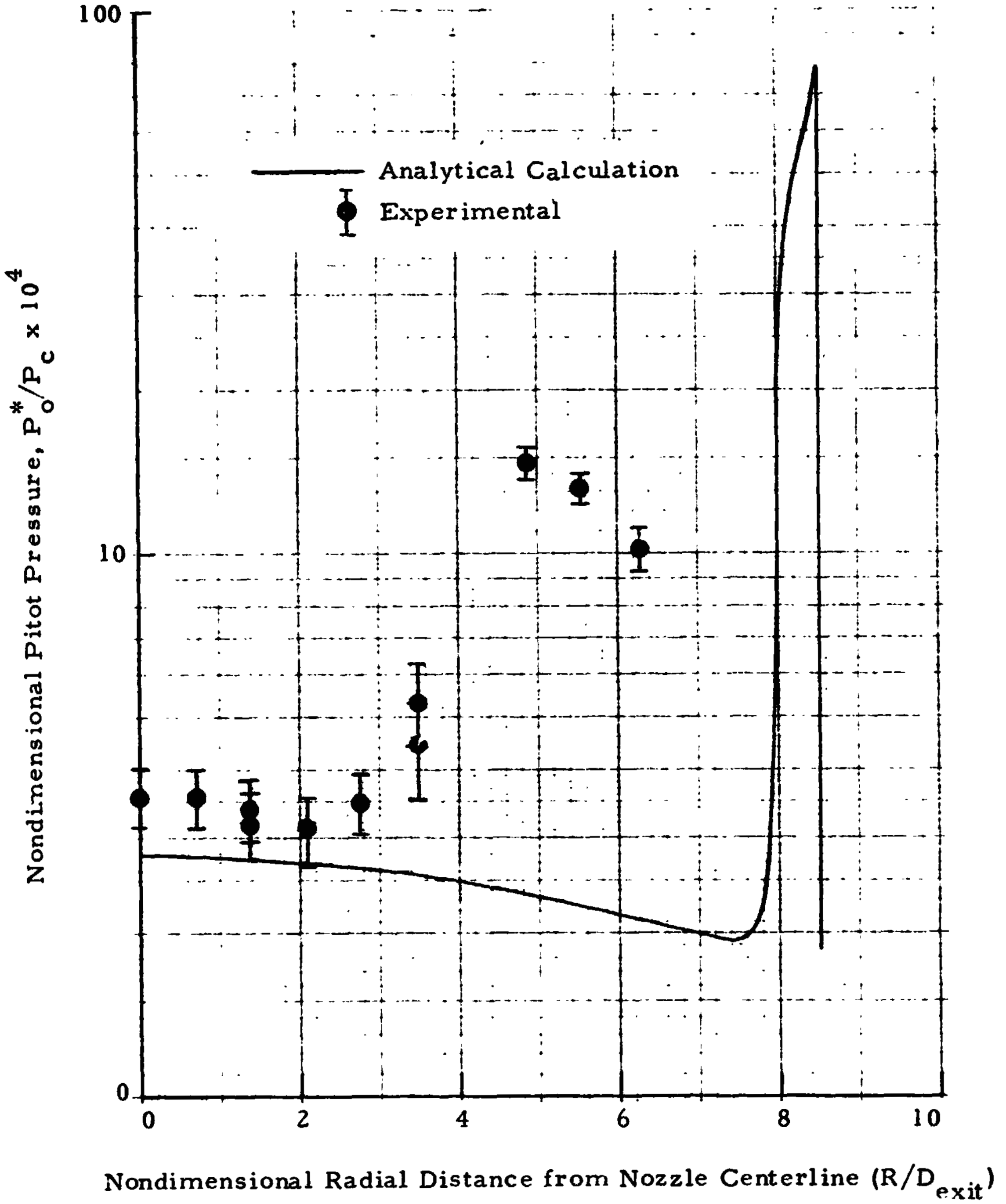

Fig. 32 - Radial Distributions of Nondimensional Pitot Pressure for 10% Aℓ Propellant at x/D_{exit} = 20 and a Simulated Altitude of 100,000 ft

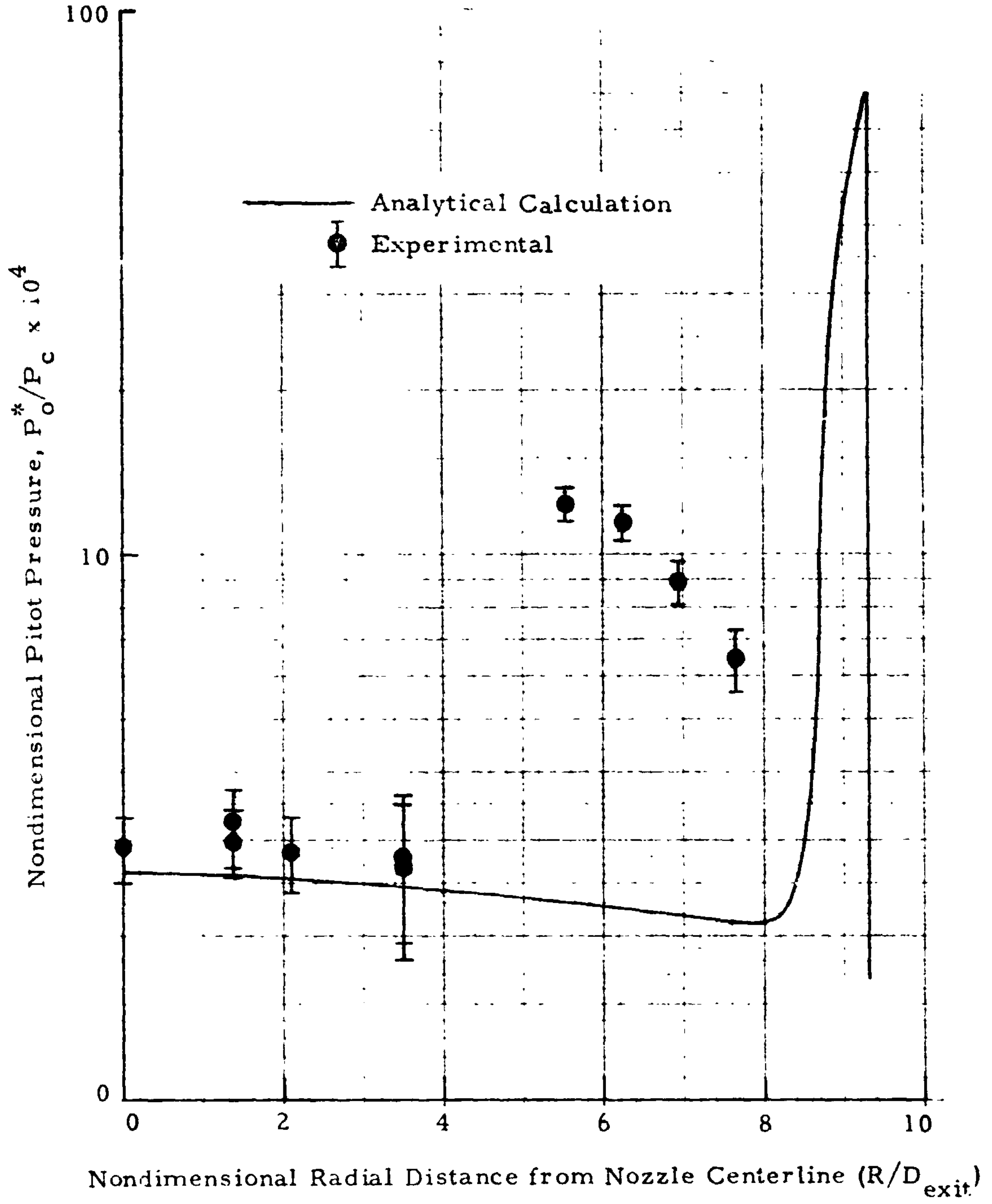

Fig. 33 - Radial Distributions of Nondimensional Pitot Pressure for 15% Al Propellant at x/D_{exit} = 20 and a Simulated Altitude of 100,000 ft

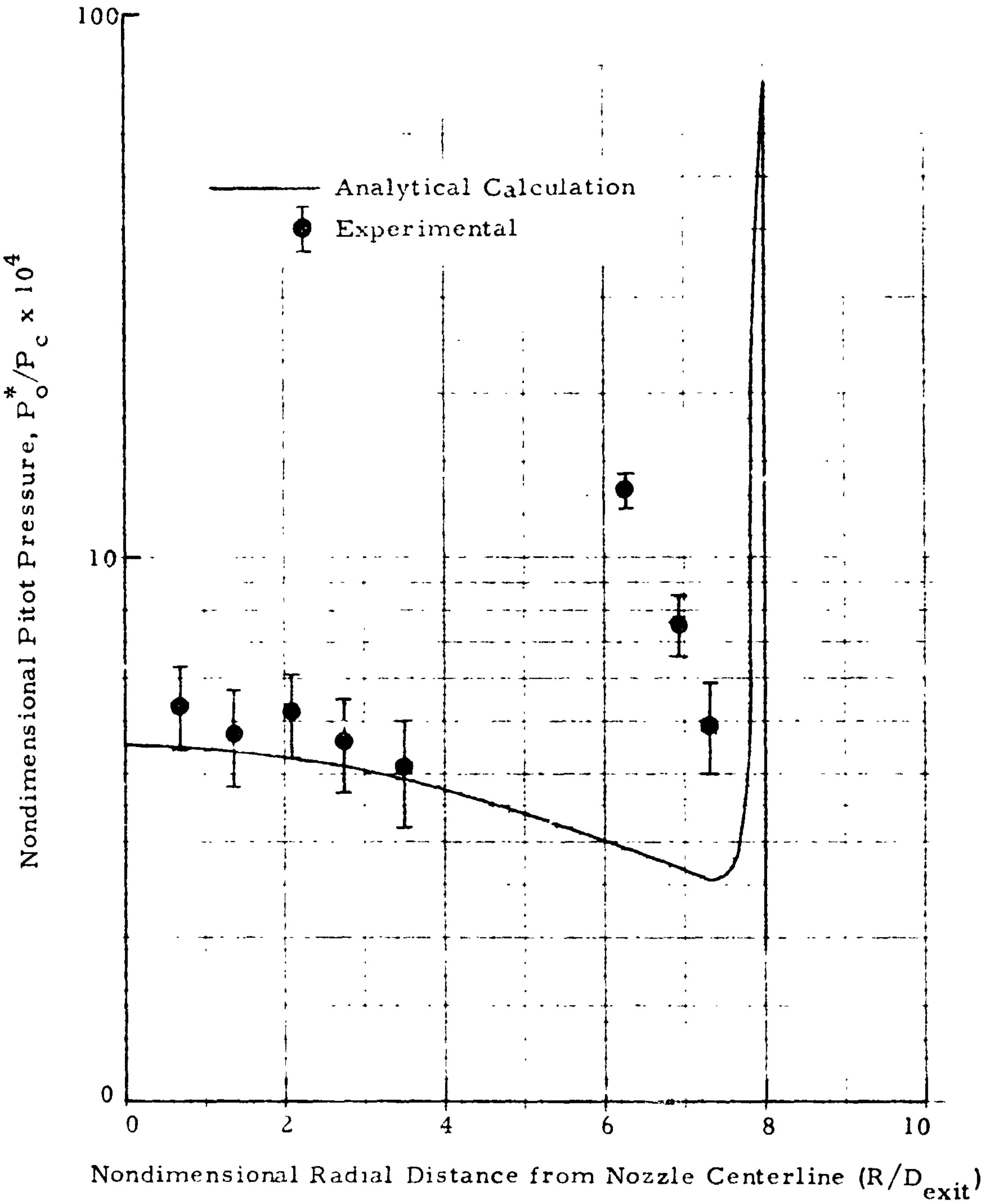

Fig. 34 - Radial Distributions of Nondimensional Pitot Pressure for 10% Al Propellant at $x/D_{exit} = 16$ and a Simulated Altitude of 100,000 ft

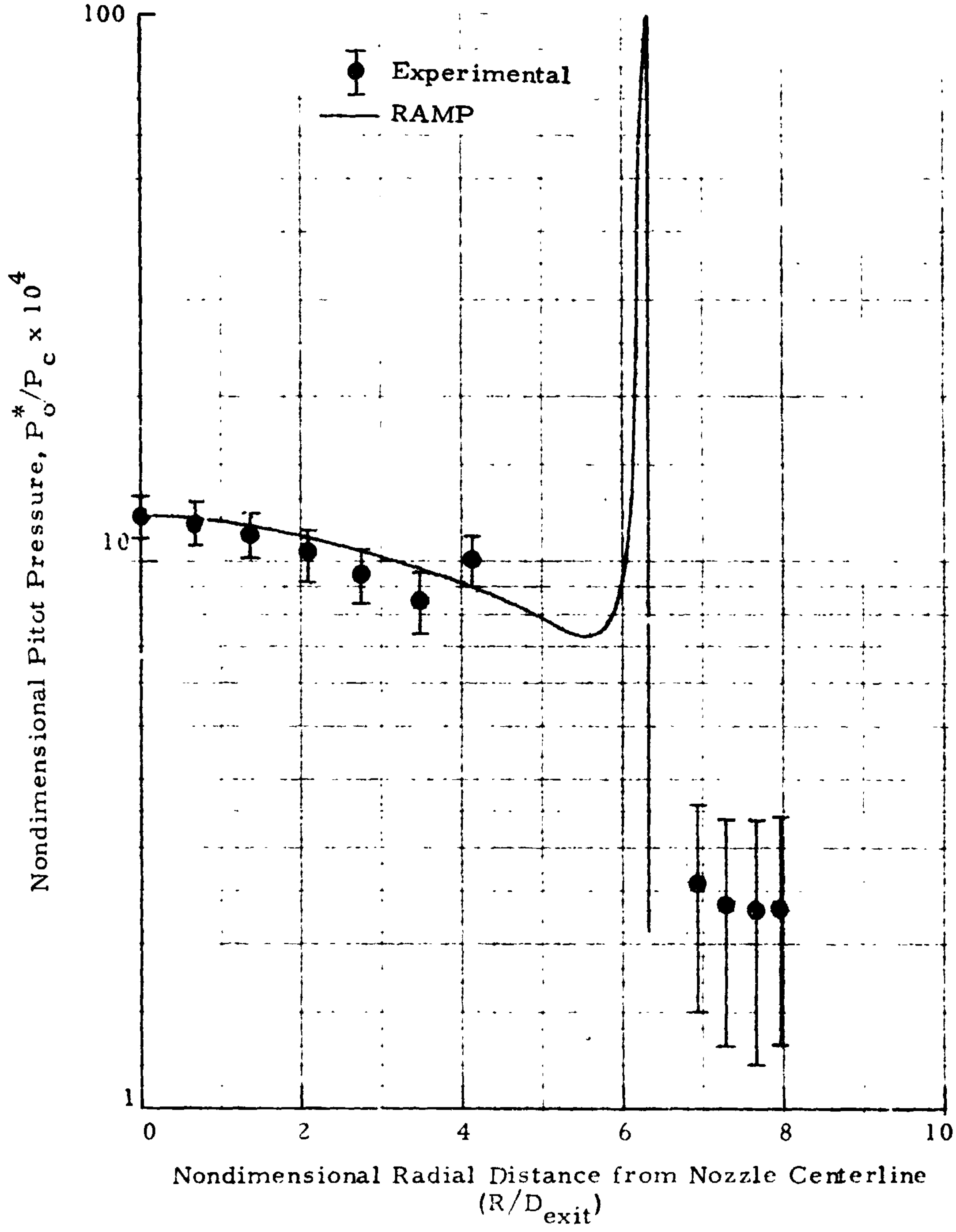

Fig. 35 - Radial Distributions of Nondimensional Pitot Pressure at x/D_{exit} = 12 for 2% Al Propellant and Altitude of 100,000 ft

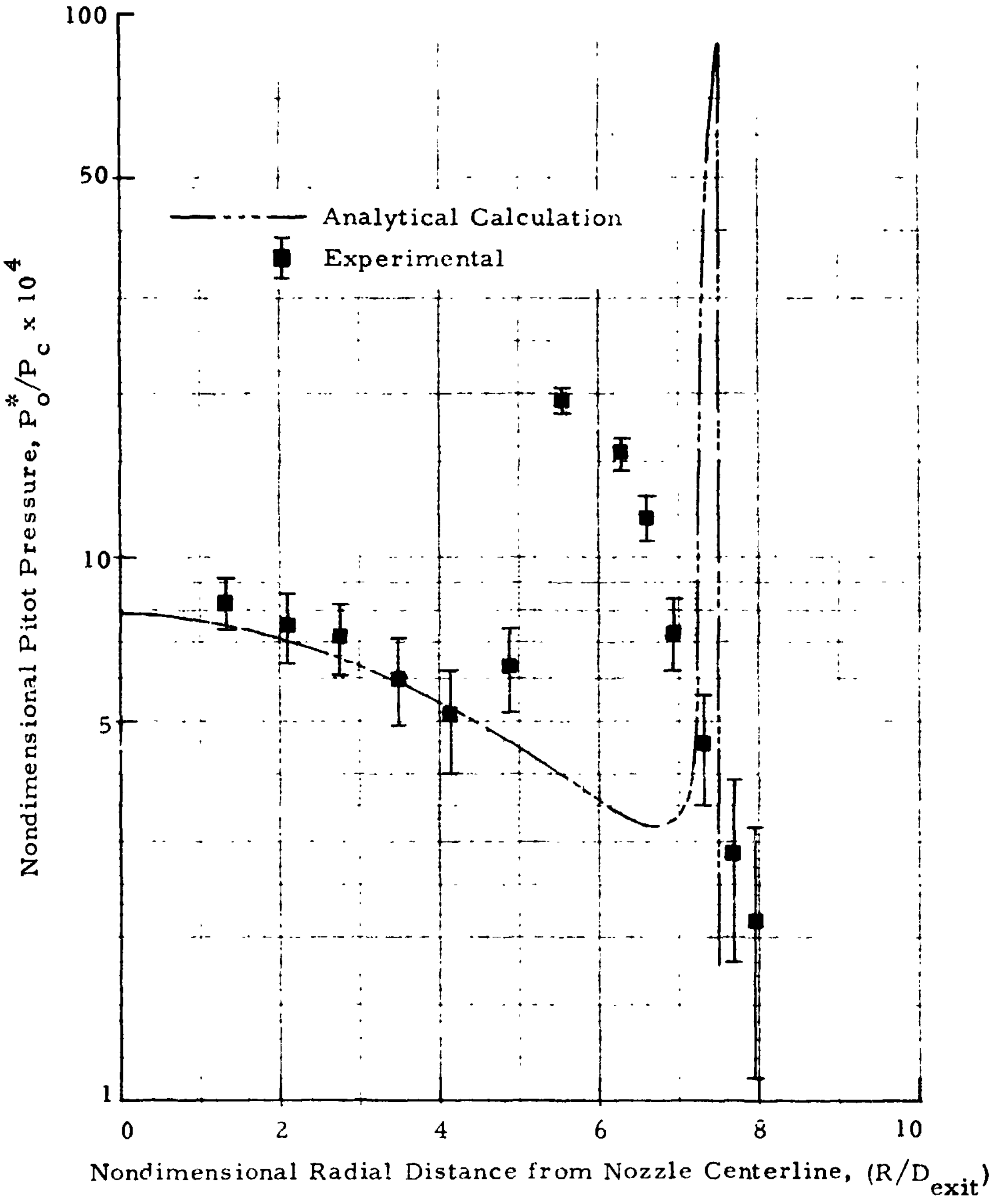

Fig. 36 - Radial Distributions of Nondimensional Pitot Pressure for 10% Al Propellant at $x/D_{exit} = 12$ and an Altitude of 100,000 ft

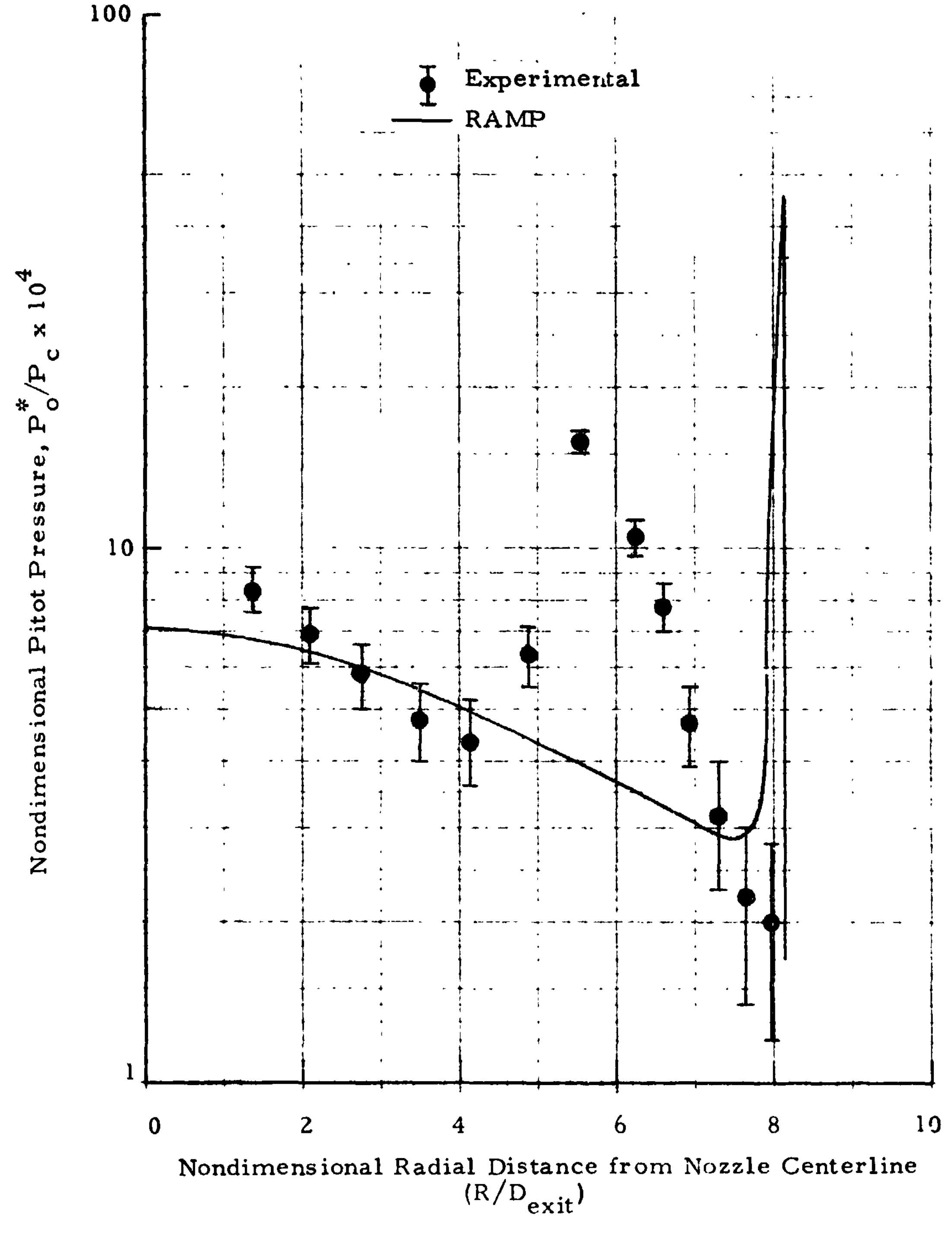

Fig. 37 - Radial Distributions of Nondimensional Pitot Pressure at x/D_{exit} = 12 for 15% Al Propellant and Altitude of 100,000 ft

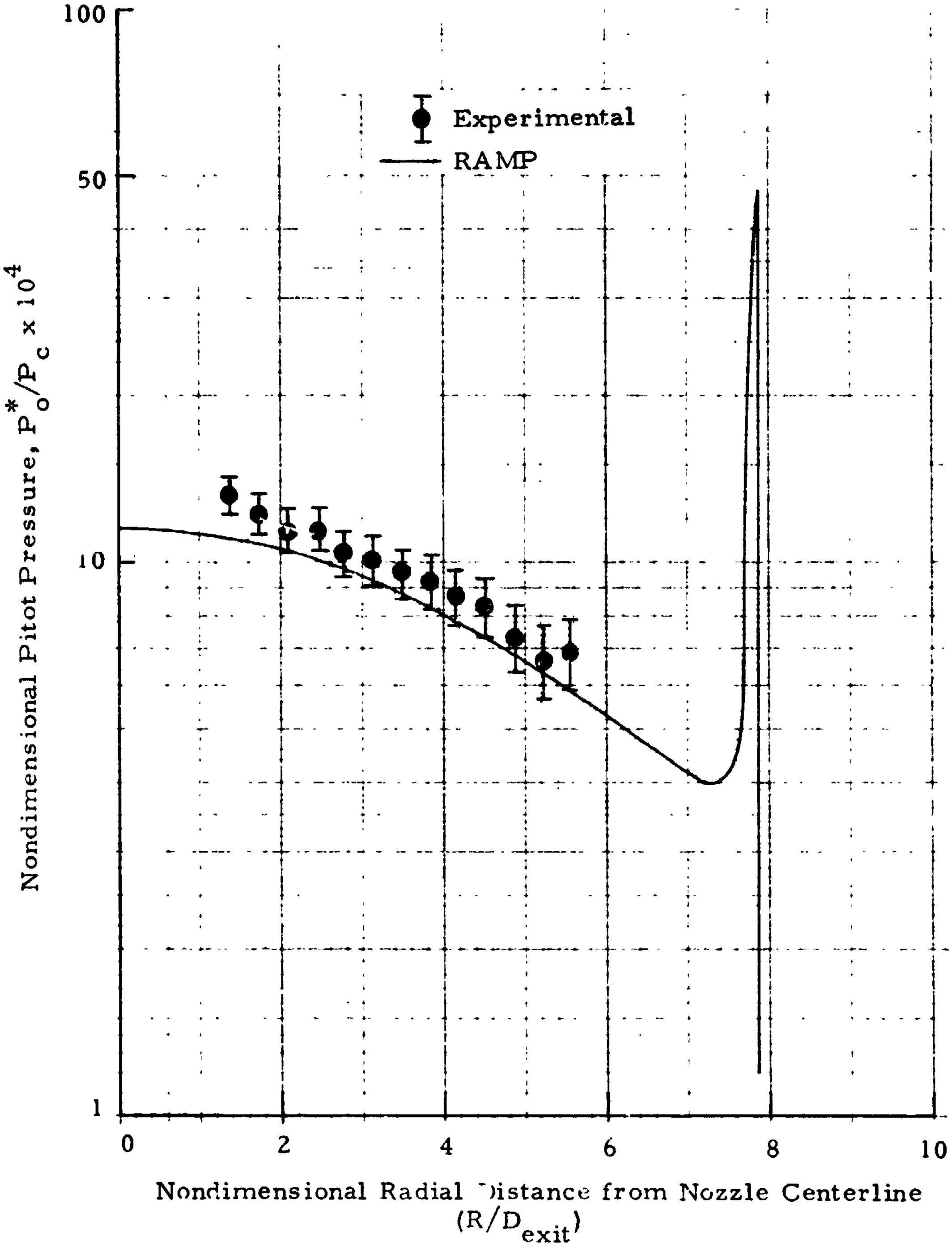

Fig. 38 - Radial Distributions of Nondimensional Pitot Pressure at x/D_{exit} = 12 for 2% Al Propellant and Altitude of 112,000 ft

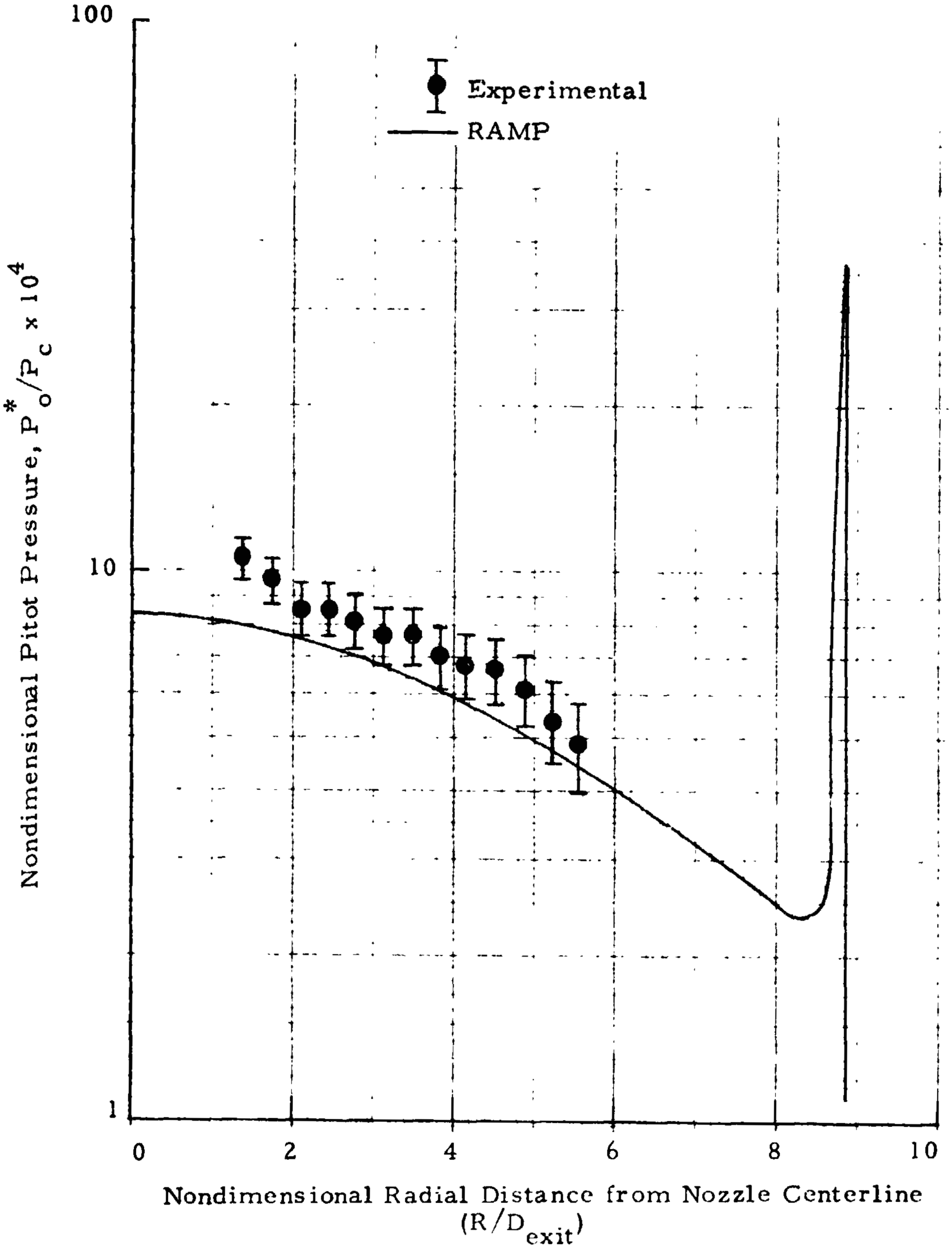

Fig. 39 - Radial Distributions of Nondimensional Pitot Pressure at x/D_{exit} = 12 for 10% Al Propellant and Altitude of 112,000 ft

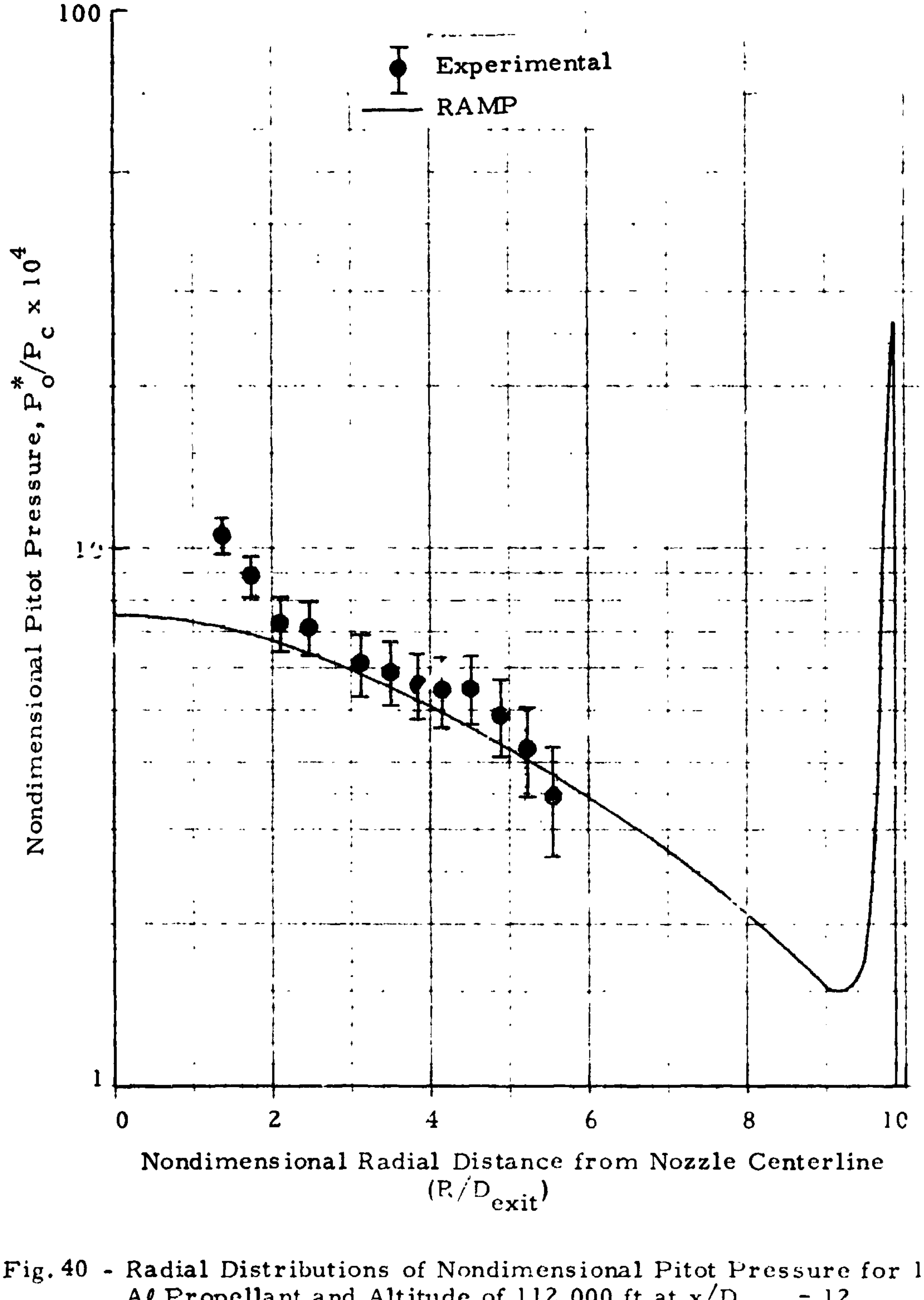

Fig. 40 - Radial Distributions of Nondimensional Pitot Pressure for 15% Al Propellant and Altitude of 112,000 ft at $x/D_{exit} = 12$

REPRODUCIBILITY OF THE
ORIGINAL PAGE IS POOR

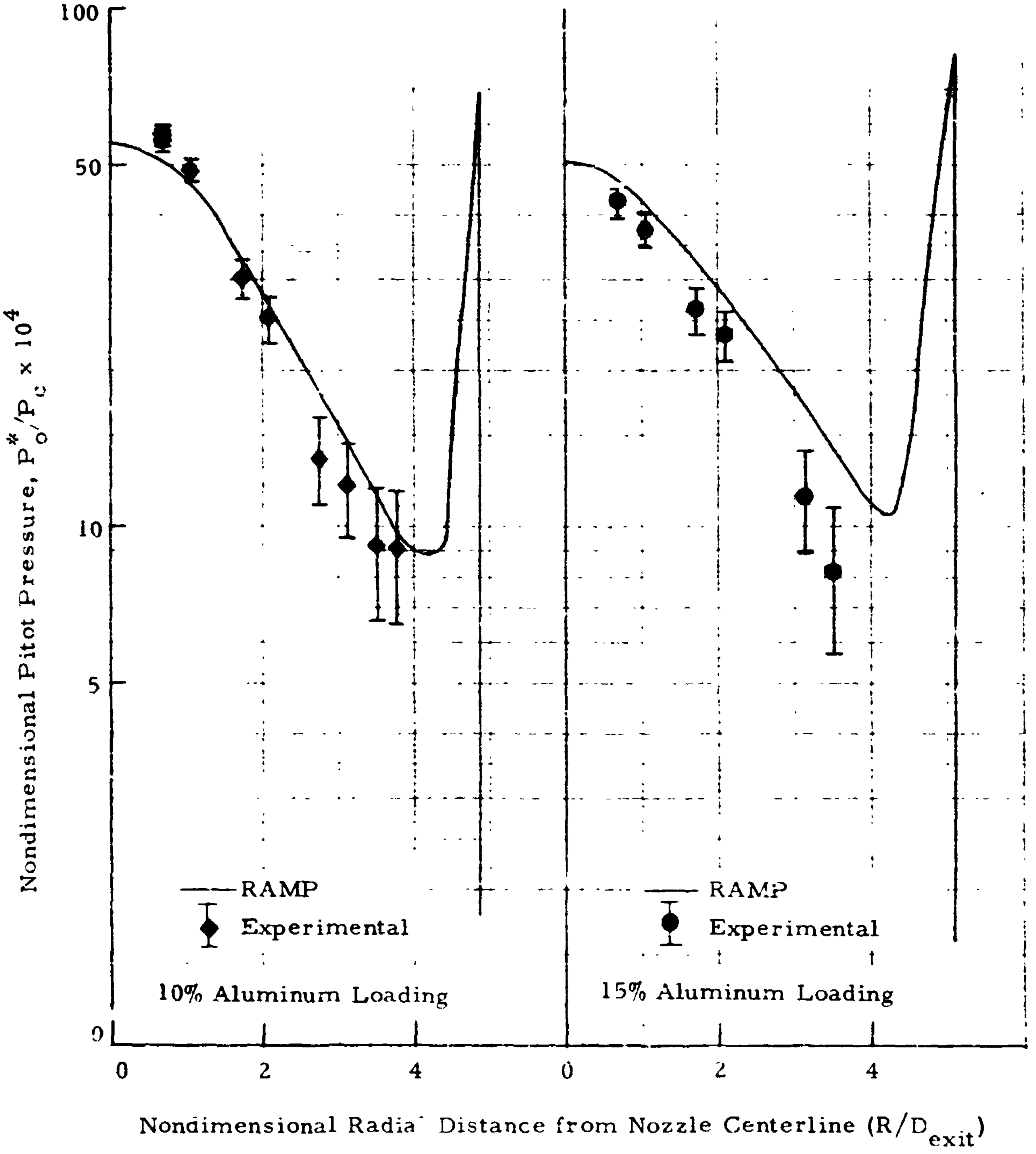

Fig. 41 - Radial Distributions of Nondimensional Pitot Pressure at x/D_{exit} = 5, an Altitude of 100,000 ft and 10 and 15% Al Propellants

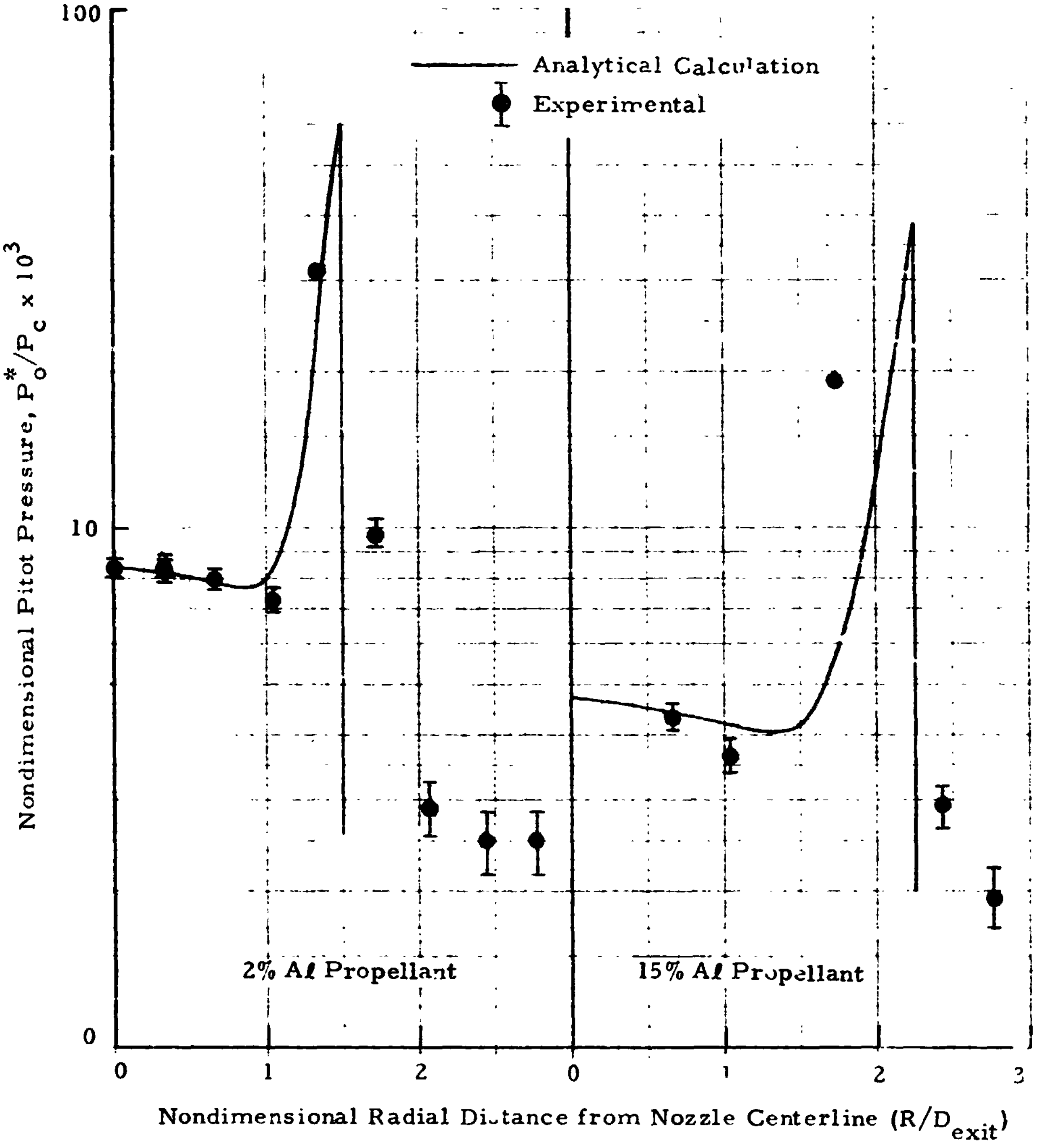

Fig. 42 - Radial Distributions of Nondimensional Pitot Pressure at x/D_{exit} = 5 for 2 and 15% Al Propellants and a Simulated Altitude of 50,000 ft

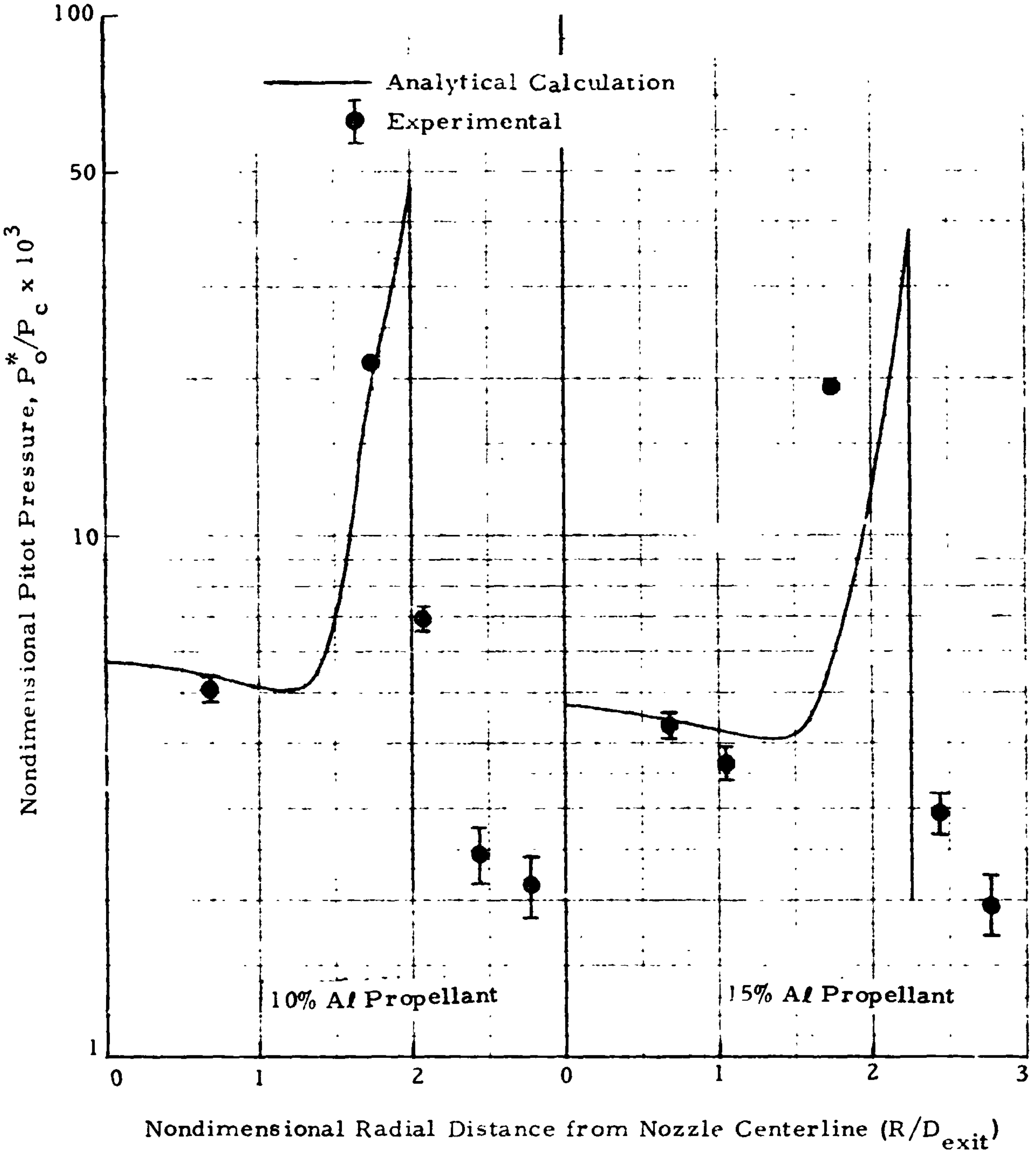

Fig.43 - Radial Distributions of Nondimensional Pitot Pressure at $x/D_{exit} = 5$ for 10 and 15% Al Propellants and Altitude of 50,000 ft

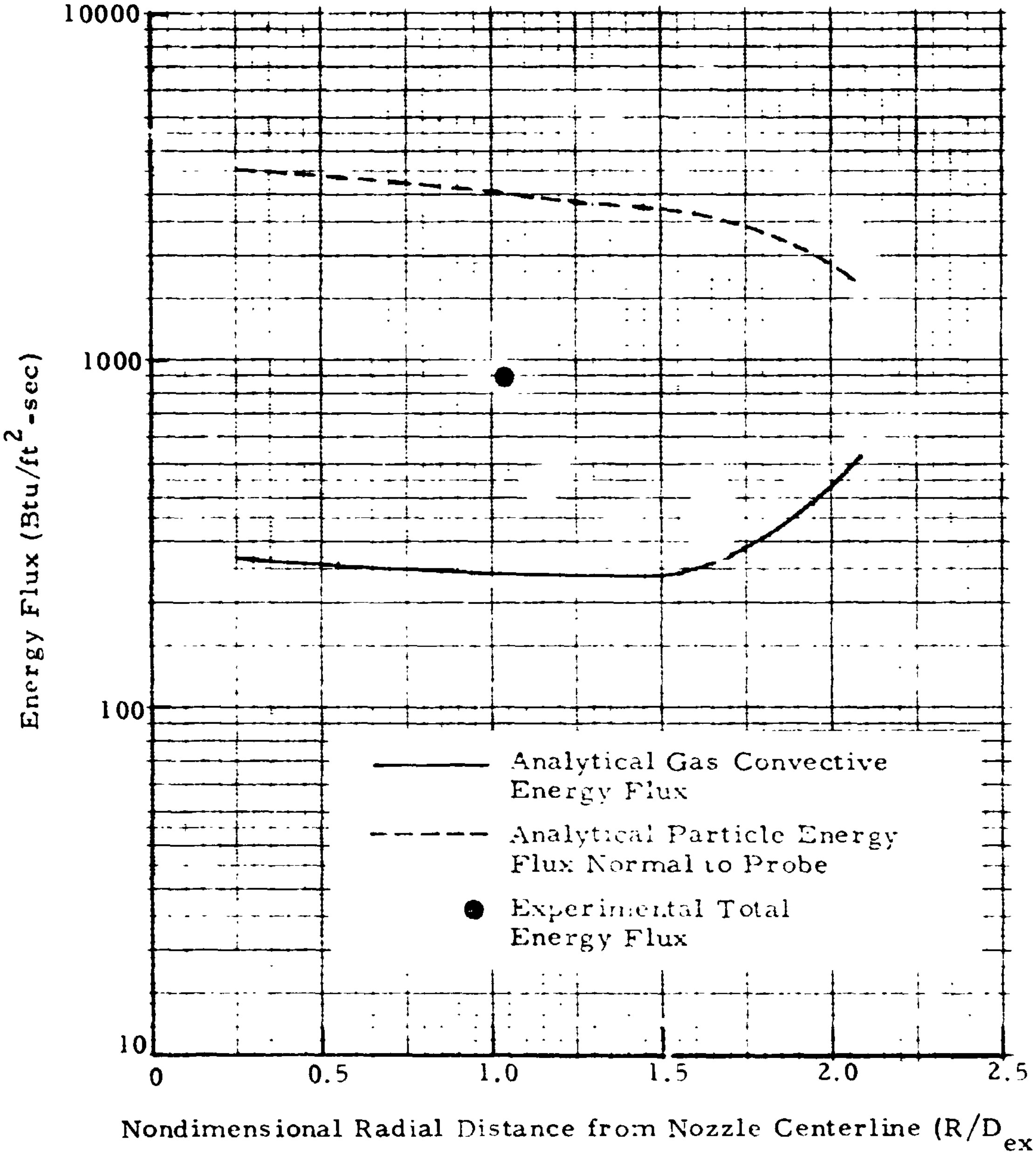

Fig.44 - Comparison of Experimental and Analytical Energy Flux for the 15% Al Propellant at $x/D_{exit} = 5$ and a Simulated Altitude of 50,000 ft

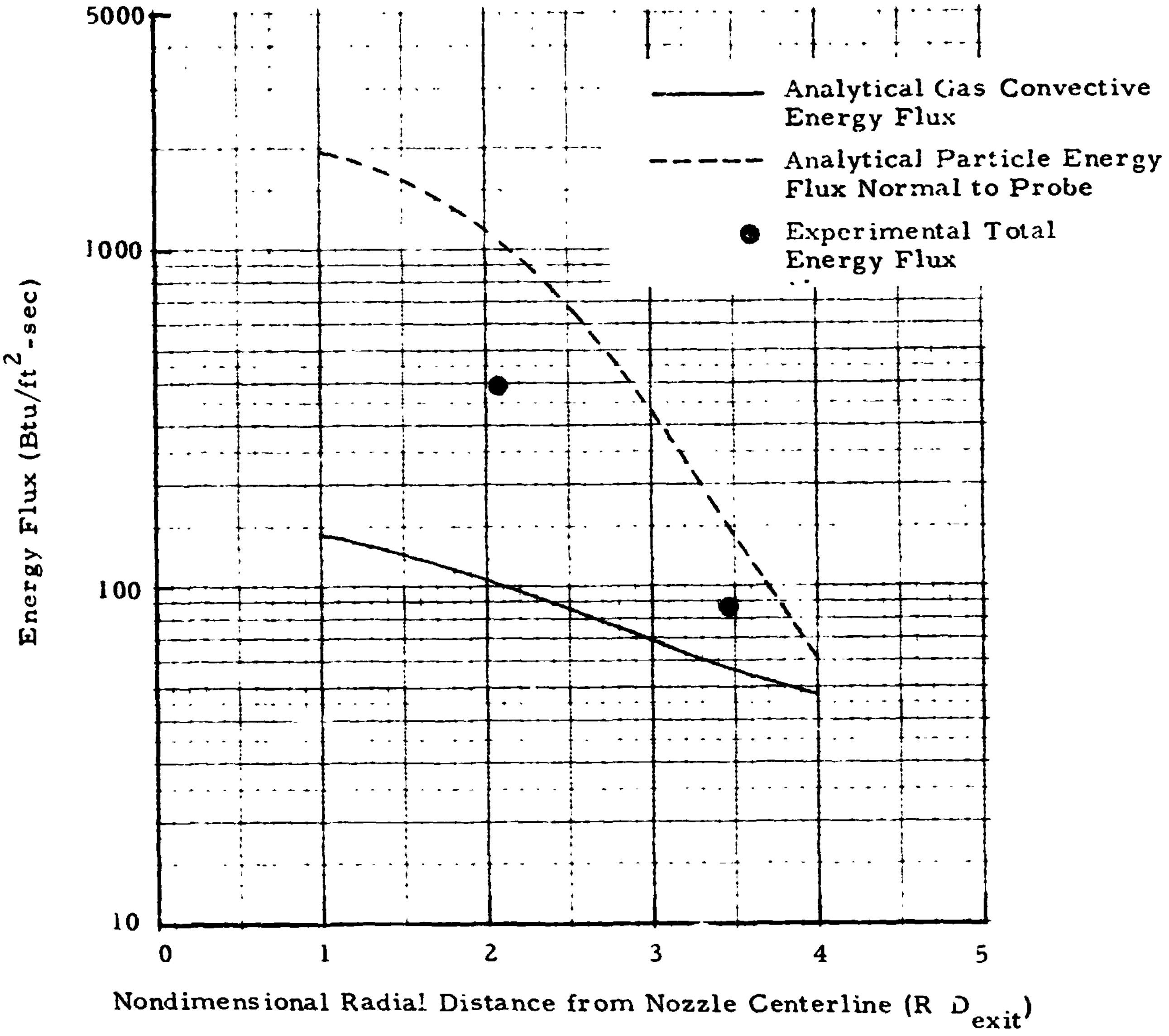

Fig. 45 - Comparison of Experimental and Analytical Energy Flux for the 10% Aℓ Propellant at $x/D_{exit} = 5$ and a Simulated Altitude of 100,000 ft

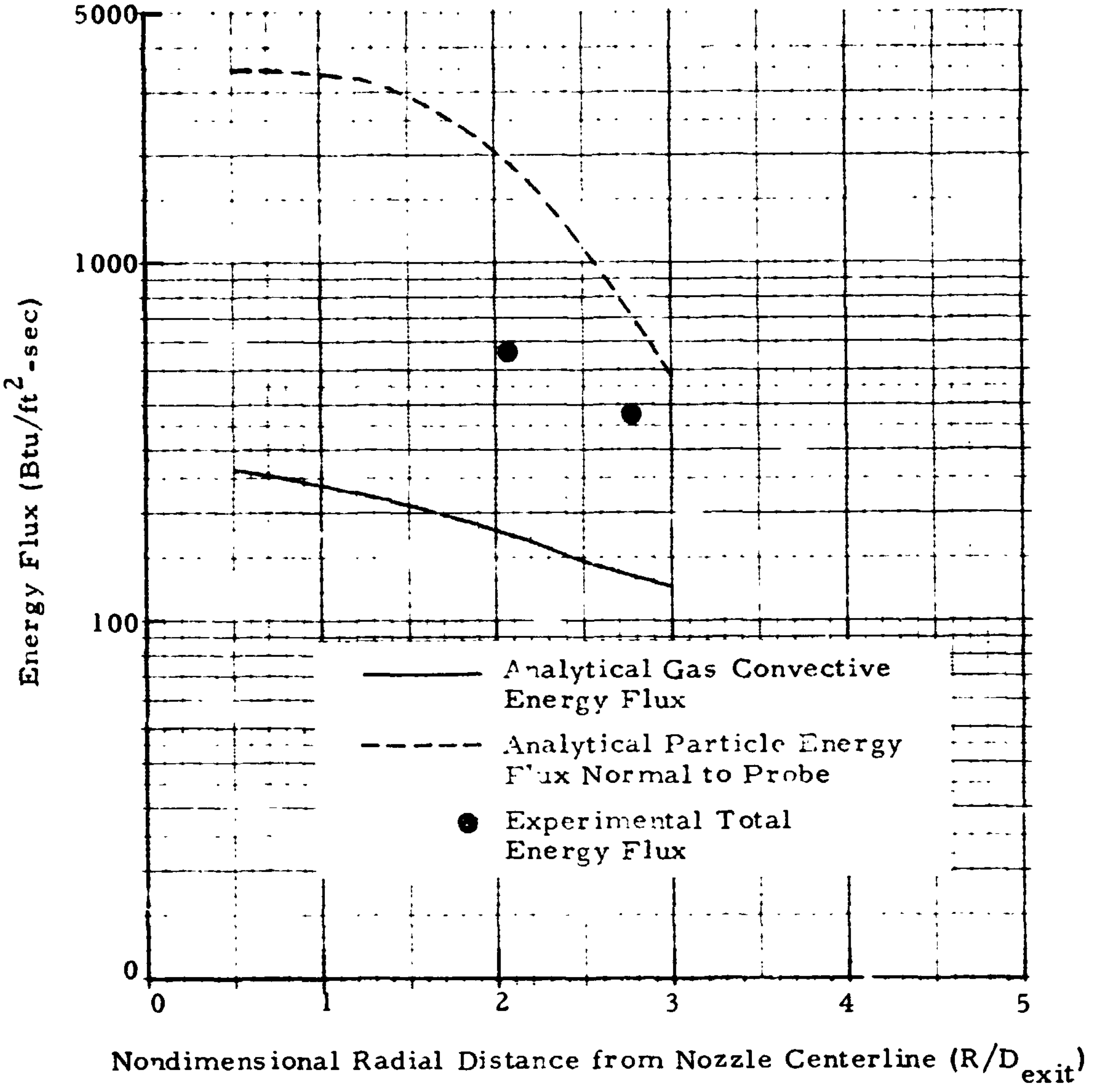

Fig. 46 - Comparison of Experimental and Analytical Energy Flux for the 15% Al Propellant at $x/D_{exit} = 5$ and a Simulated Altitude of 100,000 ft

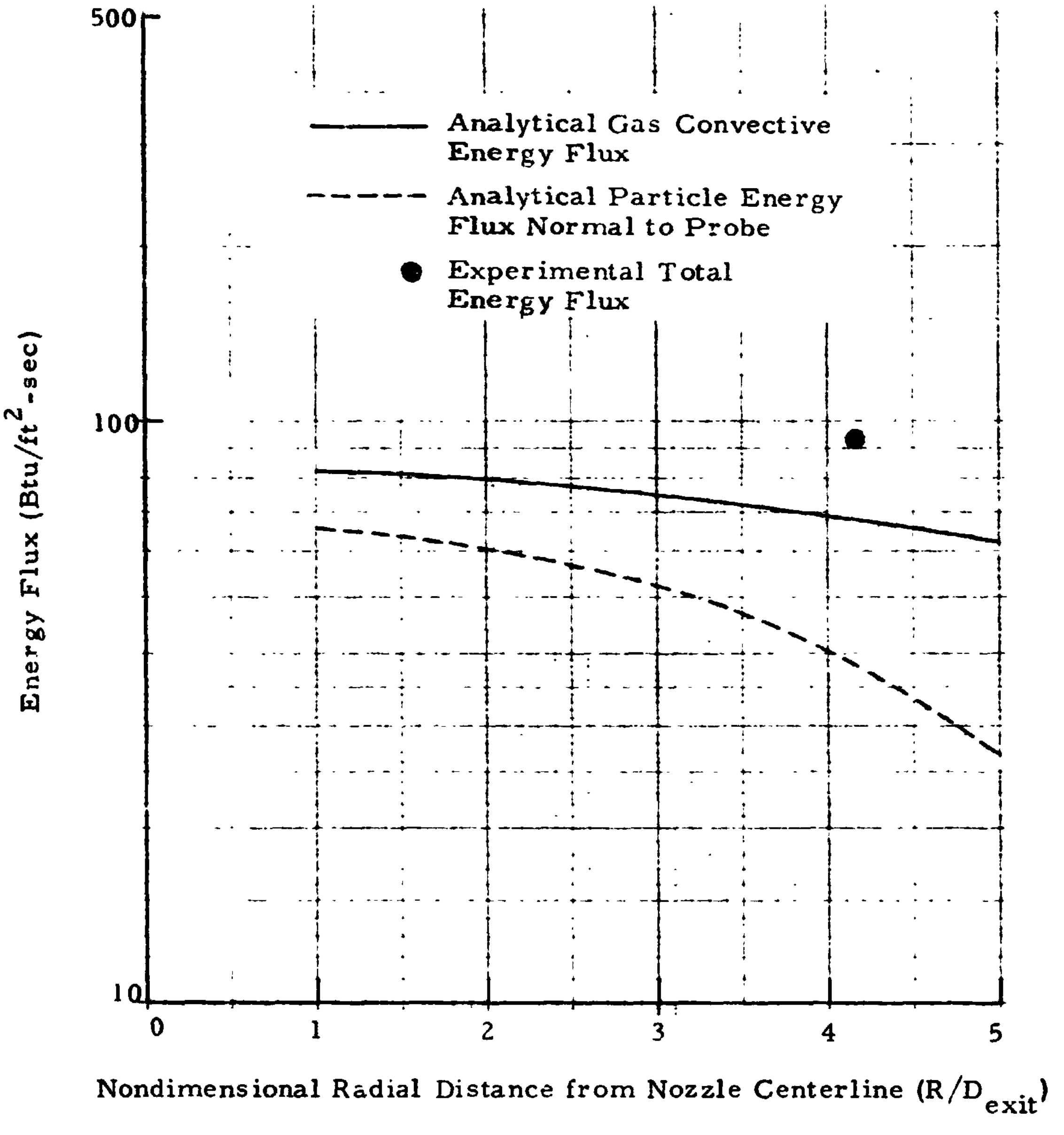

Fig. 47 - Comparison of Experimental and Analytical Energy Flux for the 2% Al Propellant at $x/D_{exit} = 12$ and a Simulated Altitude of 100,000 ft

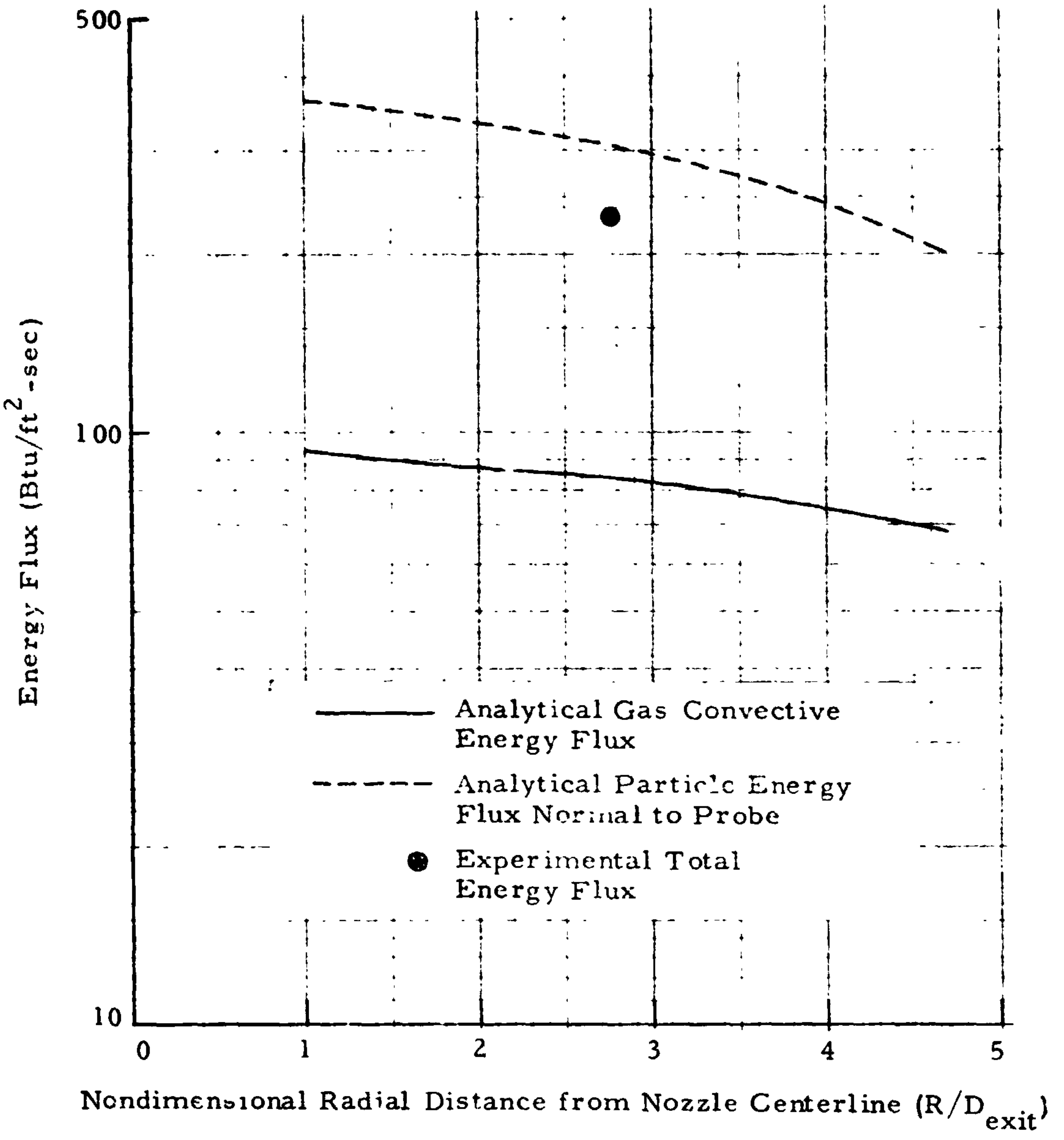

Fig. 48 - Comparison of Experimental and Analytical Energy Flux for the 10% Al Propellant at $x/D_{exit} = 12$ and a Simulated Altitude of 100,000 ft

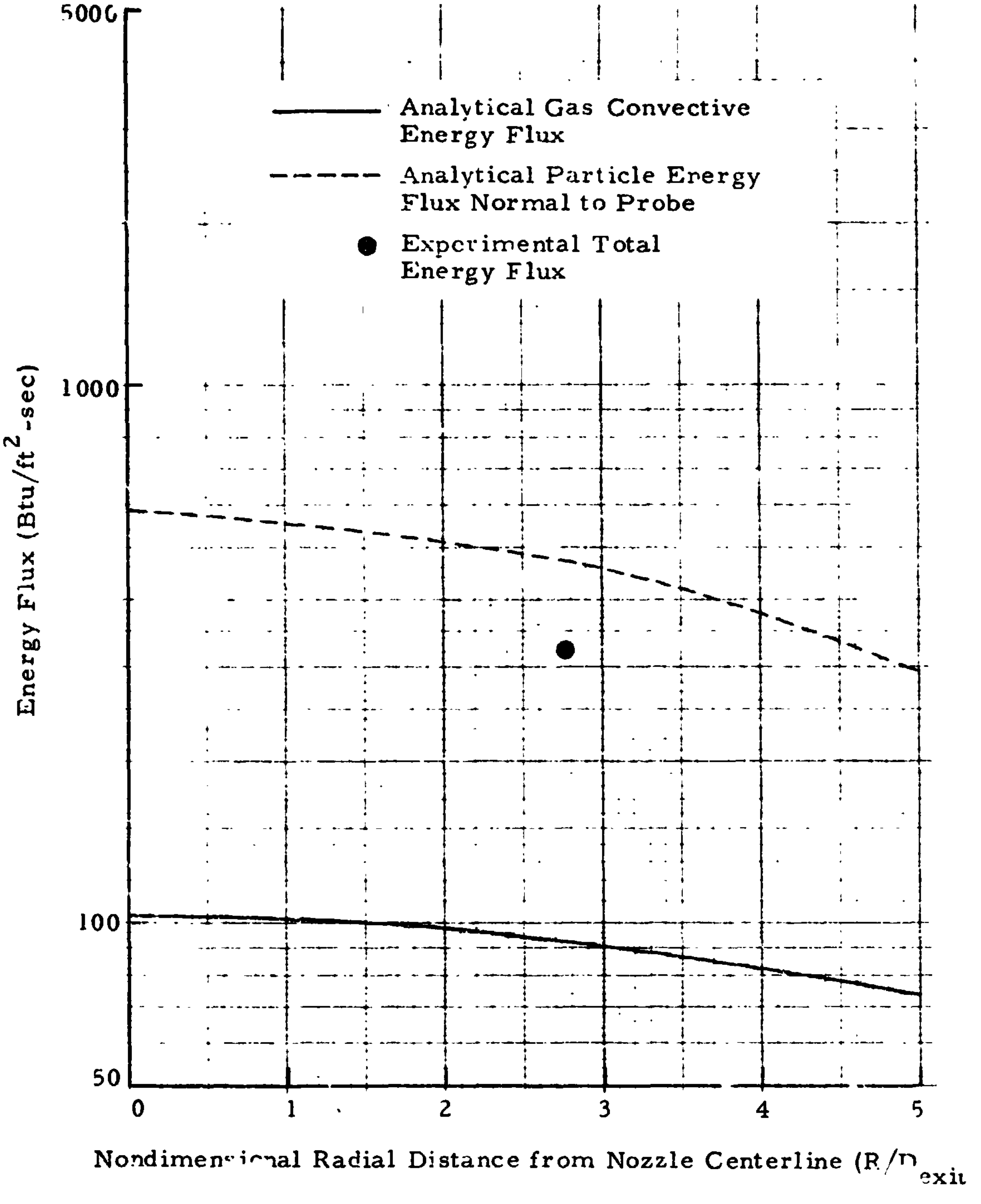

Fig. 49 - Comparison of Experimental and Analytical Energy Flux for the 15% Al Propellant at $x/D_{exit} = 12$ and a Simulated Altitude of 100,000 ft

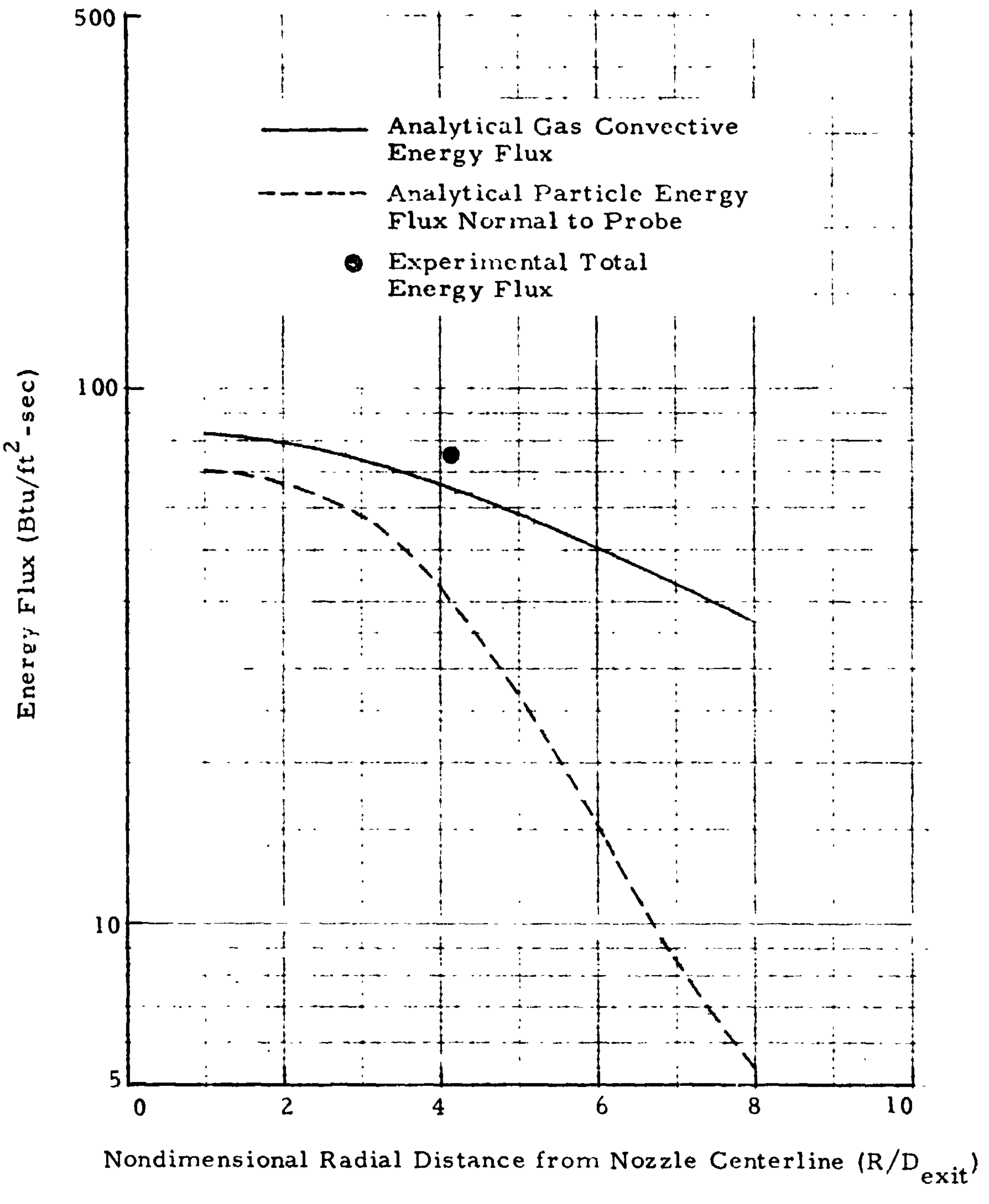

Fig. 50 - Comparison of Experimental and Analytical Energy Flux for the 2% Al Propellant at $x/D_{exit} = 12$ and a Simulated Altitude of 112,000 ft

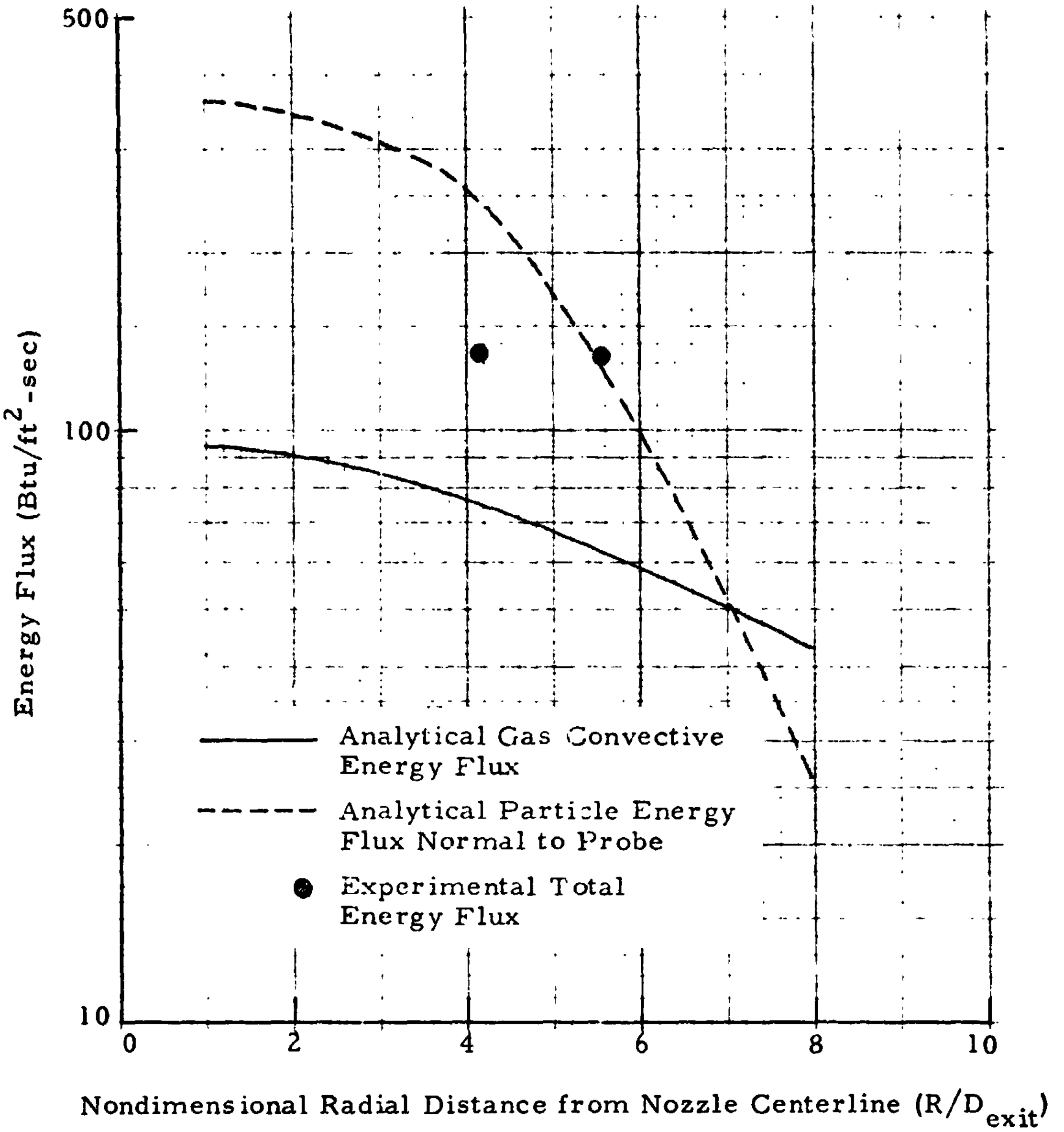

Fig. 51 - Comparison of Experimental and Analytical Energy Flux for the 10% Al Propellant at x/D_{exit} = 12 and a Simulated Altitude of 112,000 ft

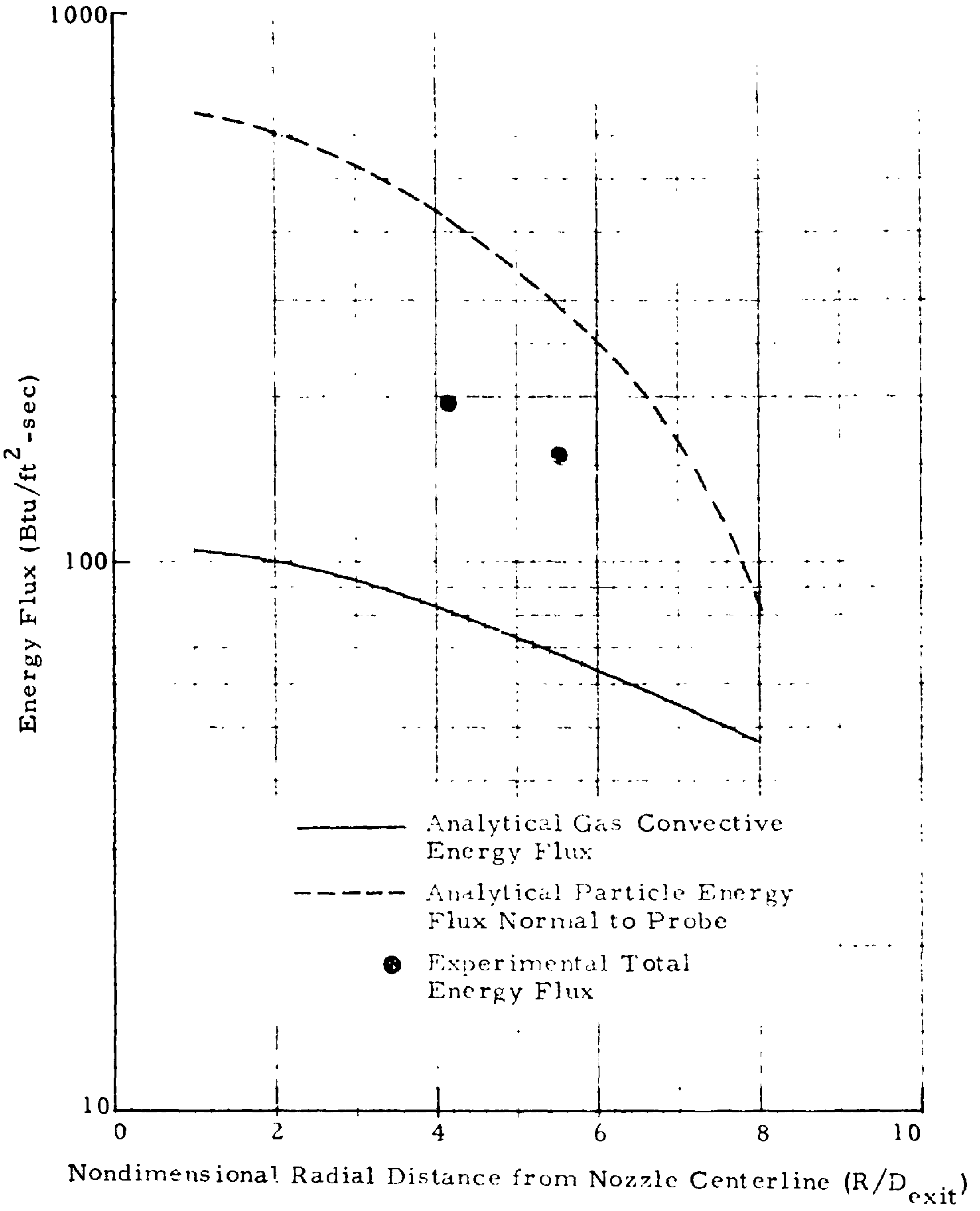

Fig. 52 - Comparison of Experimental and Analytical Energy Flux for the 15% Al Propellant at x/D$_{exit}$ = 12 and a Simulated Altitude of 112,000 ft

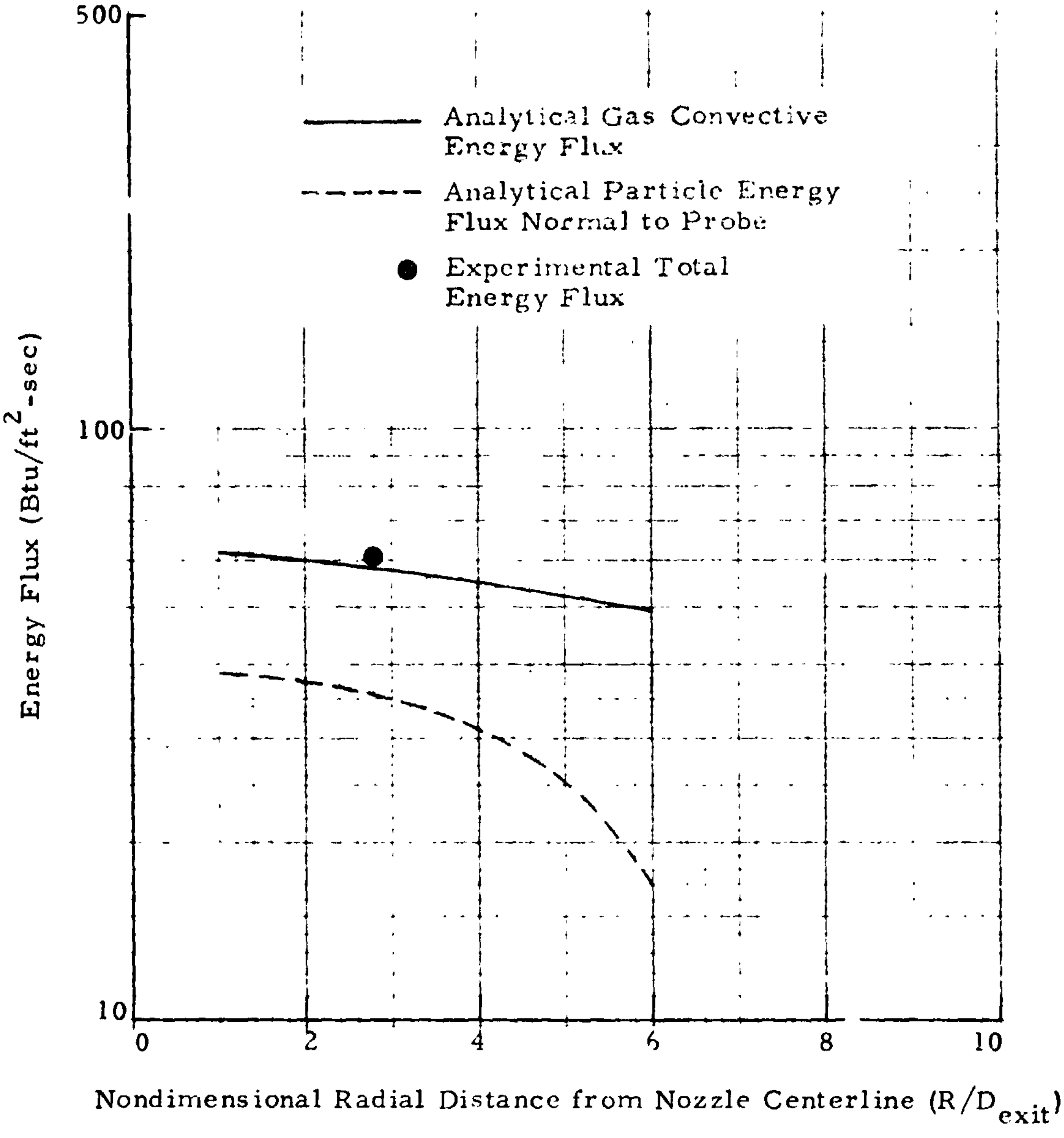

Fig. 53 - Comparison of Experimental and Analytical Energy Flux for the 2% Al Propellant at x/D$_{exit}$ = 16 and a Simulated Altitude of 100,000 ft

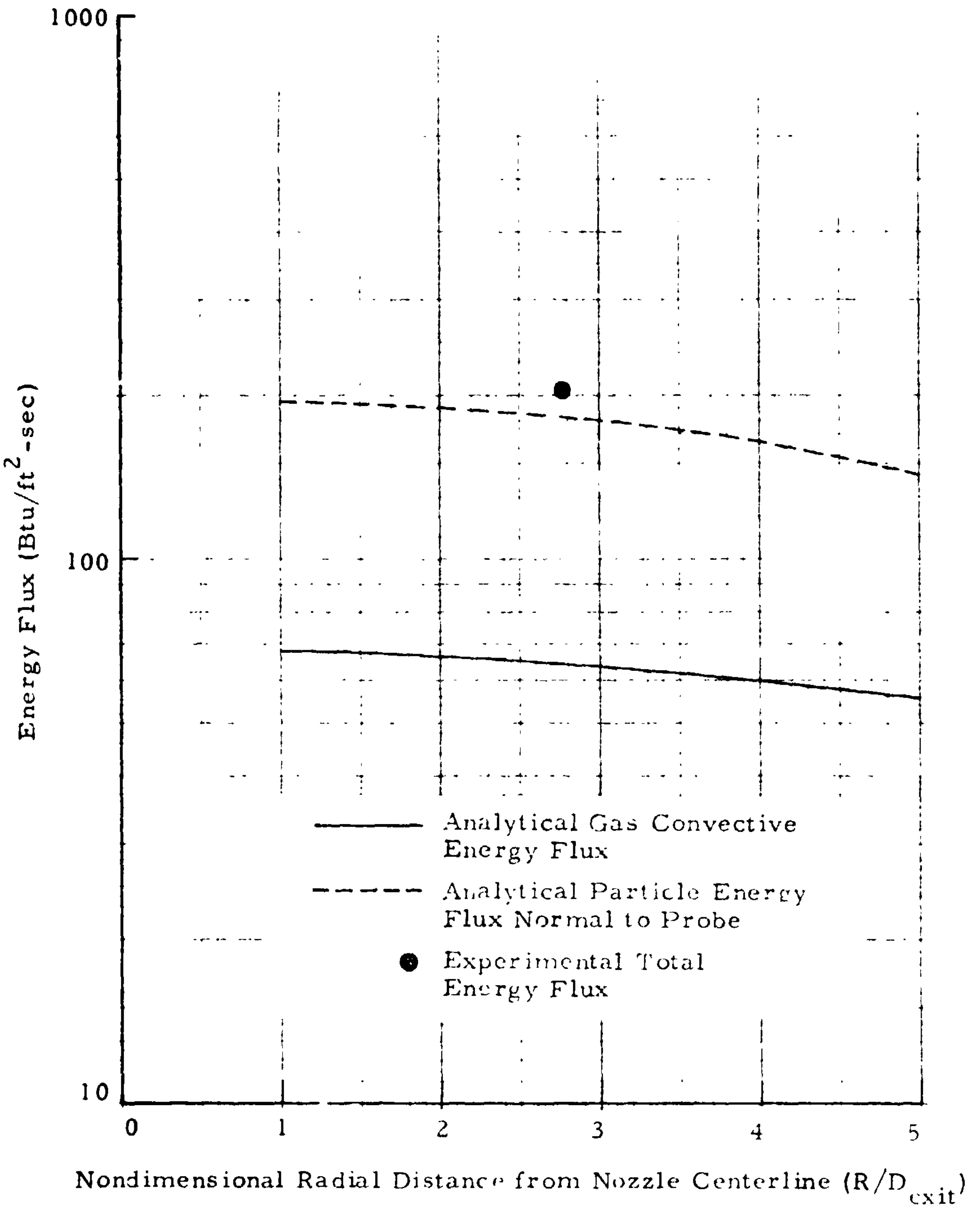

Fig. 54 - Comparison of Experimental and Analytical Energy Flux for the 10% Al Propellant at x/D$_{exit}$ = 16 and a Simulated Altitude of 100,000 ft

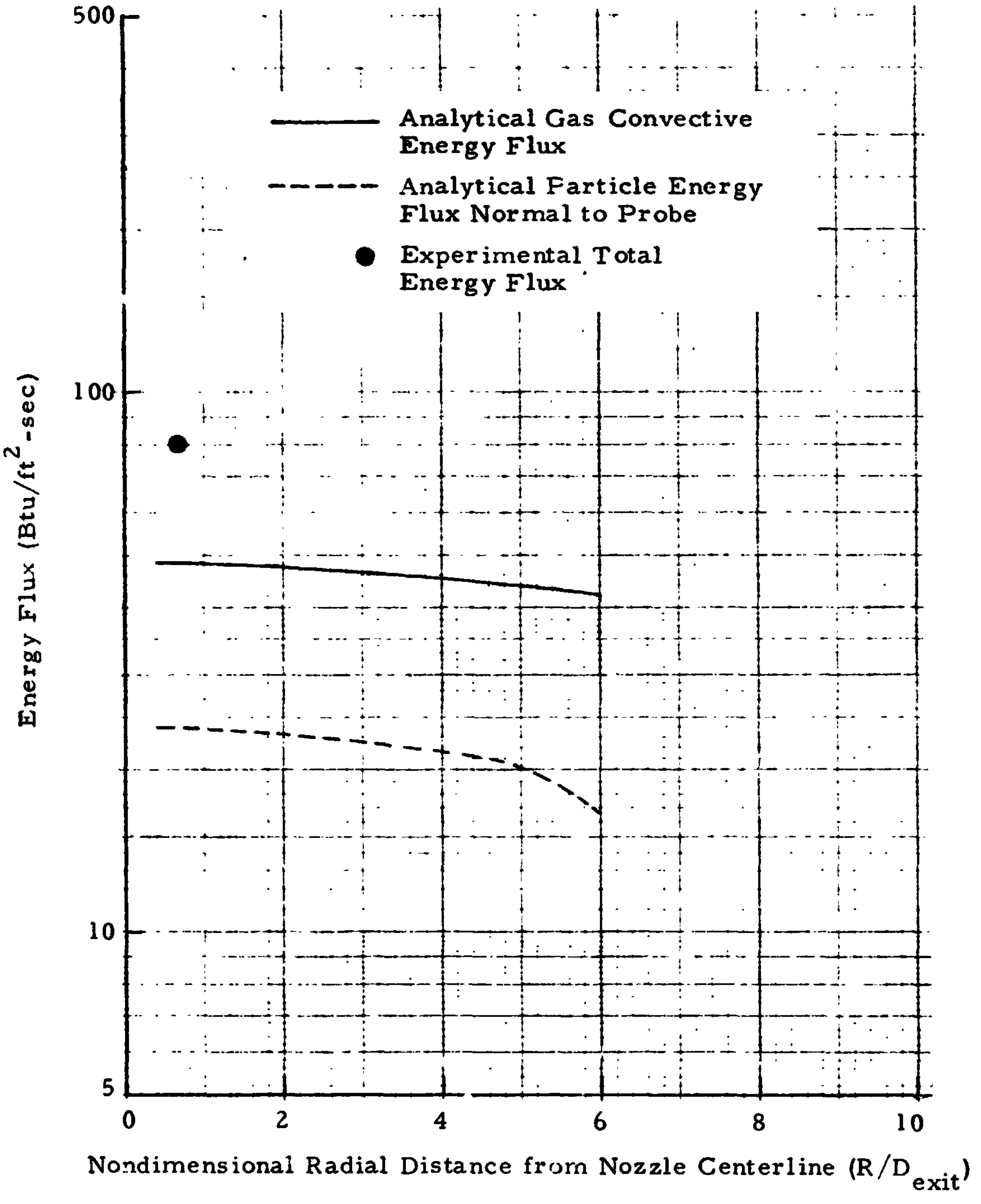

Fig. 55 - Comparison of Experimental and Analytical Energy Flux for the 2% Al Propellant at $x/D_{exit} = 20$ and a Simulated Altitude of 100,000 ft

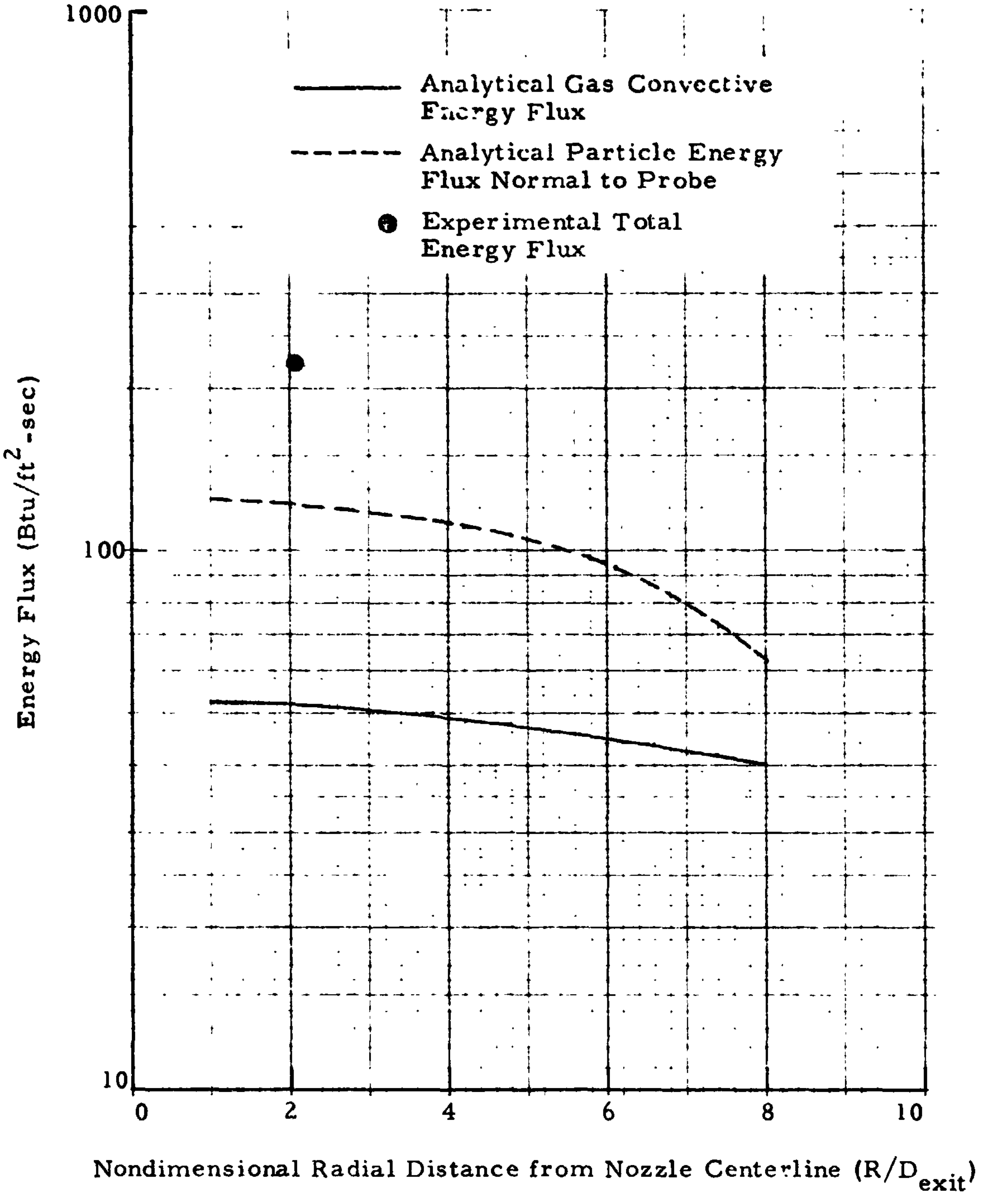

Fig. 56 - Comparison of Experimental and Analytical Energy Flux for the 10% Al Propellant at x/D_{exit} = 20 and a Simulated Altitude of 100,000 ft

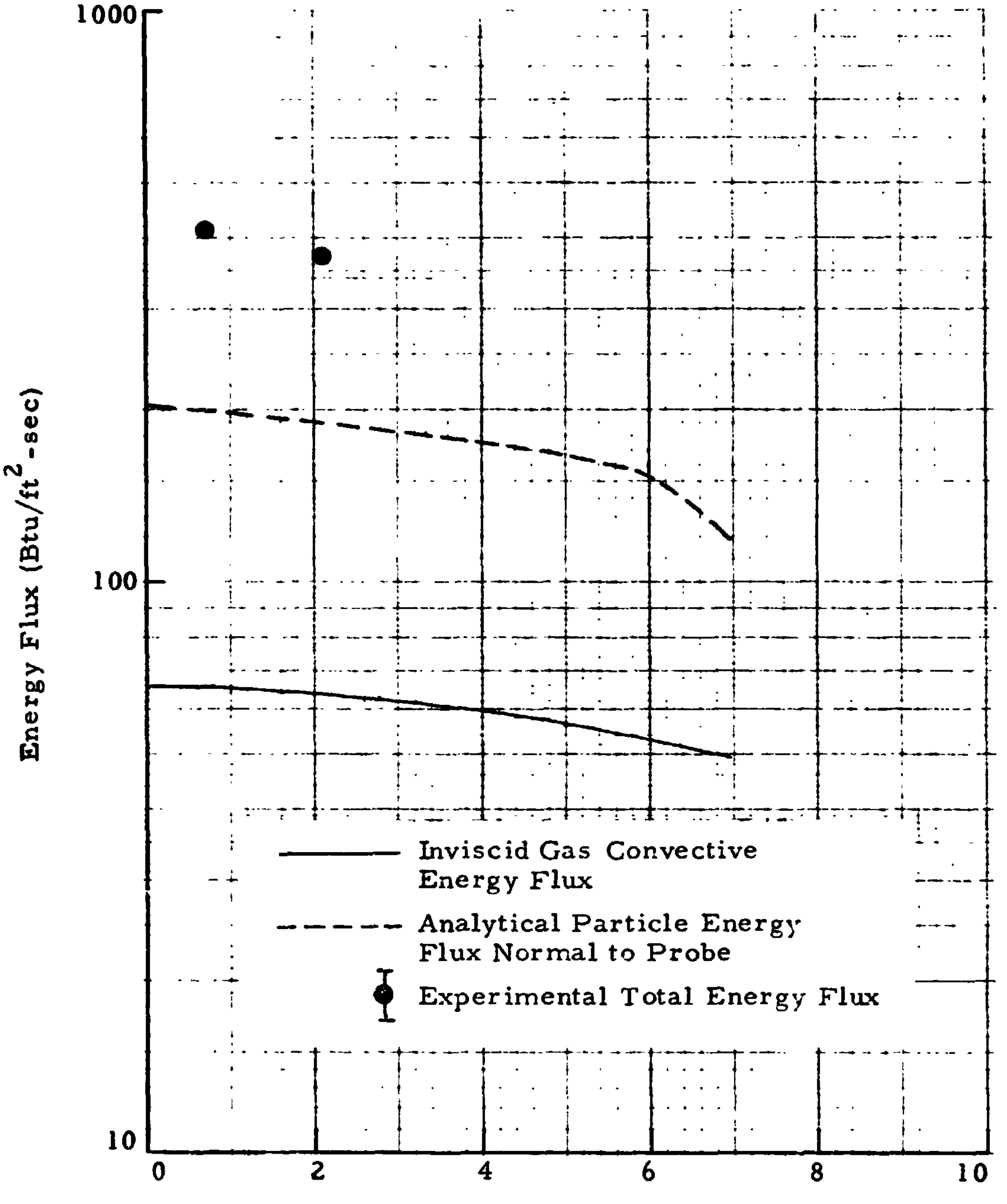

Fig. 57 - Comparison of Experimental and Analytical Energy Flux for the 15% Aℓ Propellant at x/D$_{exit}$ = 20 and a Simulated Altitude of 100,000

REPRODUCIBILITY OF THE
ORIGINAL PAGE IS POOR

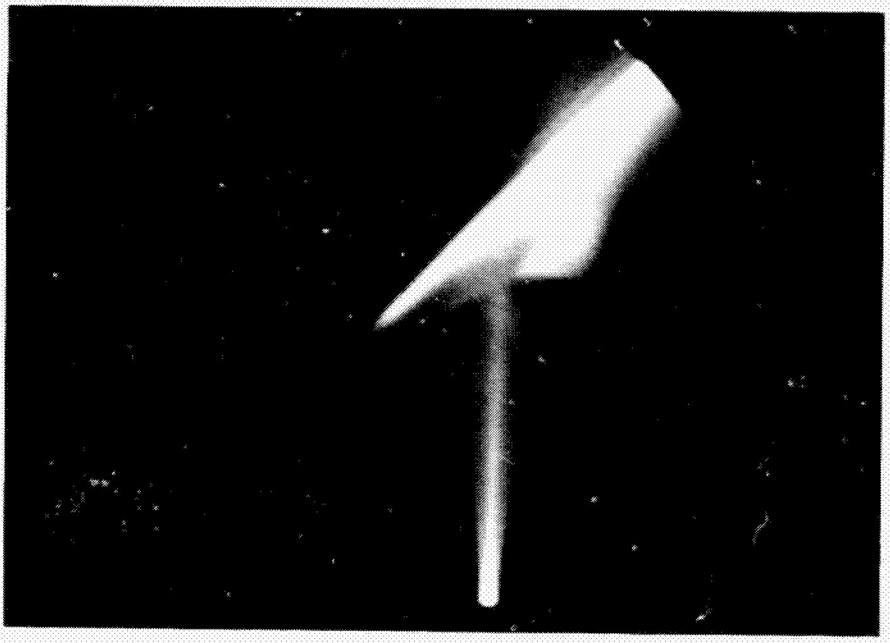

10% Aℓ Propellant, $\psi = 45^{\circ}$

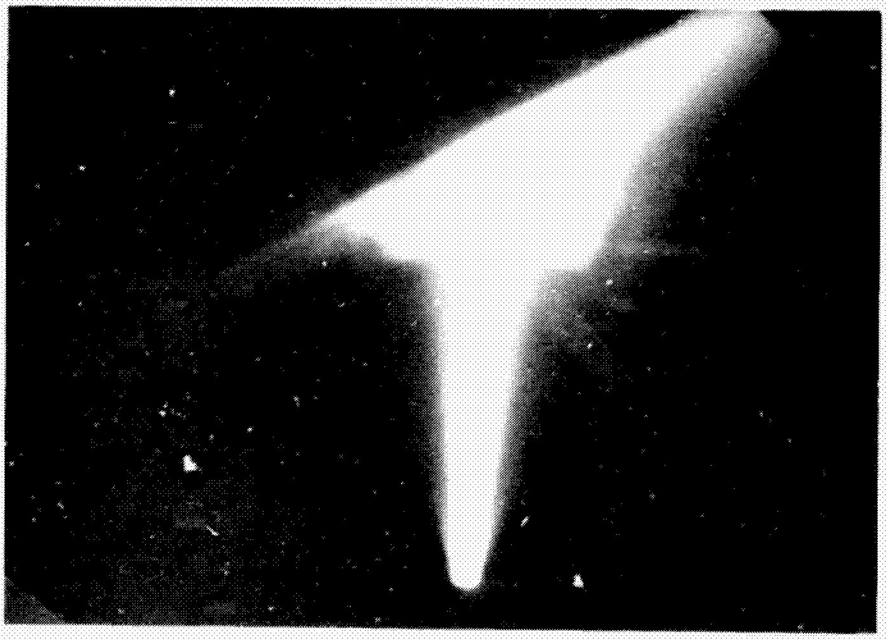

15% Aℓ Propellant, $\psi = 60^{\circ}$

Fig. 58 - Photographs of 10% and 15% Aℓ Propellant Exhaust Plumes Impinging on Flat Plate Centered at $x/D_{exit} = 20$ at a Simulated Altitude of 100,000 ft

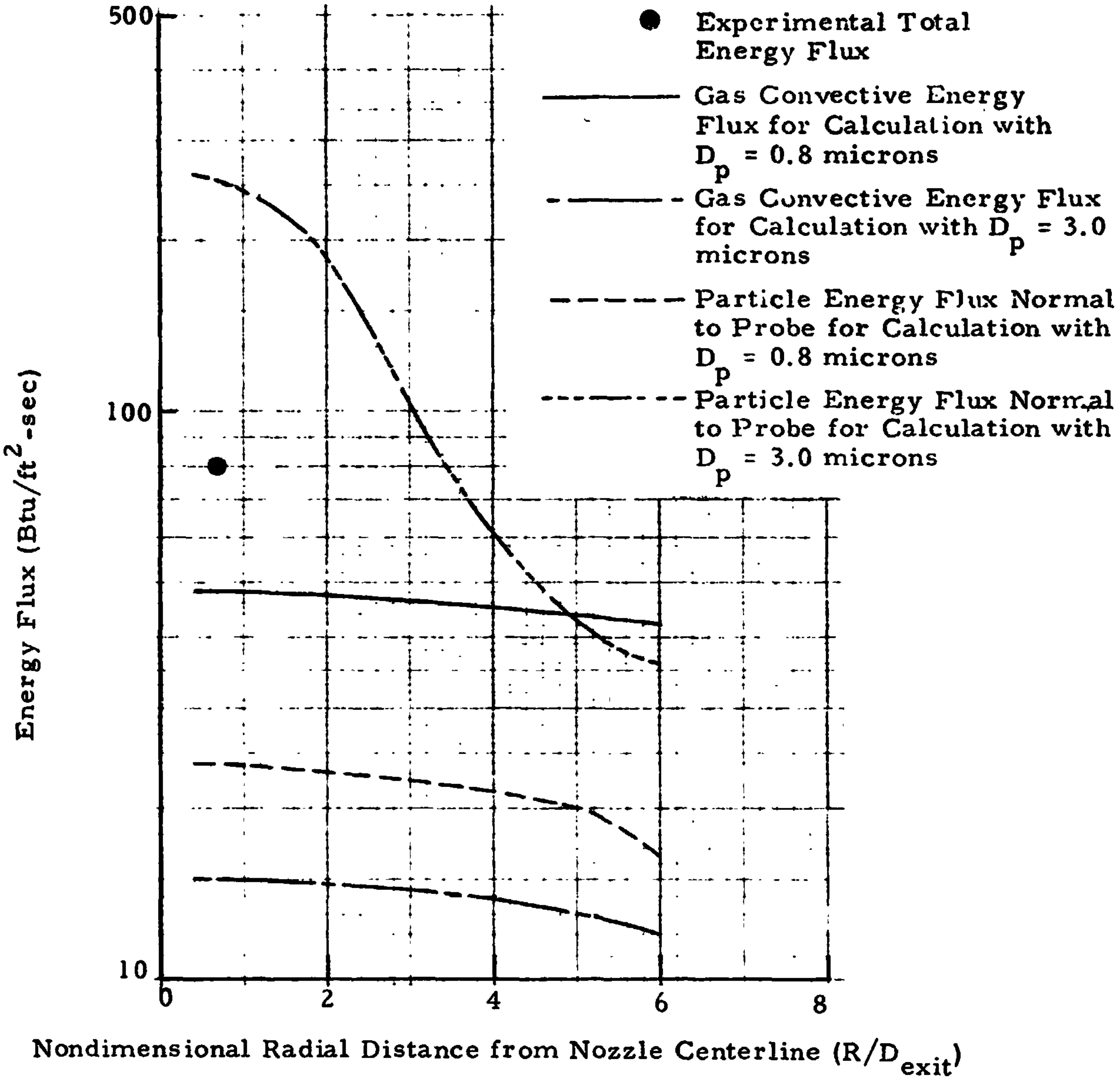

Fig. 59 - Comparison of Experimental and Analytical Energy Flux at x/D_{exit} = 20 for the 2% Al Propellant with Analytical Calculations Using Different Mass Mean Particle Diameters

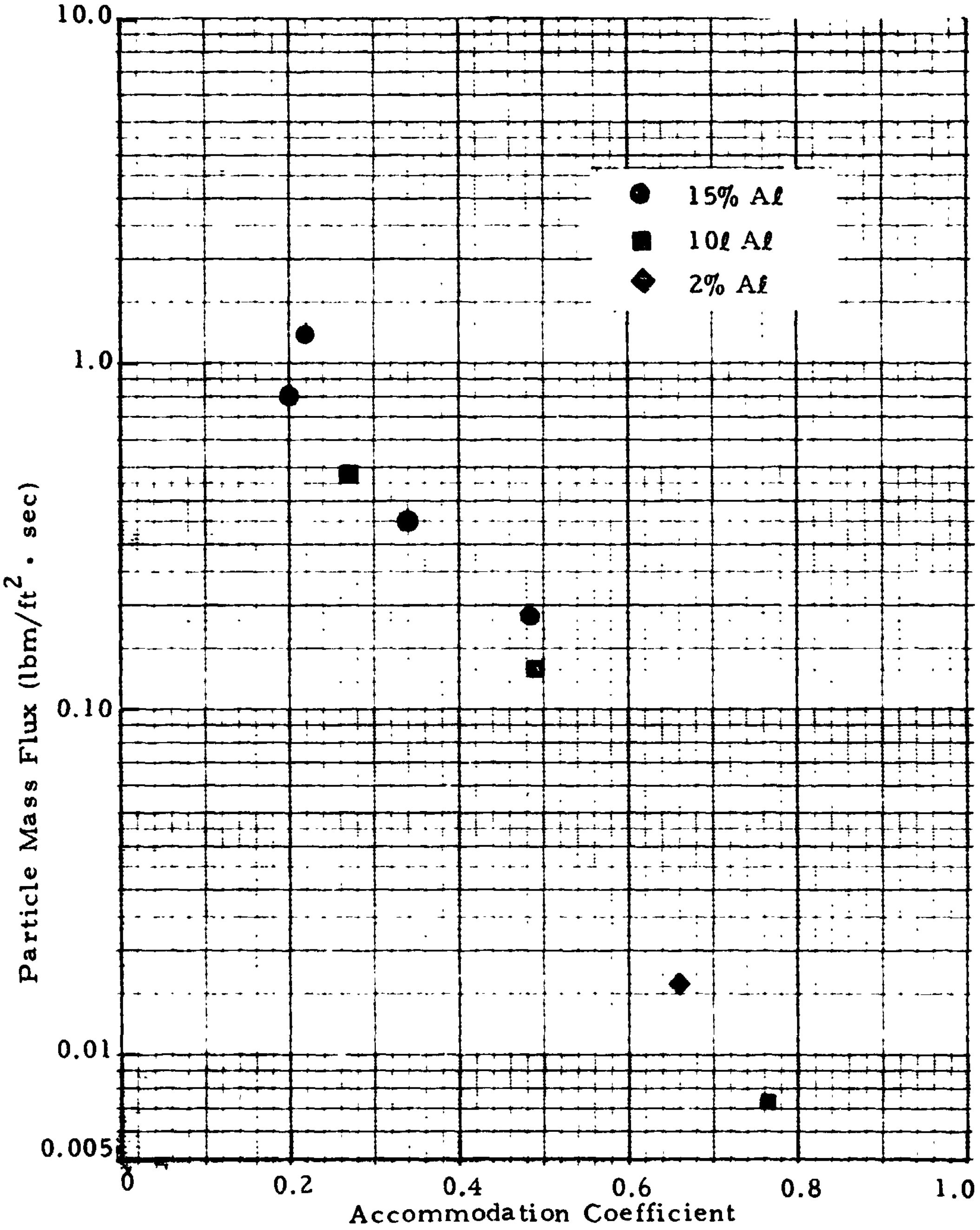

Fig. 60 - Particle Mass Flux as a Function of Accommodation Coefficient for 2, 10 and 15% Aℓ Loadings

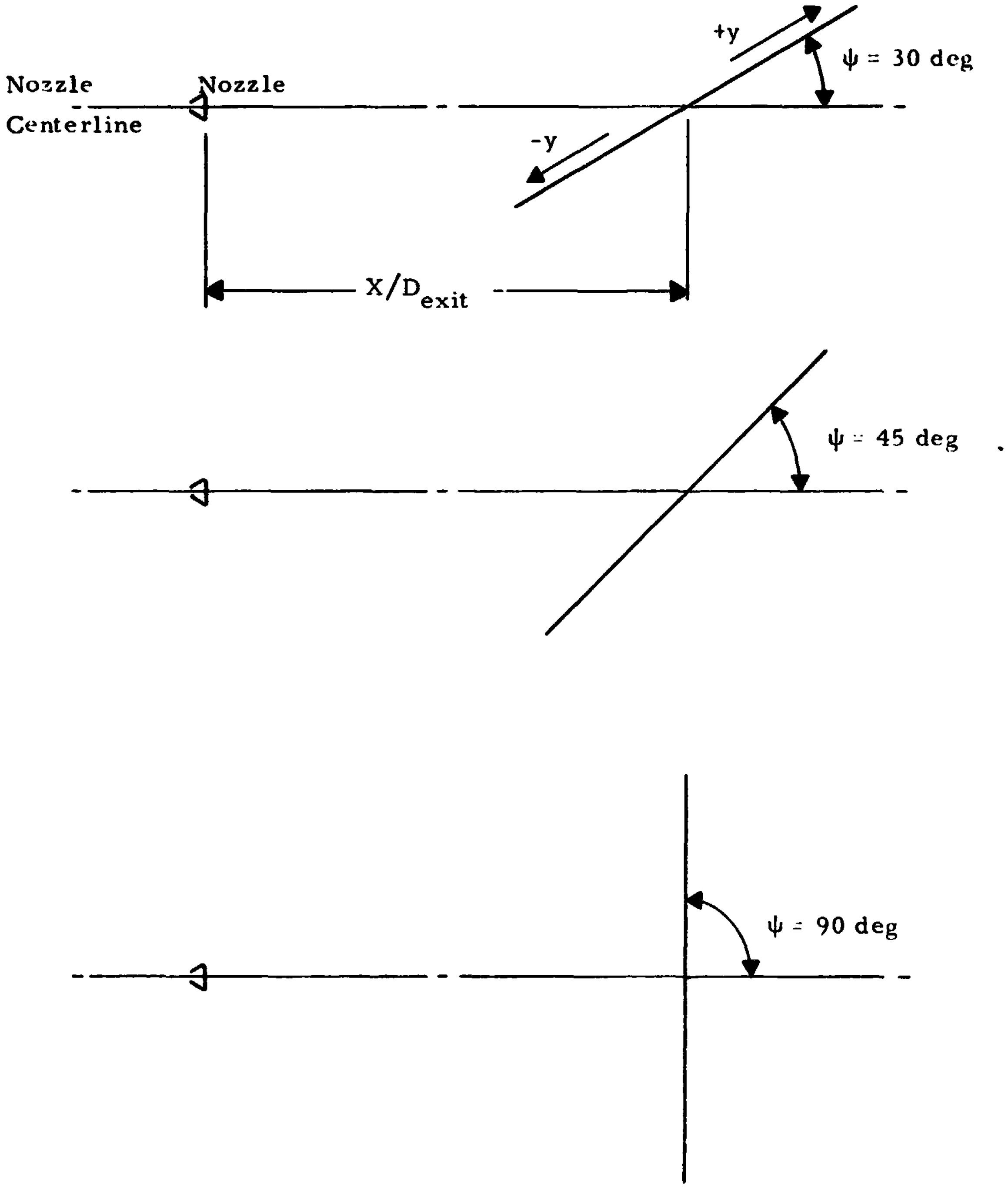

Fig. 61 - Definition of Flat Plate Configurations Investigated in Analysis

REPRODUCIBILITY OF THE
ORIGINAL PAGE IS POOR

ψ = 45 deg, x/D_{exit} = 12

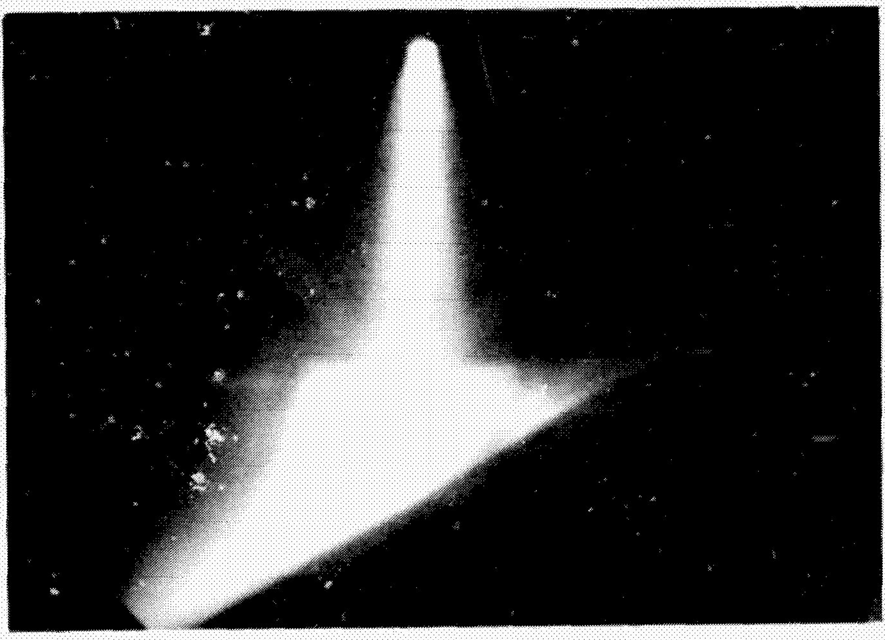

ψ = 60 deg, x/D_{exit} = 20

Fig. 62 - Photographs of the 15% Aℓ Propellant Impinging on the Flat Plate Inclined at Various Angles to the Nozzle Centerline

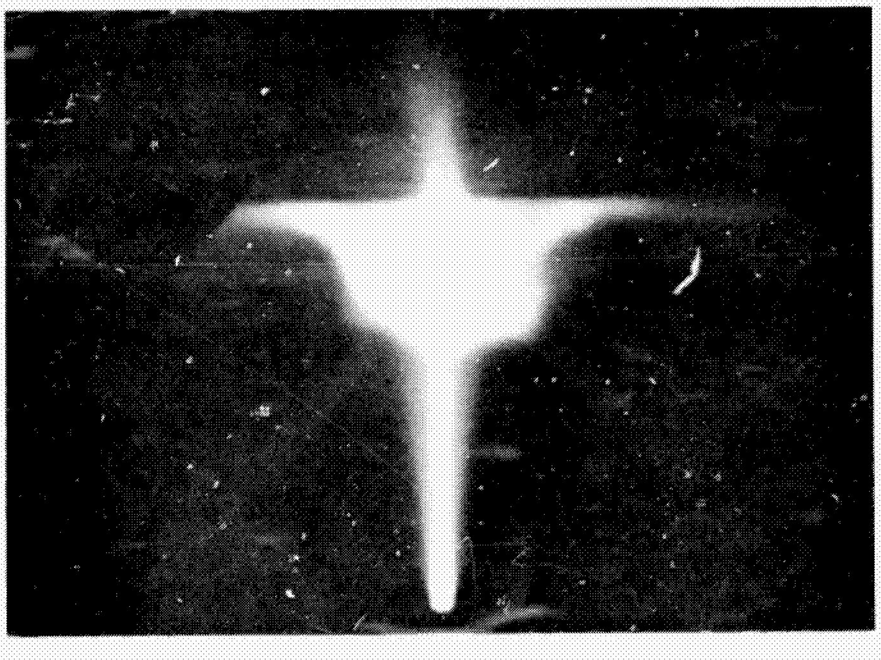

ψ = 90 deg, x/D_{exit} = 20

Fig. 62 (Concluded)

15% Aℓ, ψ = 45 deg, x/D_{exit} = 5

2% Aℓ, ψ = 45 deg, x/D_{exit} = 5

Fig. 63 - Photographs of the 15 and 2% Aℓ Propellants Impinging on the Flat Plate at a Simulated Altitude of 50,000 ft

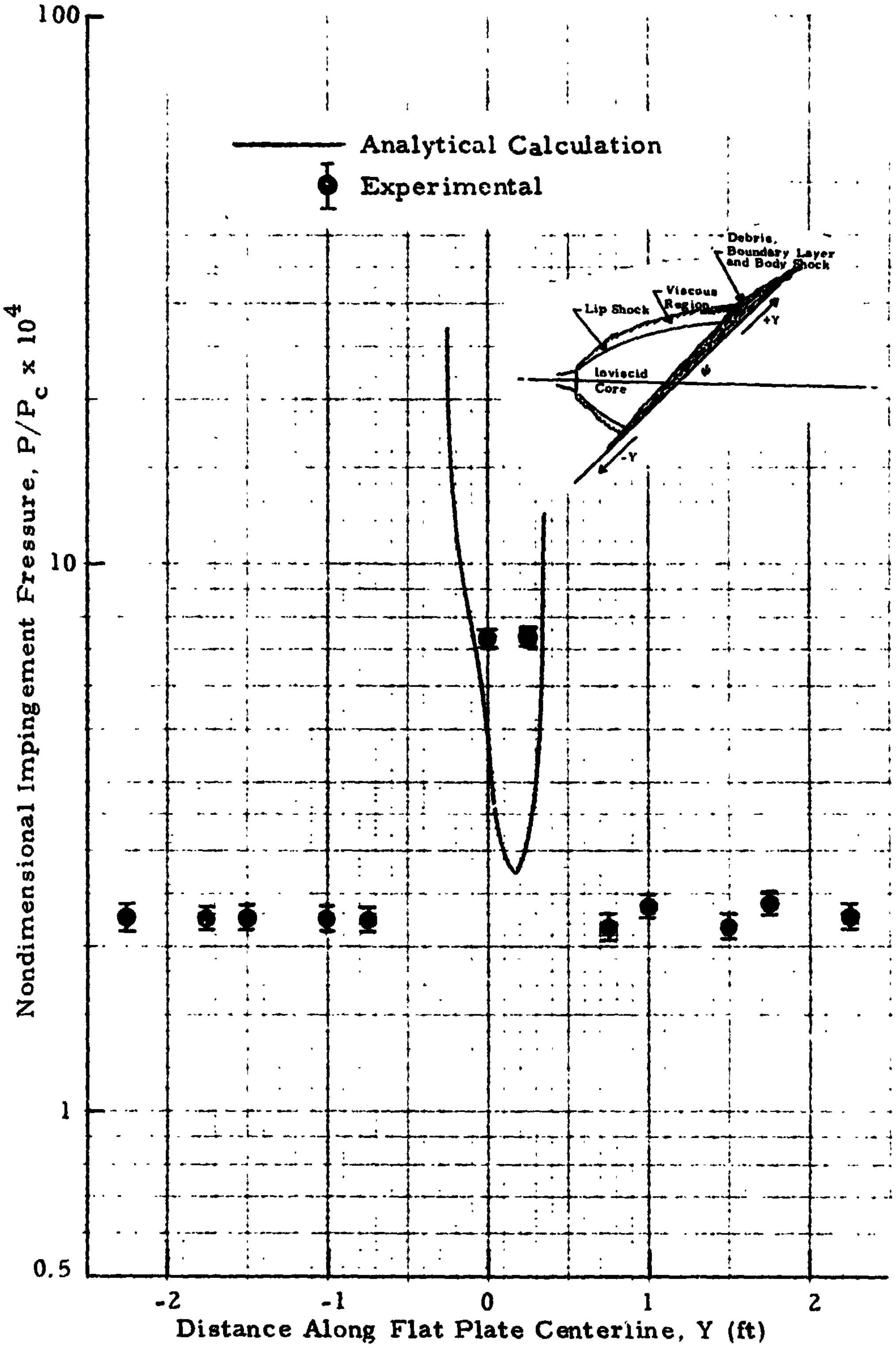

Fig. 64 - Comparison of Experimental and Analytical Impingement Pressure Along Centerline of Flat Plate for 2% Al Propellant at $x/D_{exit} = 5$, $\psi = 45$ deg, and a Simulated Altitude of 50,000 ft

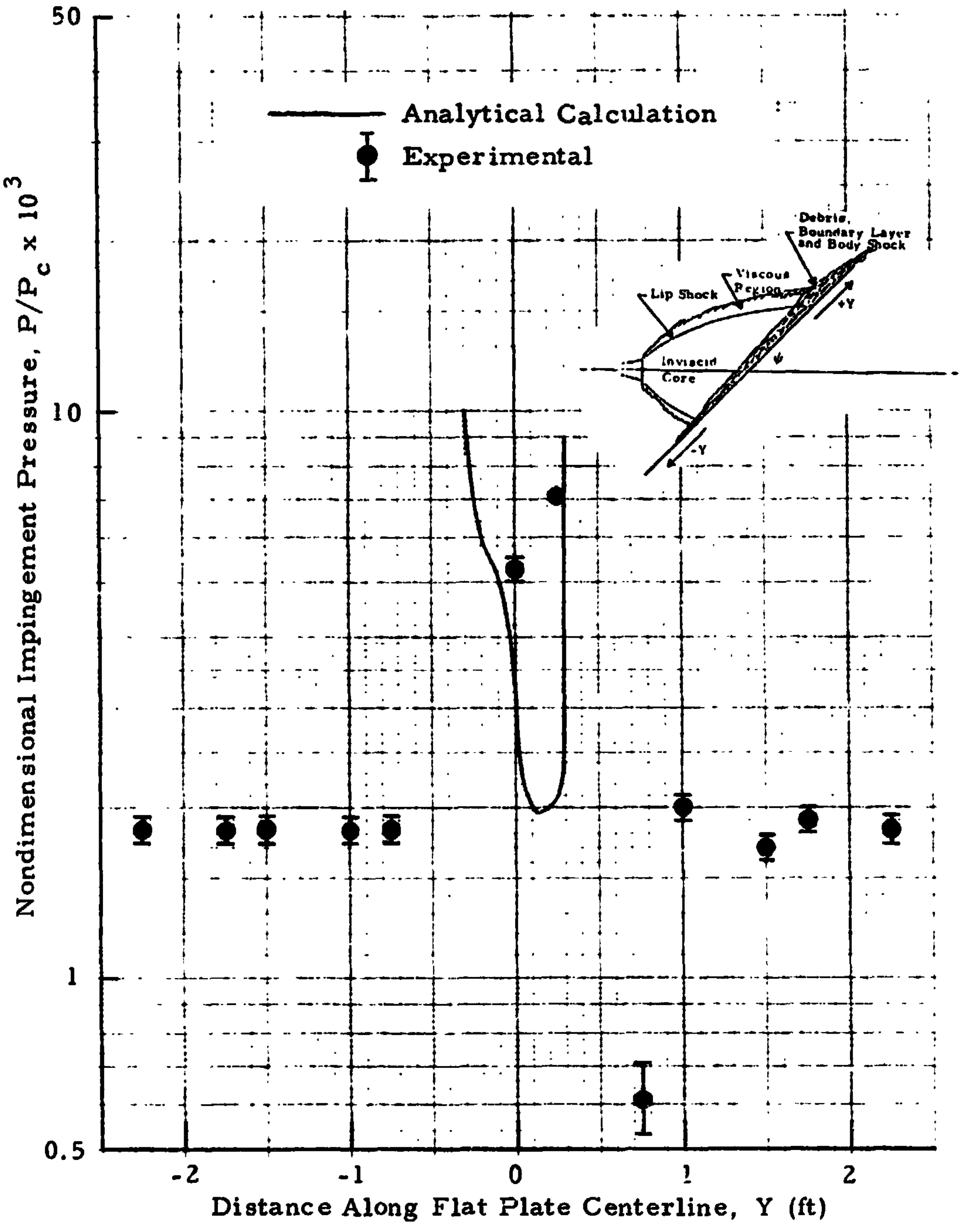

Fig. 65 - Comparison of Experimental and Analytical Impingement Pressure Along Centerline of Flat Plate for 10% Al Propellant at $x/D_{exit} = 5$, $\psi = 45$ deg and a Simulated Altitude of 50,000 ft

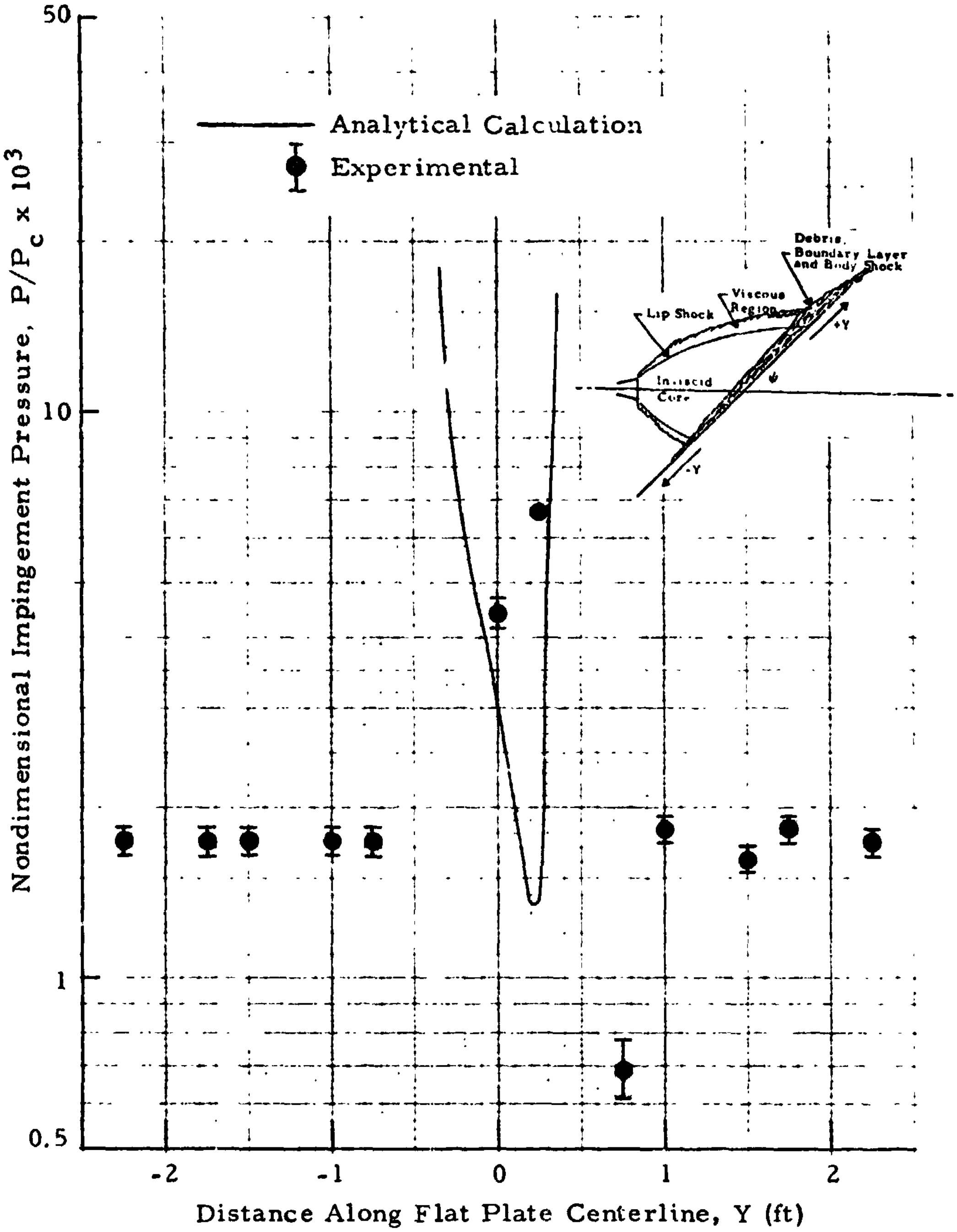

Fig. 66 - Comparison of Experimental and Analytical Impingement Pressure Along Centerline of Flat Plate for 15% Al Propellant at $x/D_{exit} = 5$, $\psi = 45$ deg, and a Simulated Altitude of 50,000 ft

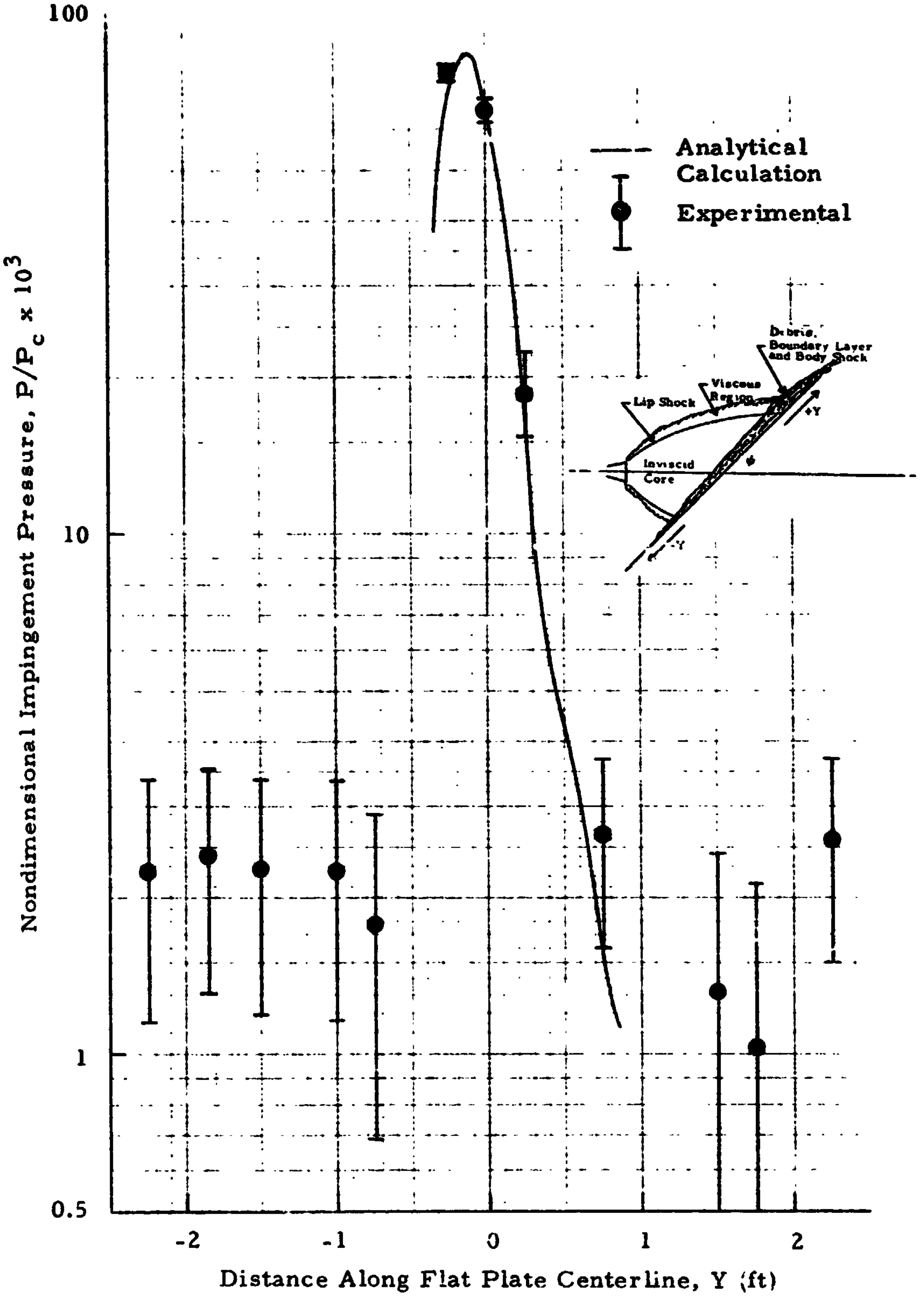

Fig. 67 - Comparison of Experimental and Analytical Impingement Pressure Along Centerline of Flat Plate for 2% Al Propellant at $X/D_{exit} = 5$, $\psi = 45$ deg and a Simulated Altitude of 100,000 ft

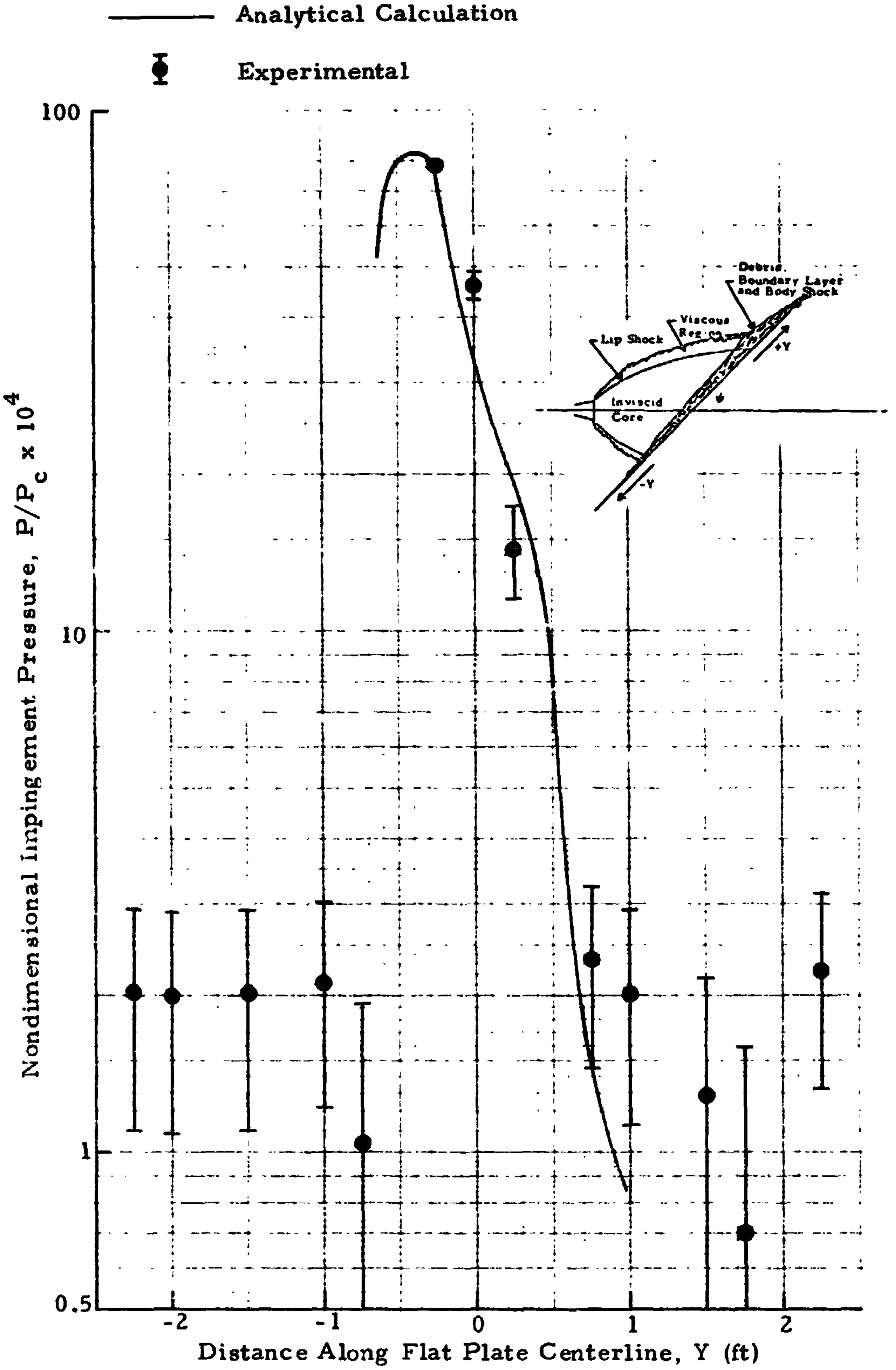

Fig. 68 - Comparison of Experimental and Analytical Impingement Pressure Along Centerline of Flat Plate for 10% Al Propellant at $x/D_{exit} = 5$, $\psi = 45$ deg and a Simulated Altitude of 100,000 ft

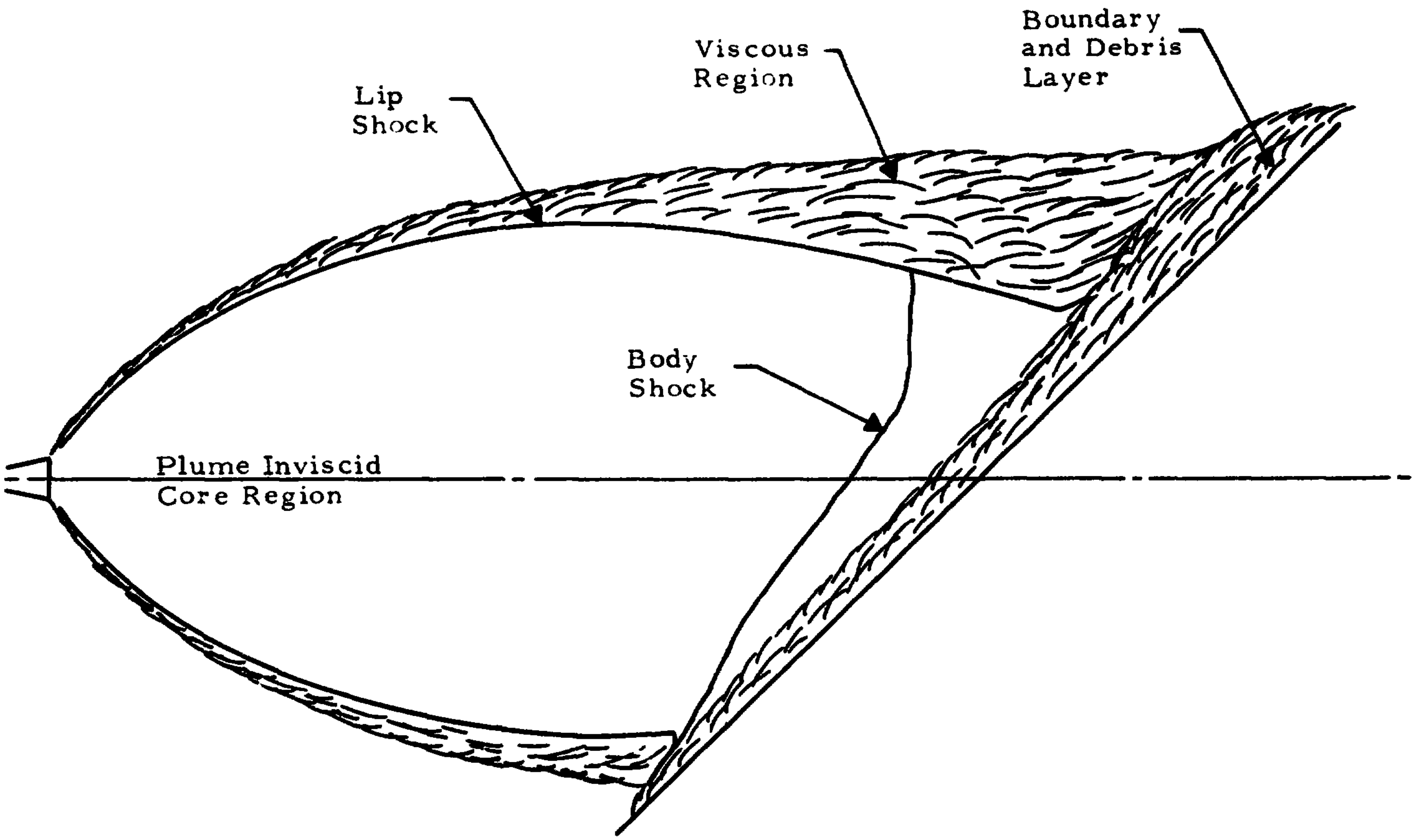

Fig. 69 - Schematic of Exhaust Plume Impinging on Flat Plate Located in Plume Far Field

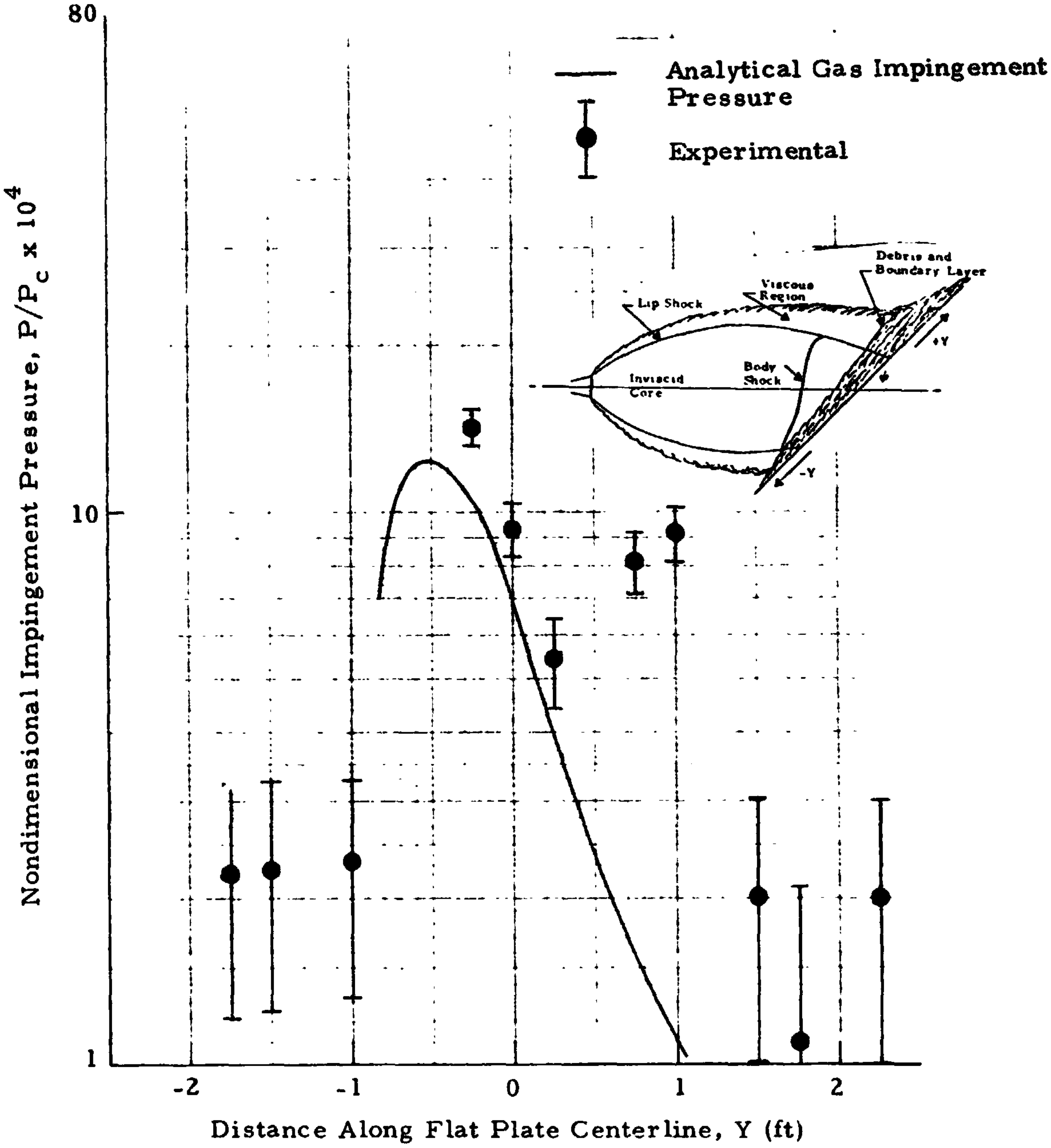

Fig. 70 - Comparison of Experimental and Analytical Impingement Pressure Along Centerline of Flat Plate for 2% Al Propellant at $X/D_{exit} = 12$, $\psi = 45$ deg and a Simulated Altitude of 100,000 ft

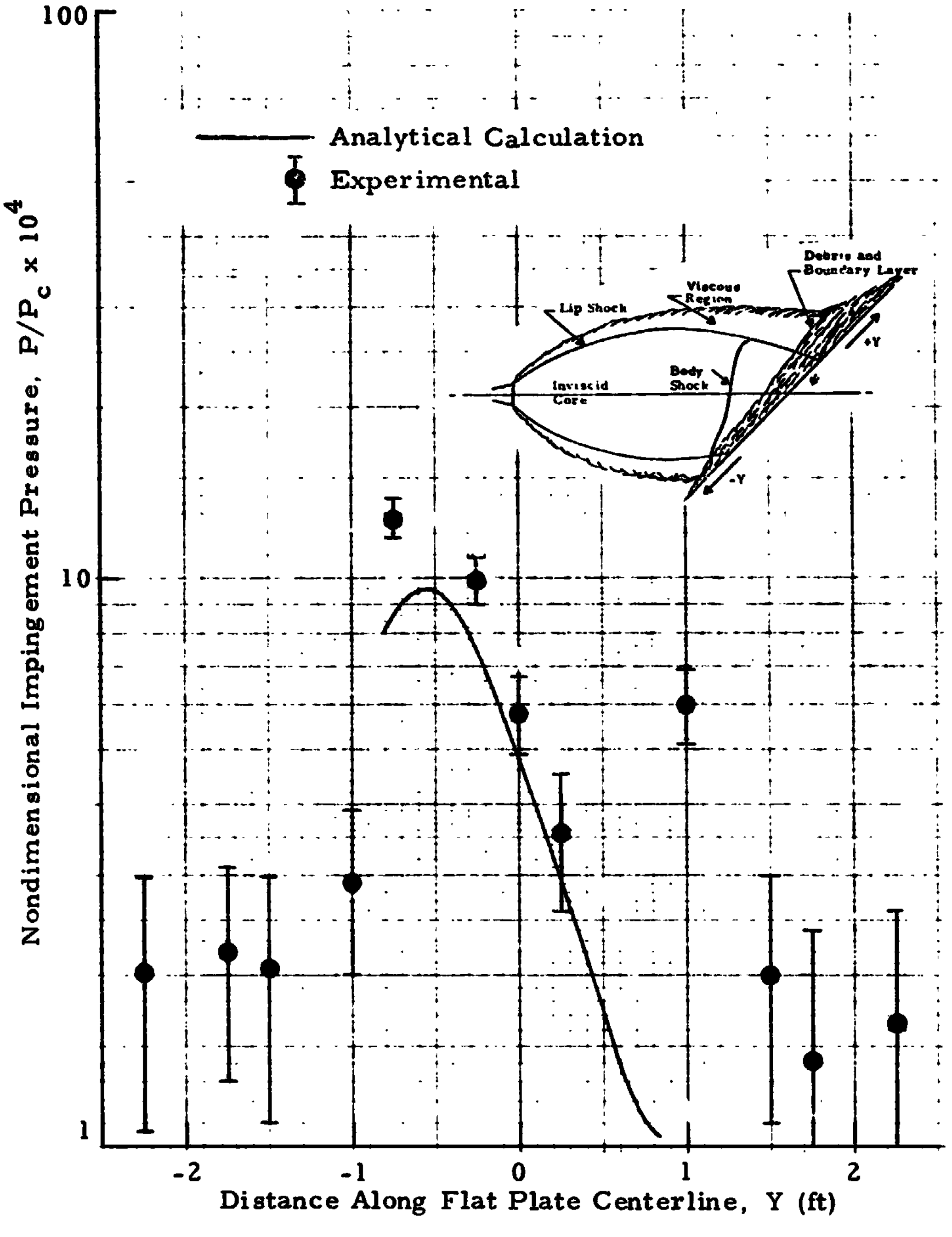

Fig. 71 - Comparison of Experimental and Analytical Impingement Pressure Along Centerline of Flat Plate for 10% Aℓ Propellant at $x/D_{exit} = 12$, $\psi = 45$ deg and a Simulated Altitude of 100,000 ft

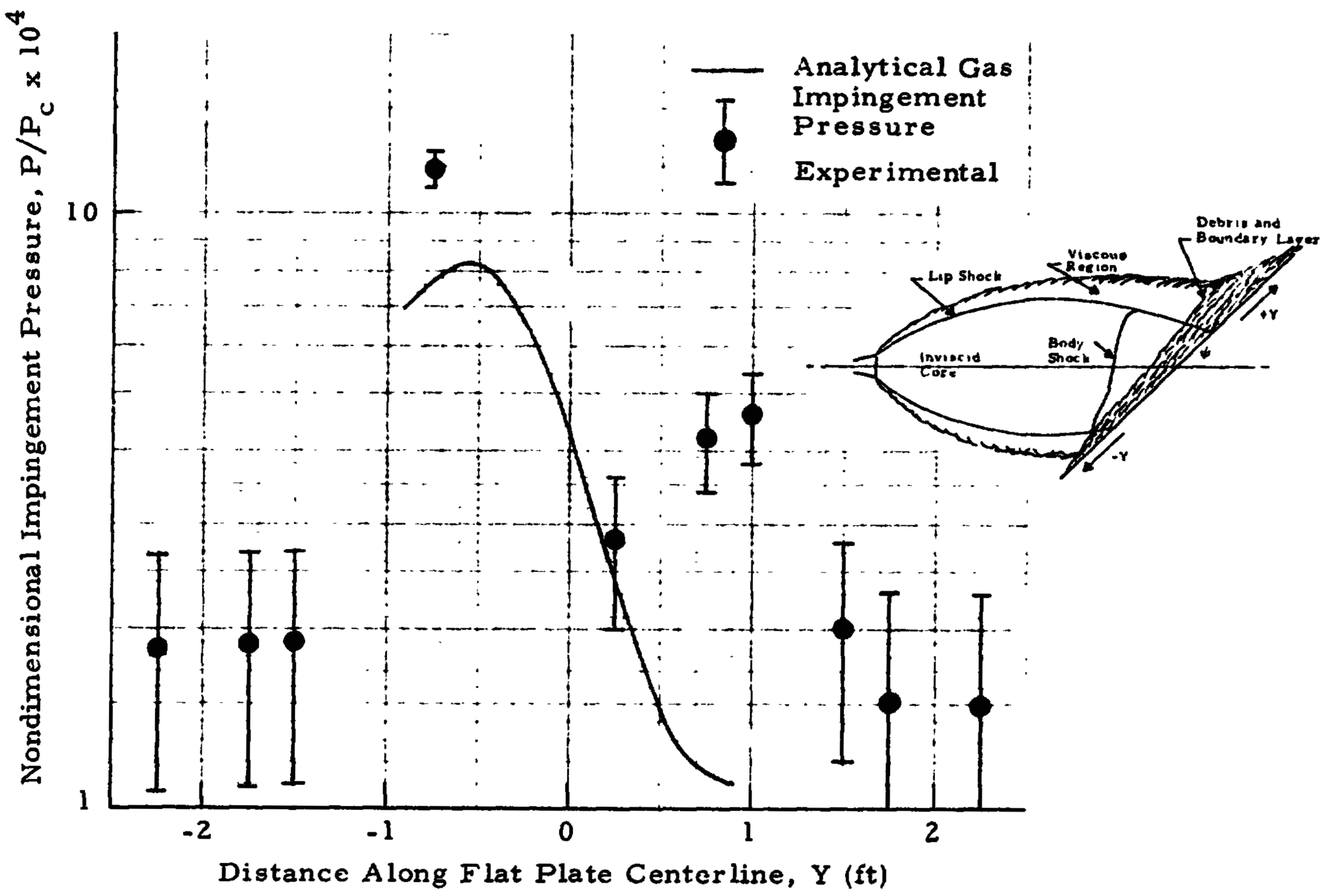

Fig. 72 - Comparison of Experimental and Analytical Impingement Pressure Along Centerline of Flat Plate for 15% Al Propellant at $X/D_{exit} = 12$, $\psi = 45$ deg, and a Simulated Altitude of 100,000 ft

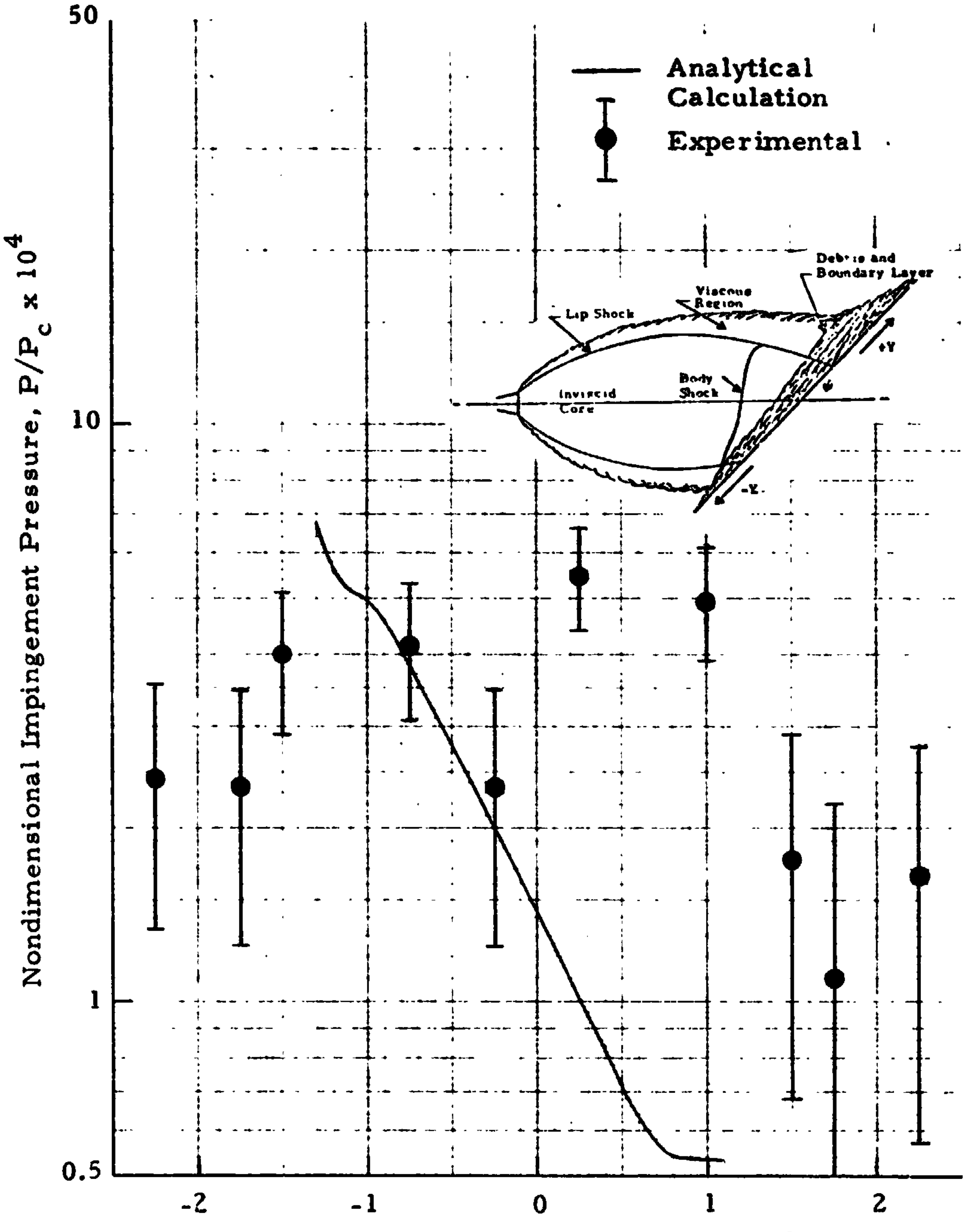

Fig. 73 - Comparison of Experimental and Analytical Impingement Pressure Along Centerline of Flat Plate for 2% Al Propellant at $X/D_{exit} = 20$, $\psi = 30$ deg and a Simulated Altitude of 100,000 ft

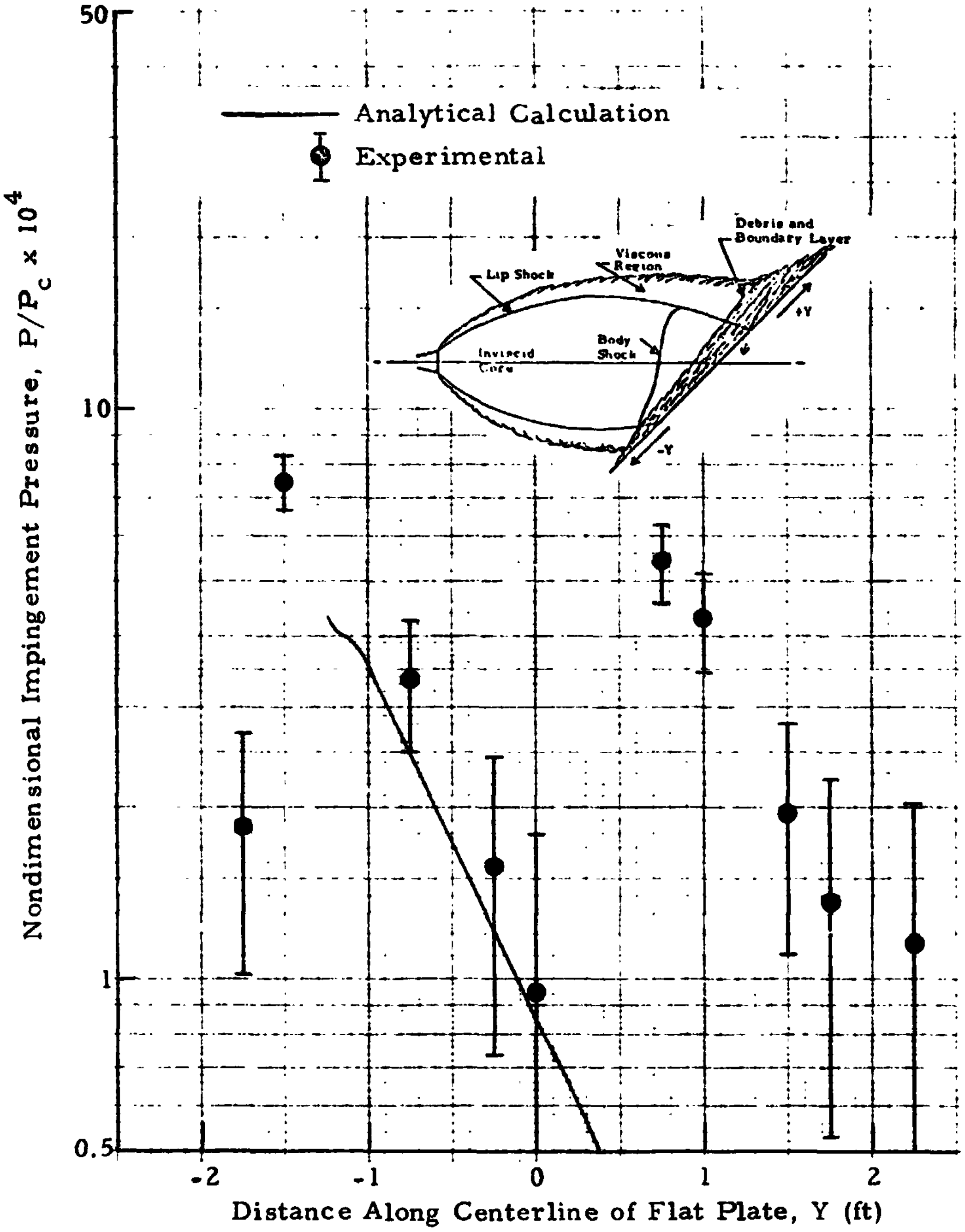

Fig. 74 - Comparison of Experimental and Analytical Impingement Pressure Along Centerline of Flat Plate for 10% Al Propellant at $x/D_{exit} = 20$, $\psi = 30$ deg and a Simulated Altitude of 100,000 ft

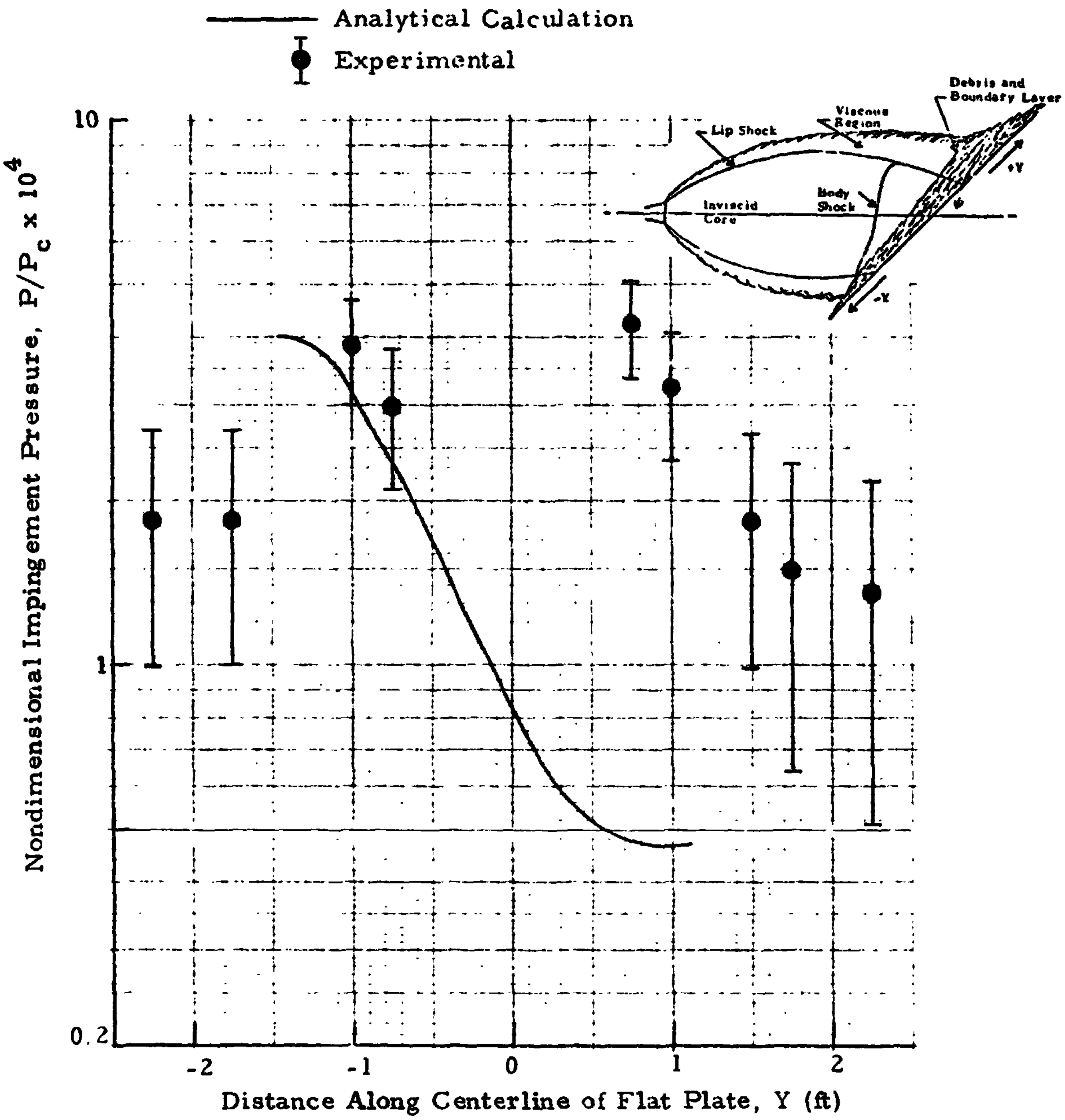

Fig. 75 - Comparison of Experimental and Analytical Impingement Pressure Along Centerline of Flat Plate for 15% Al Propellant at $x/D_{exit} = 20$, $\psi = 30$ deg, and a Simulated Altitude of 100,000 ft

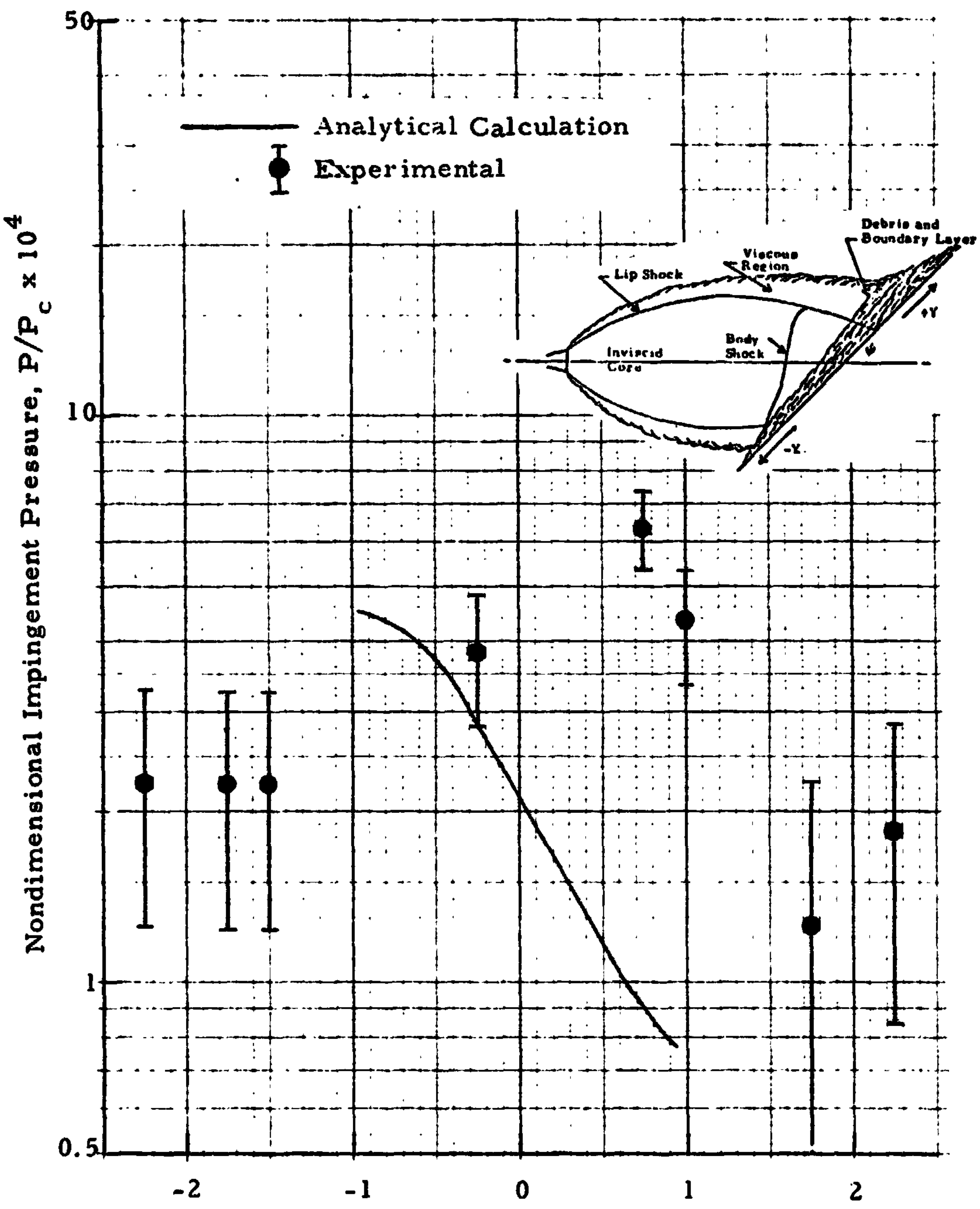

Fig. 76 - Comparison of Experimental and Analytical Impingement Pressure Along Centerline of Flat Plate for 2% Al Propellant at $x/D_{exit} = 20$, $\psi = 45$ deg, and a Simulated Altitude of 100,000 ft

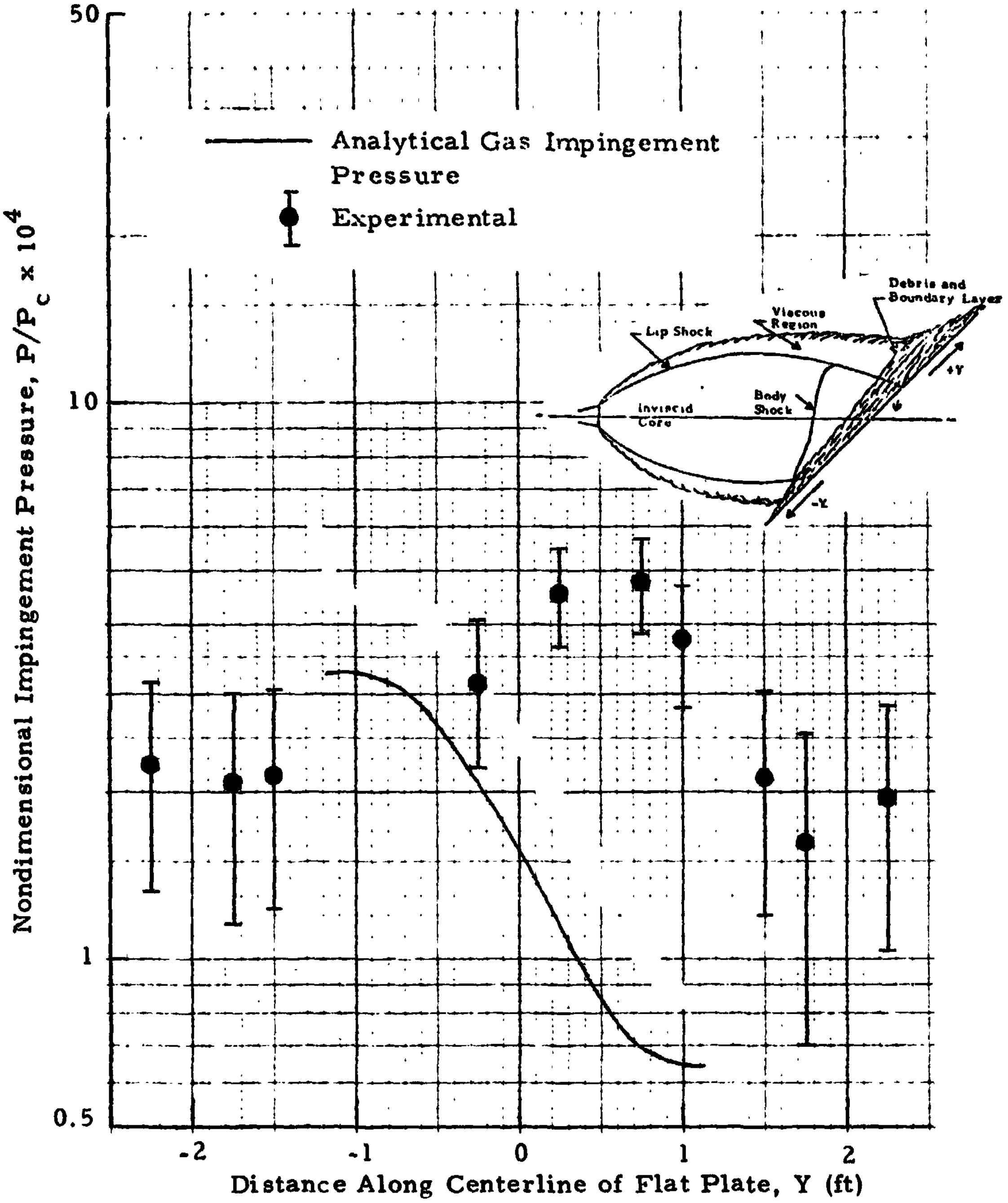

Fig. 77 - Comparison of Experimental and Analytical Impingement Pressure Along Centerline of Flat Plate for 10% Al Propellant at $x/D_{exit} = 20$, $\psi = 45$ deg, and a Simulated Altitude of 100,000 ft

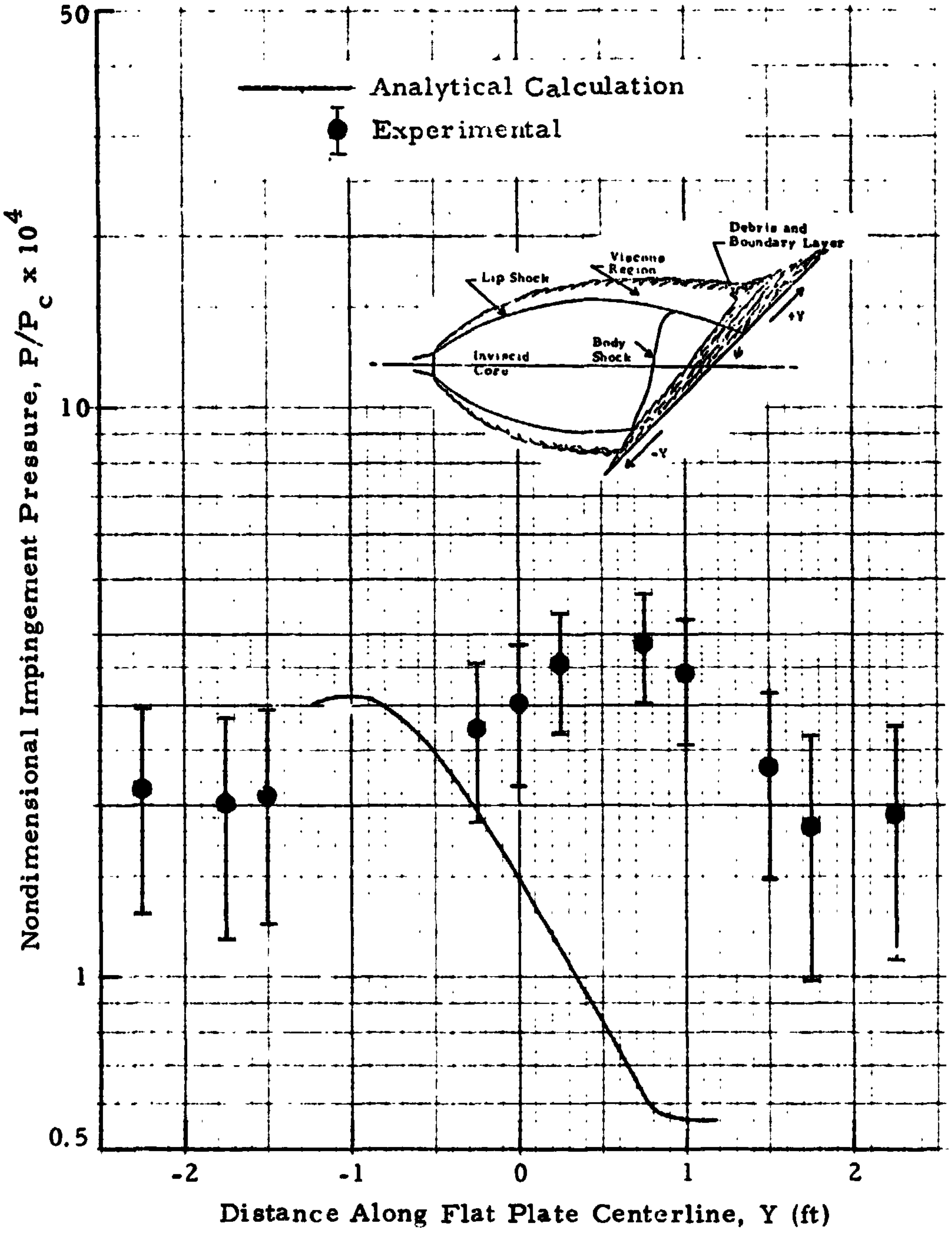

Fig. 78 - Comparison of Experimental and Analytical Impingement Pressure Along Centerline of Flat Plate for 15% Aℓ Propellant at $x/D_{exit} = 20$, $\psi = 45$ deg and a Simulated Altitude of 100,000 ft

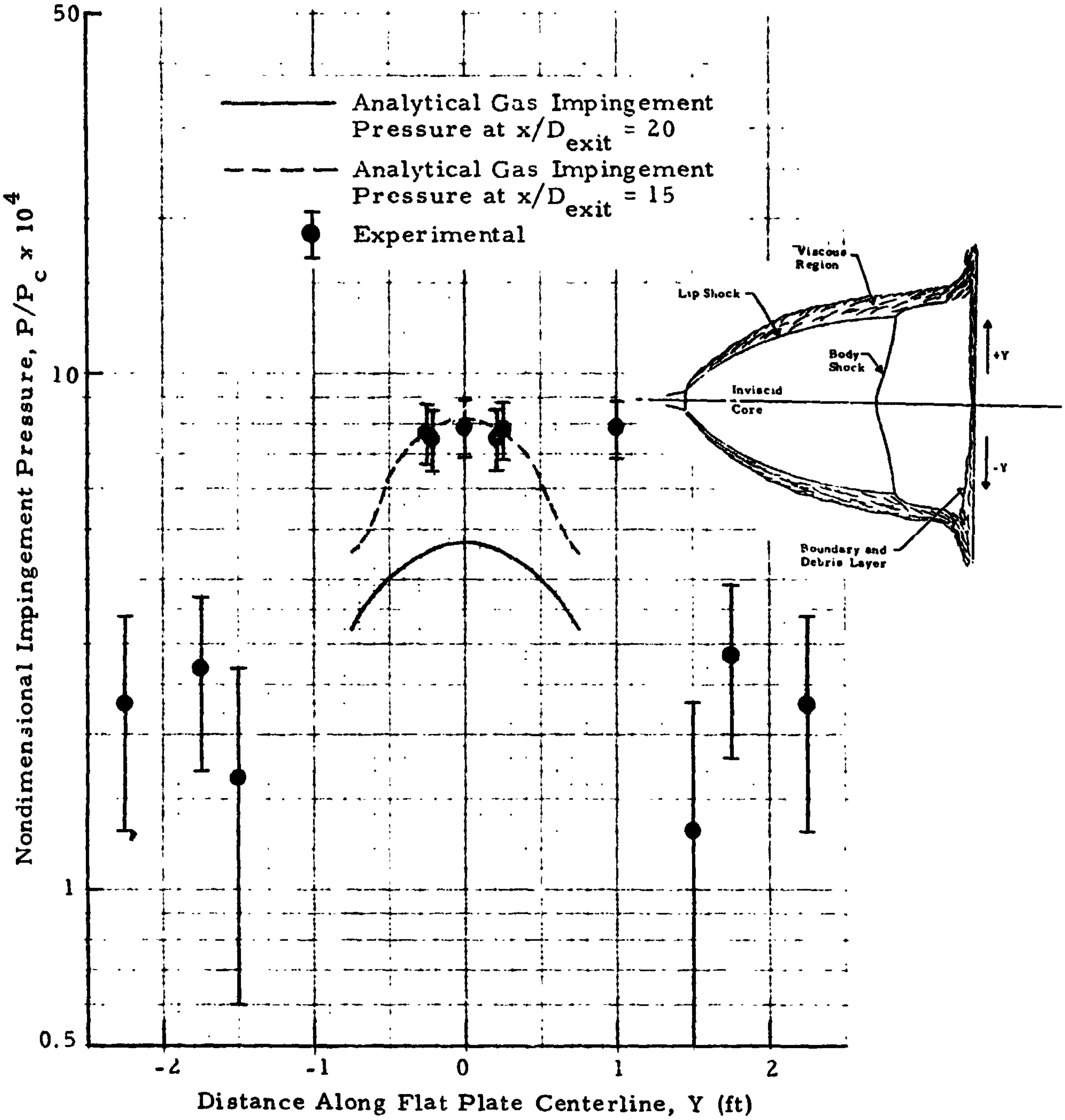

Fig. 79 - Comparison of Experimental and Analytical Impingement Pressure Along Centerline of Flat Plate for 2% Al Propellant at $x/D_{exit} = 20$, $\psi = 90$ deg, and a Simulated Altitude of 100,000 ft

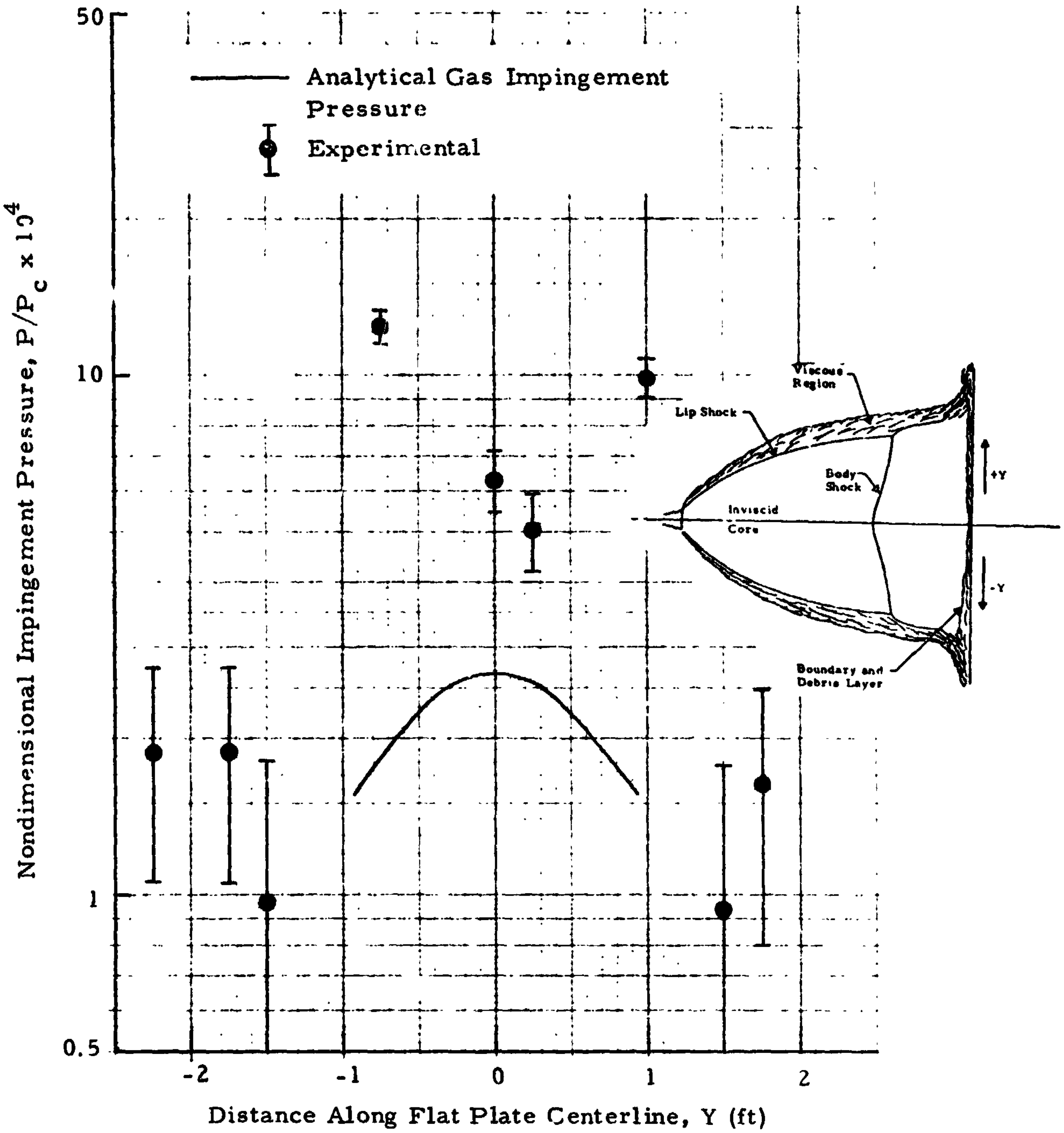

Fig. 80 - Comparison of Experimental and Analytical Impingement Pressure Along Centerline of Flat Plate for 10% Aℓ Propellant at $x/D_{exit} = 20$, $\psi = 90$ deg, and a Simulated Altitude of 100,000 ft

REPRODUCIBILITY OF THE
ORIGINAL PAGE IS POOR

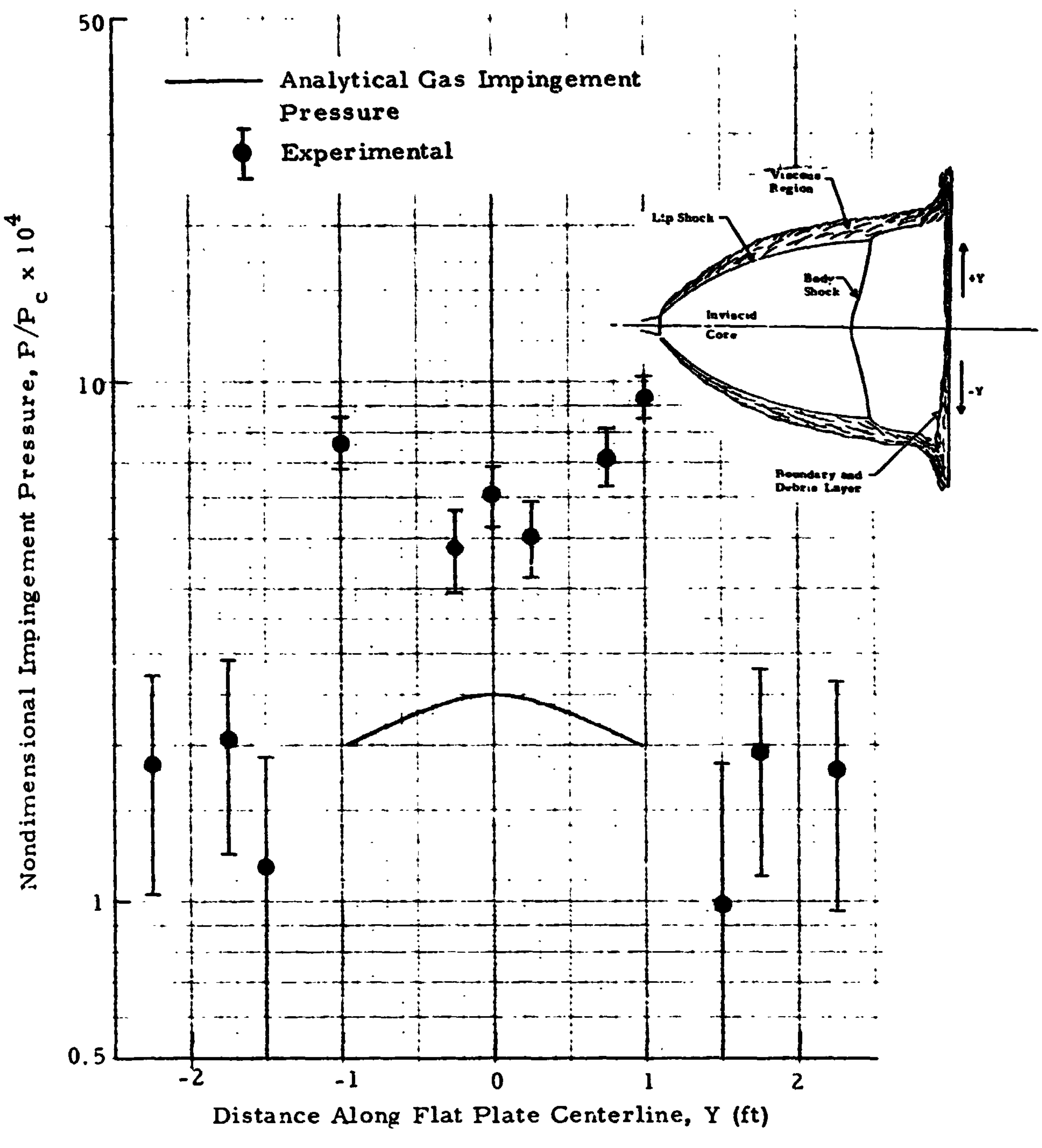

Fig. 81 - Comparison of Experimental and Analytical Impingement Pressure Along Centerline of Flat Plate for 15% Al Propellant at $x/D_{exit} = 20$, $\psi = 90$ deg, and a Simulated Altitude of 100,000 ft

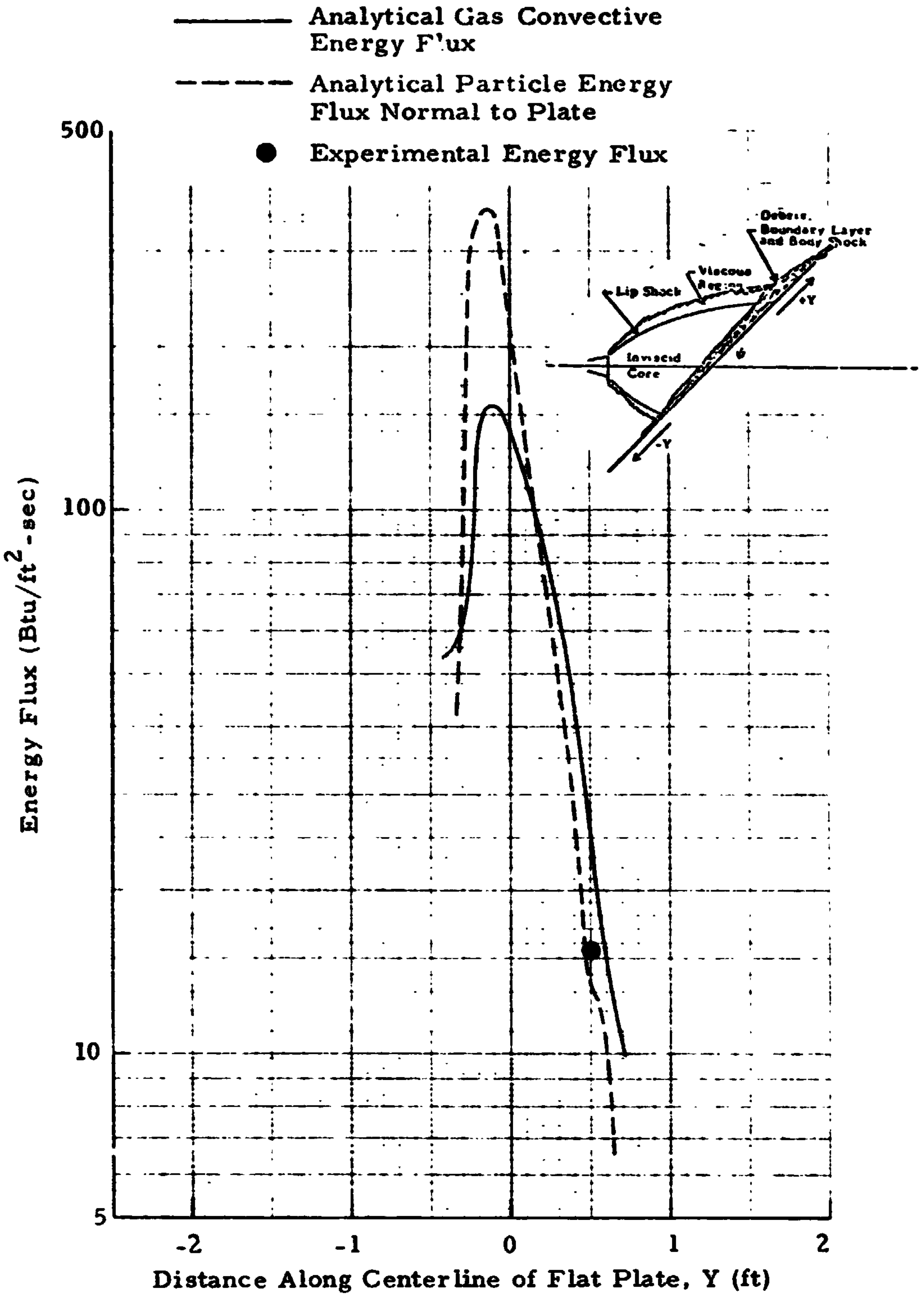

Fig. 82 - Comparison of Experimental and Analytical Energy Flux Along Centerline of Flat Plate for 2% Al Propellant at $X/D_{exit} = 5$, $\psi = 45$ deg and a Simulated Altitude of 100,000 ft

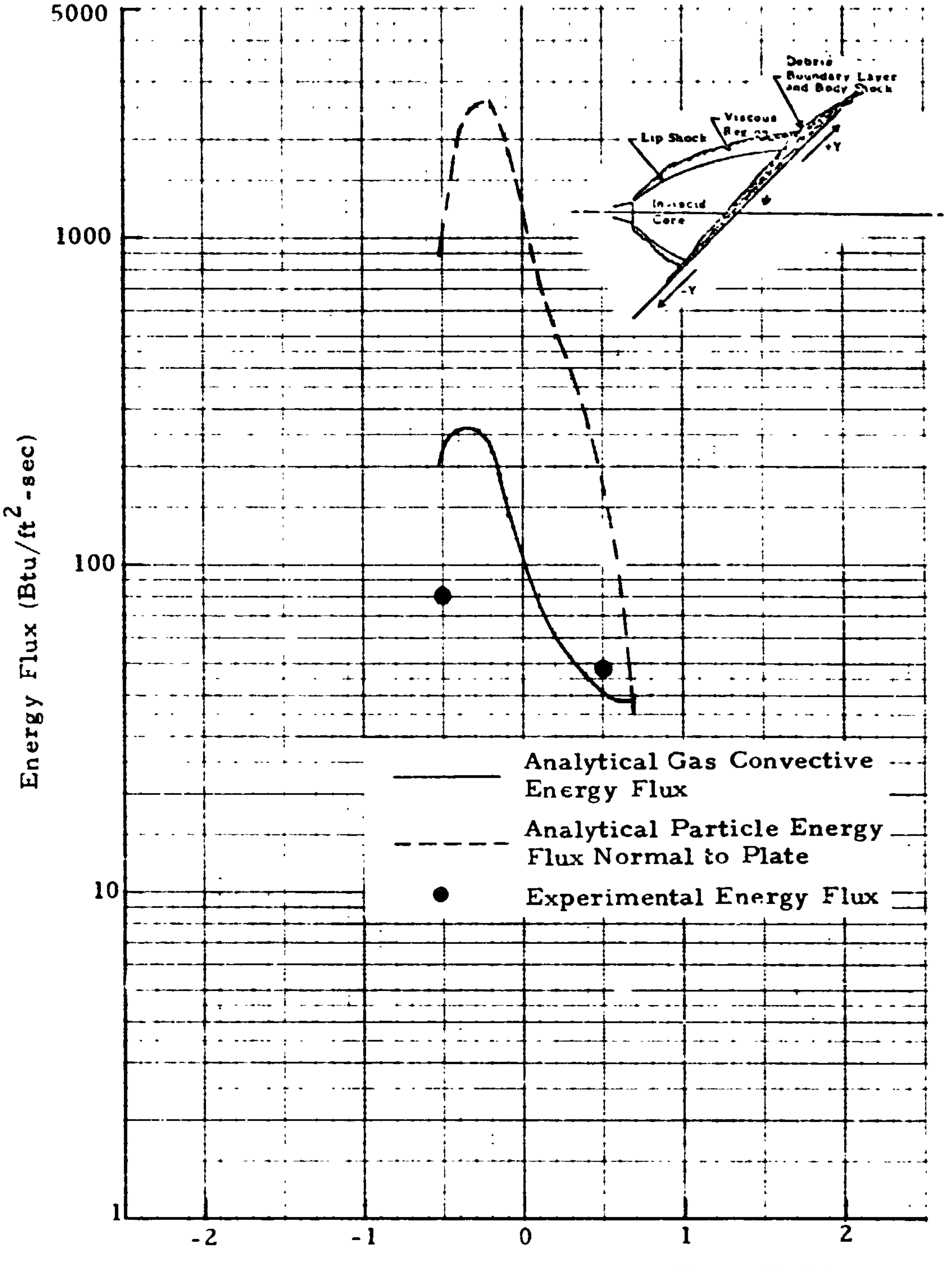

Fig. 83 - Comparison of Experimental and Analytical Energy Flux Along Centerline of Flat Plate for 10% Al Propellant at $x/D_{exit} = 5$, $\psi = 45$ deg and a Simulated Altitude of 100,000 ft

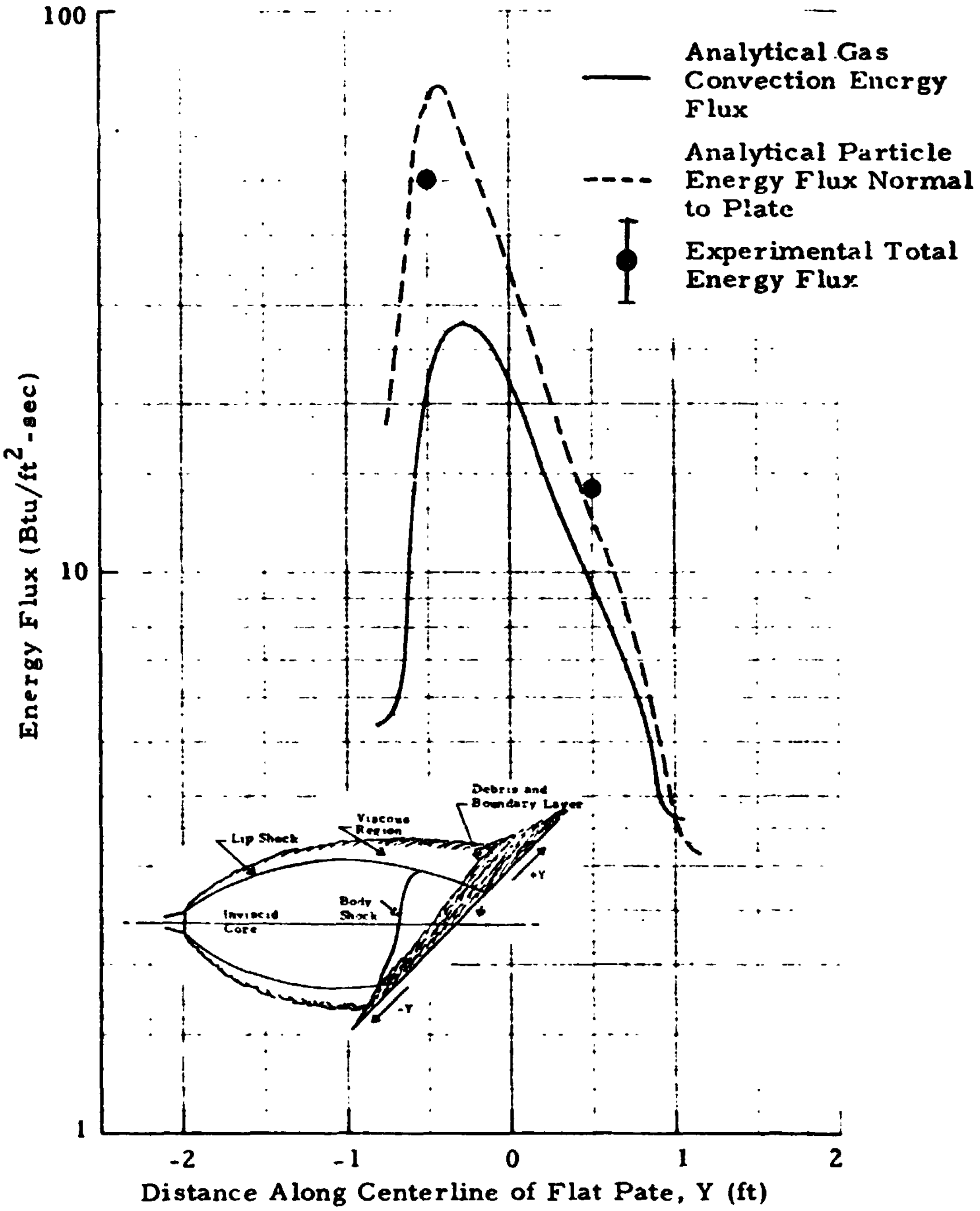

Fig. 84 - Comparison of Experimental and Analytical Energy Flux Along Centerline of Flat Plate for 2% Al Propellant at X/D_{exit} = 12, ψ = 45 deg and a Simulated Altitude of 100,000 ft

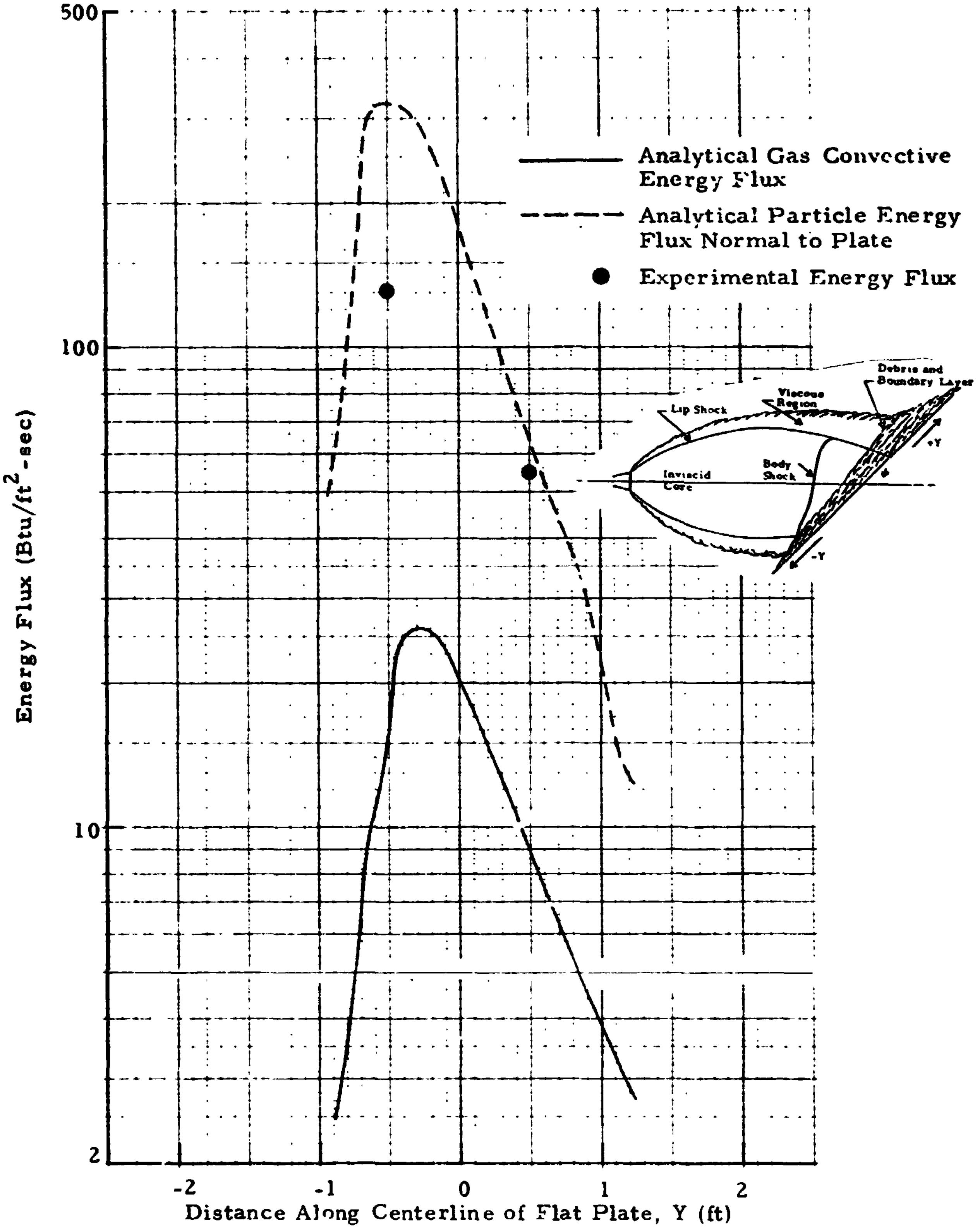

Fig. 85 - Comparison of Experimental and Analytical Energy Flux Along Centerline of Flat Plate for 10% Al Propellant at $x/D_{exit} = 12$, $\psi = 45$ deg, and a Simulated Altitude of 100,000 ft

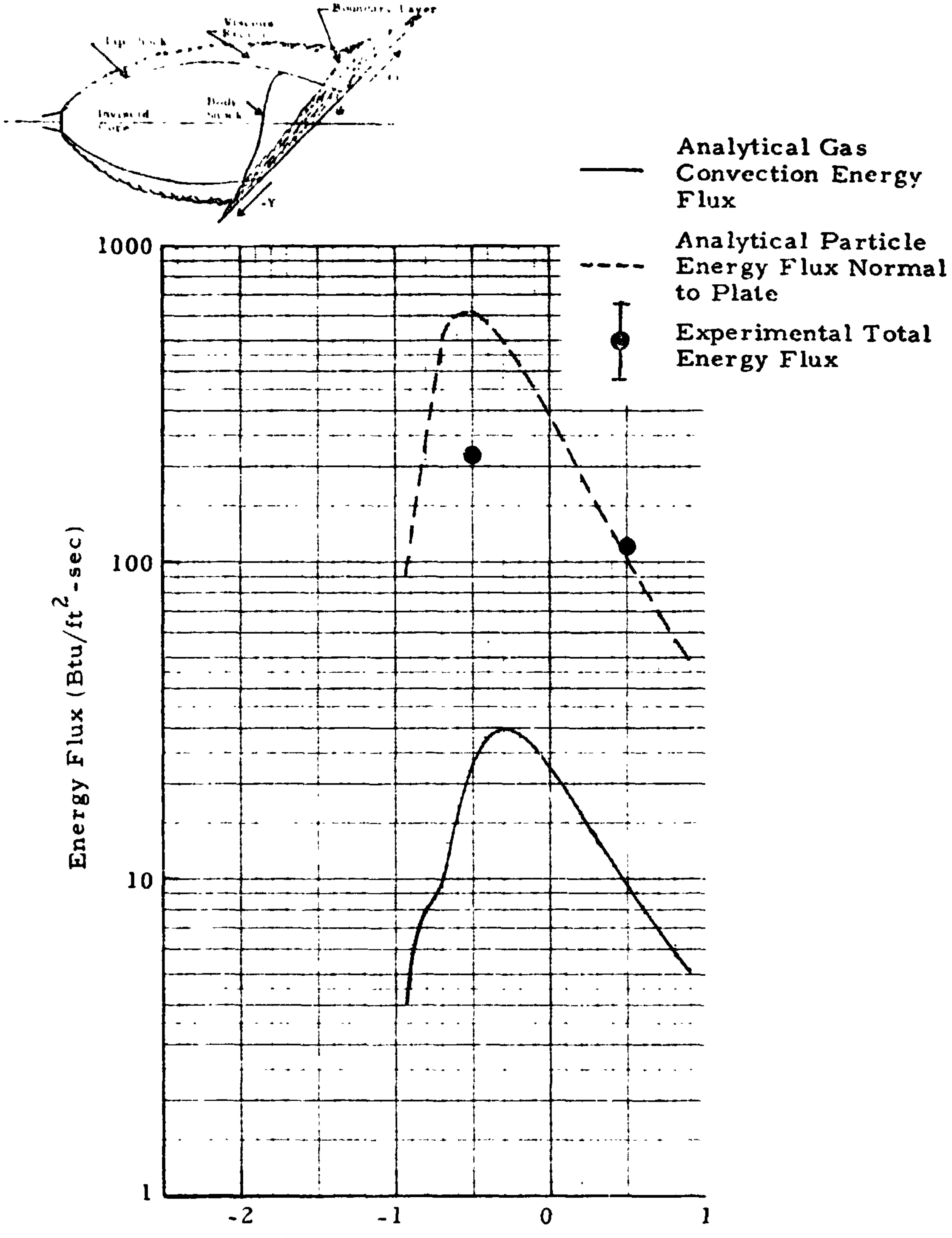

Fig. 86 - Comparison of Experimental and Analytical Energy Flux Along Centerline of Flat Plate for 15% Al Propellant at $X/D_{exit} = 12$, $\psi = 45$ deg and a Simulated Altitude of 100,000 ft

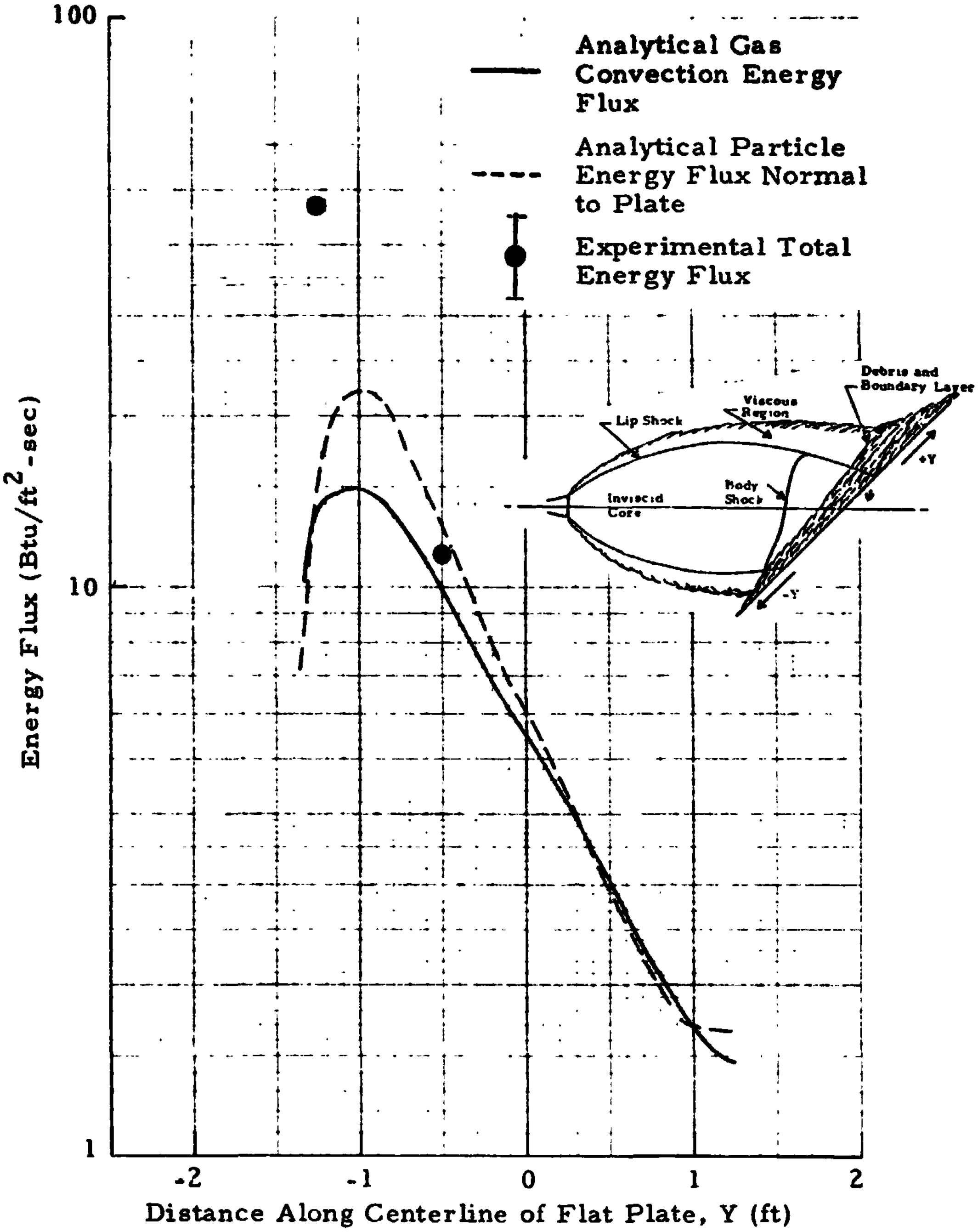

Fig. 87 - Comparison of Experimental and Analytical Energy Flux Along Centerline of Flat Plate for 2% Al Propellant at X/D$_{exit}$ = 20, ψ = 30 deg and a Simulated Altitude of 100,000 ft

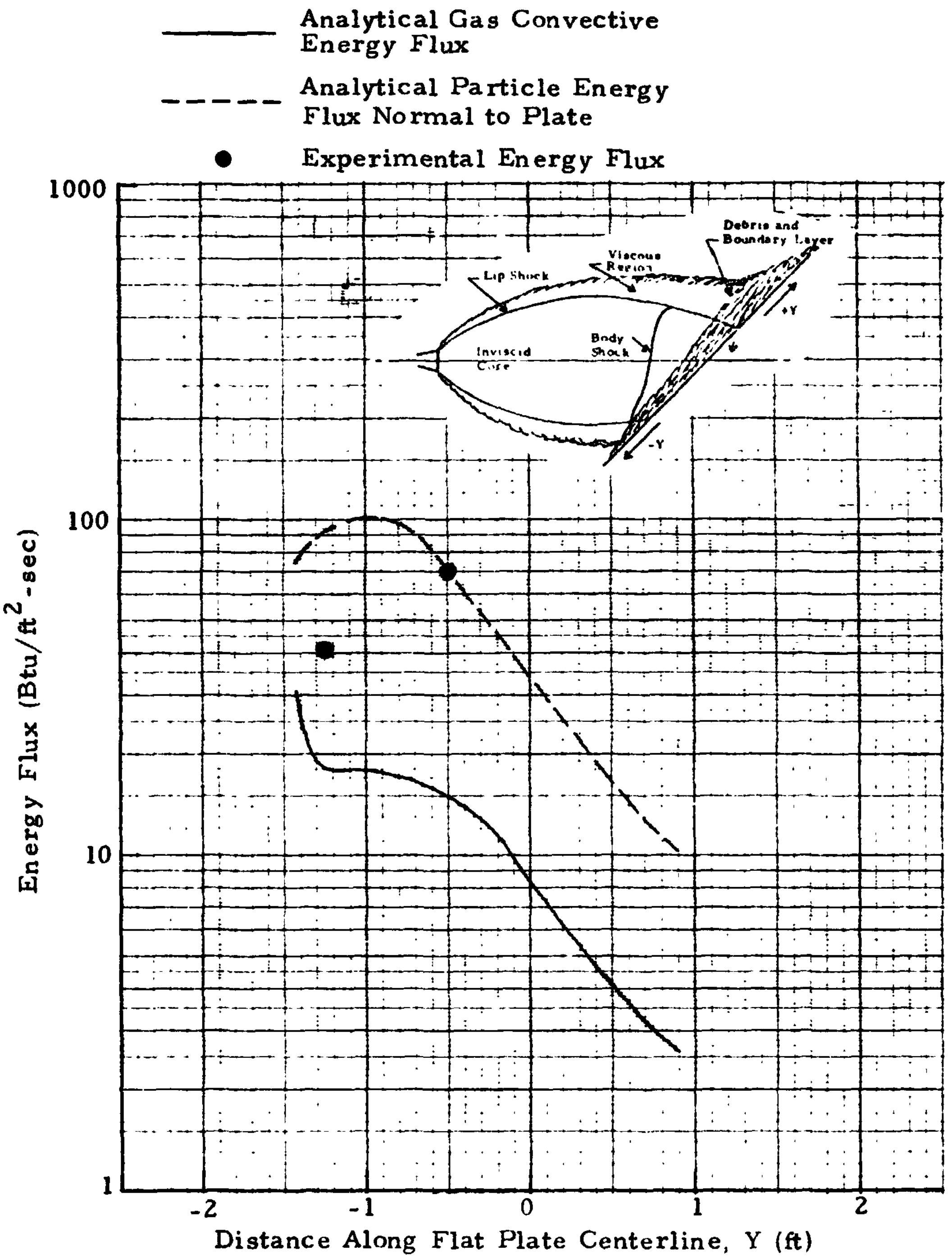

Fig. 88 - Comparison of Experimental and Analytical Energy Flux Along Centerline of Flat Plate for 10% Al Propellant at $x/D_{exit} = 20$, $\psi = 30$ deg and a Simulated Altitude of 100,000 ft

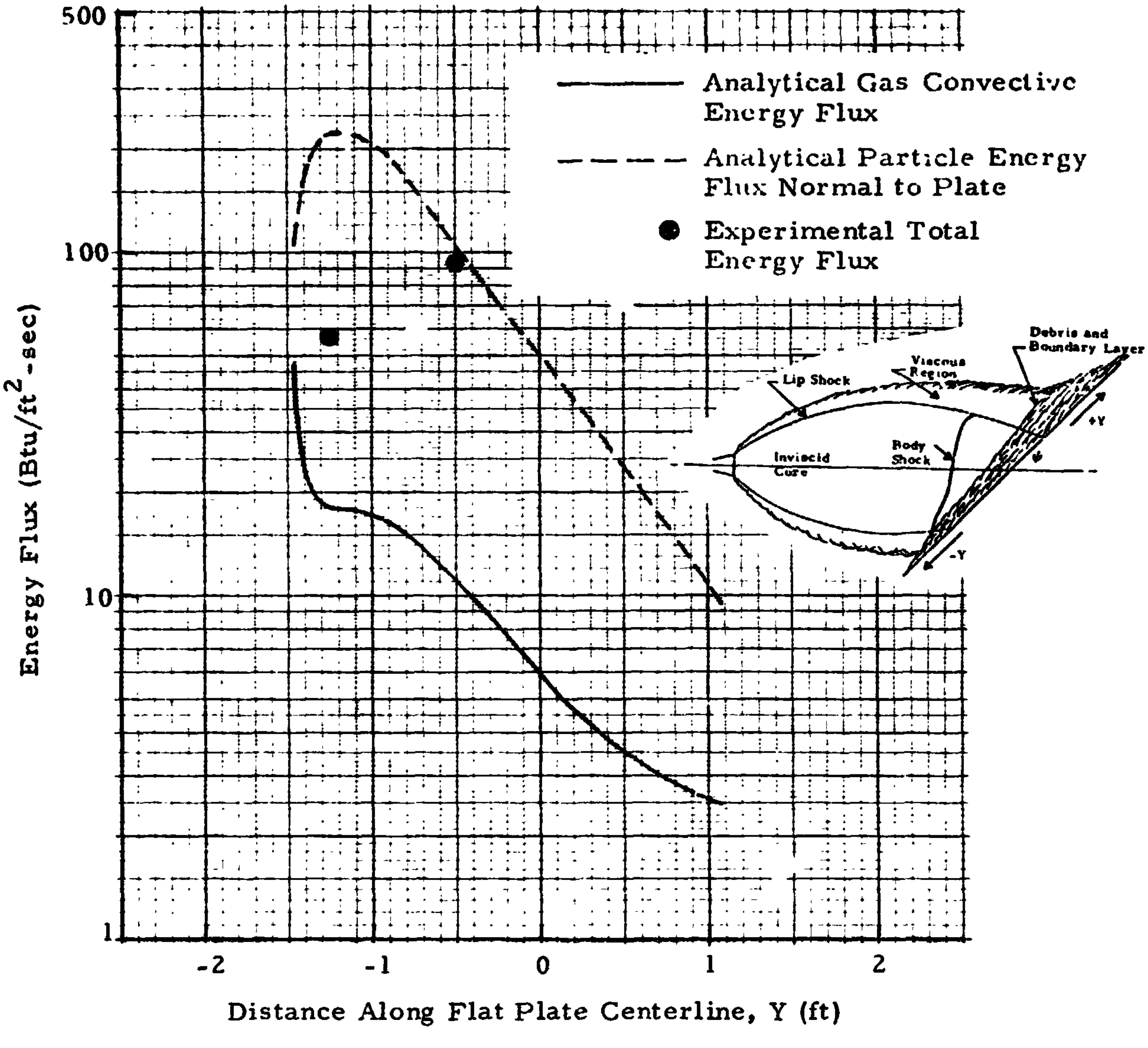

Fig. 89 - Comparison of Experimental and Analytical Energy Flux Along Centerline of Flat Plate for 15% Al Propellant at $x/D_{exit} = 20$, $\psi = 30$ deg and a Simulated Altitude of 100,000 ft

REPRODUCIBILITY OF THE ORIGINAL PAGE IS POOR

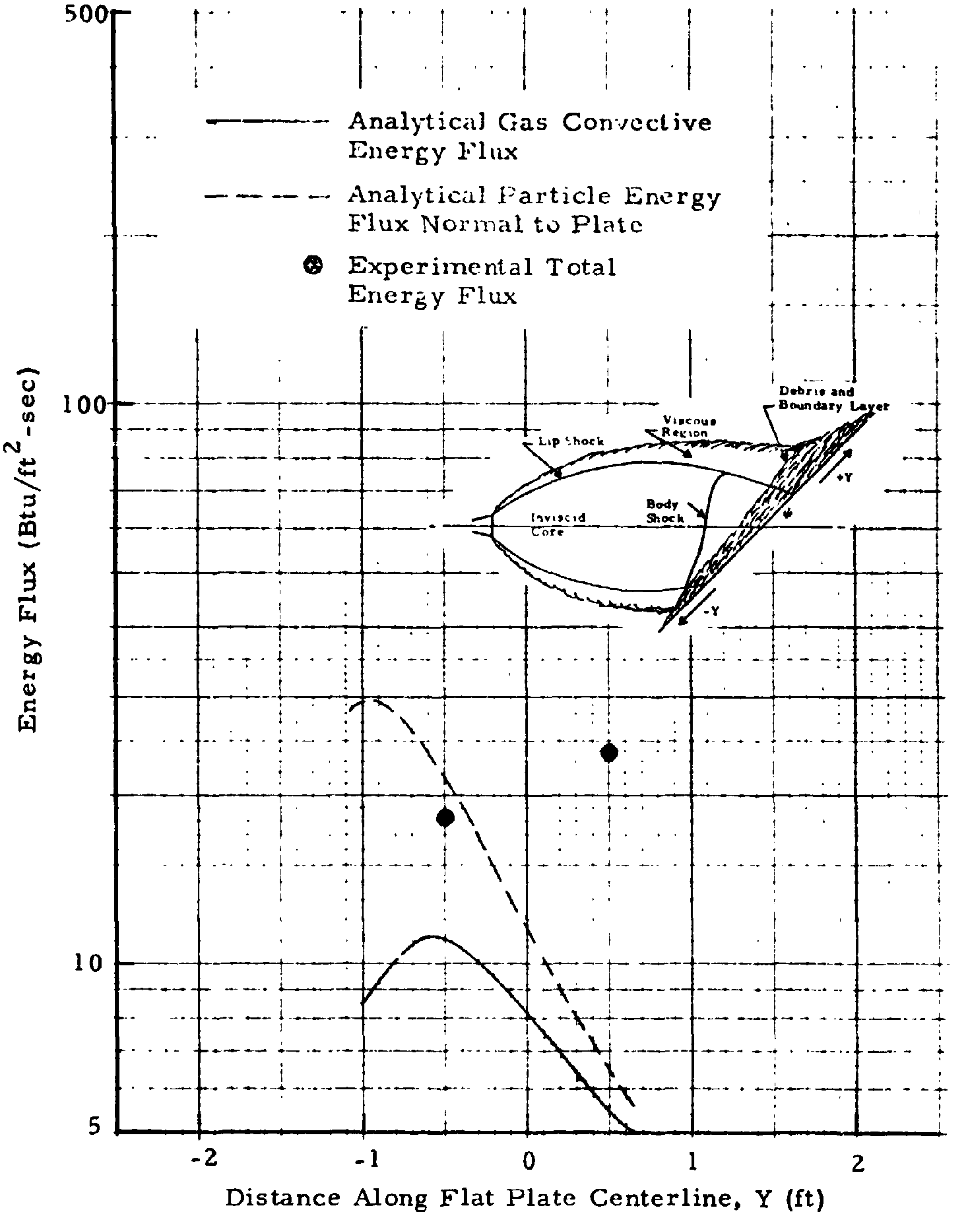

Fig. 90 - Comparison of Experimental and Analytical Energy Flux Along Centerline of Flat Plate for 2% Aℓ Propellant at $x/D_{exit} = 20$, $\psi = 45$ deg and a Simulated Altitude of 100,000 ft

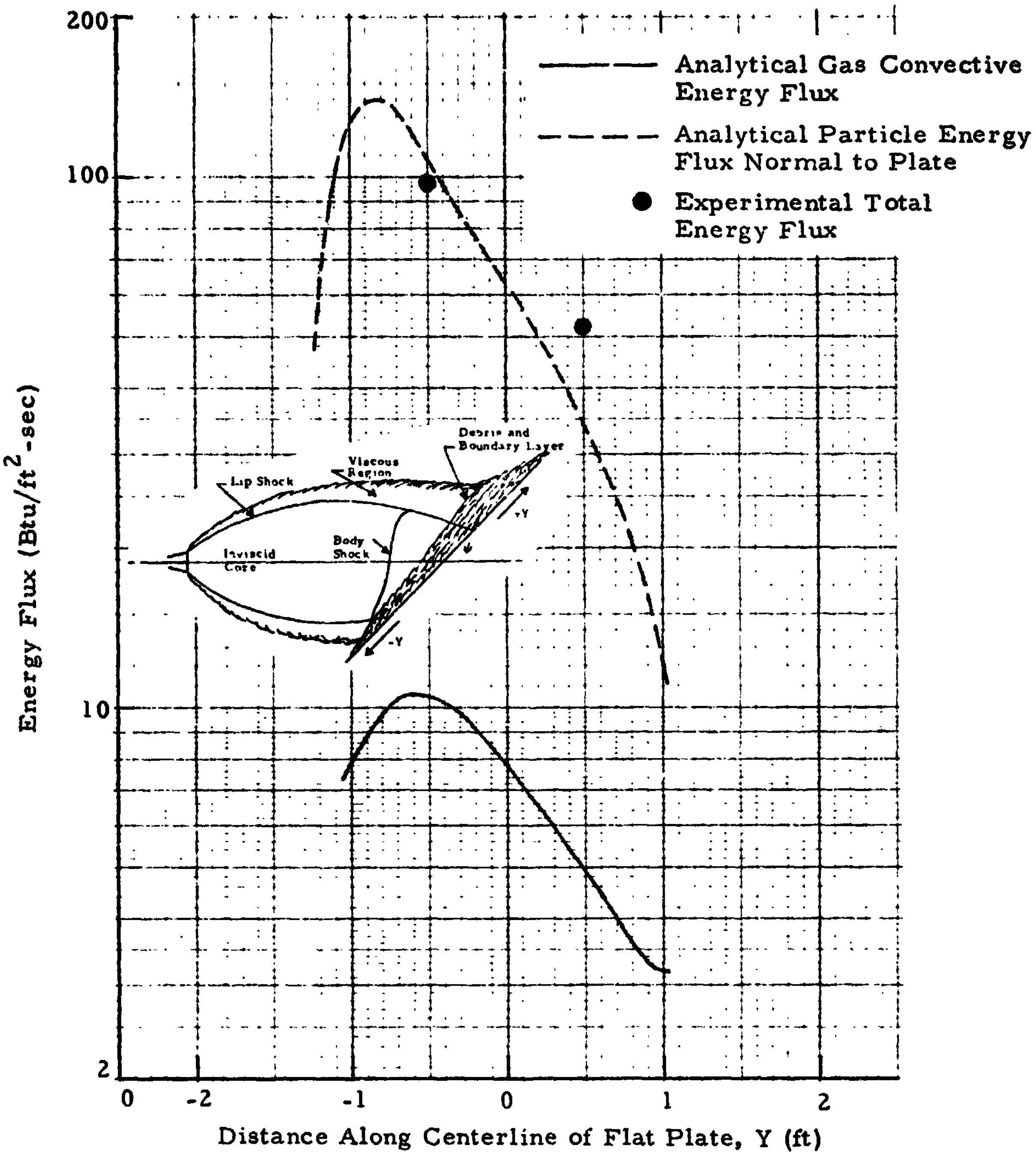

Fig. 91 - Comparison of Experimental and Analytical Energy Flux Along Centerline of Flat Plate for 10% Al Propellant at $x/D_{exit} = 20$, $\psi = 45$ deg, and a Simulated Altitude of 100,000 ft

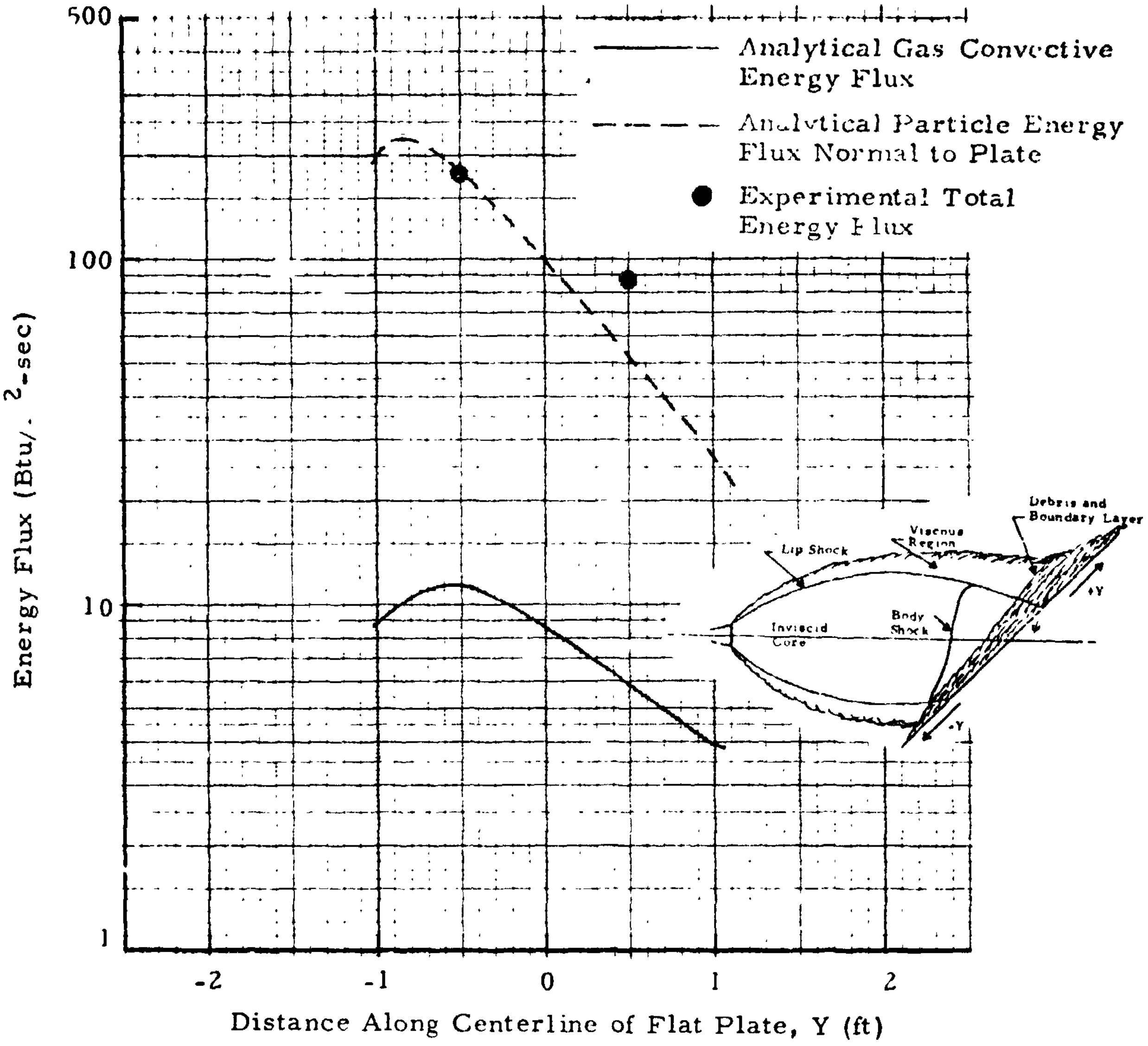

Fig. 92 - Comparison of Experimental and Analytical Energy Flux Along Centerline of Flat Plate for 15% Al Propellant at $x/D_{exit} = 20$, $\psi = 45$ deg, and a Simulated Altitude of 100,000 ft

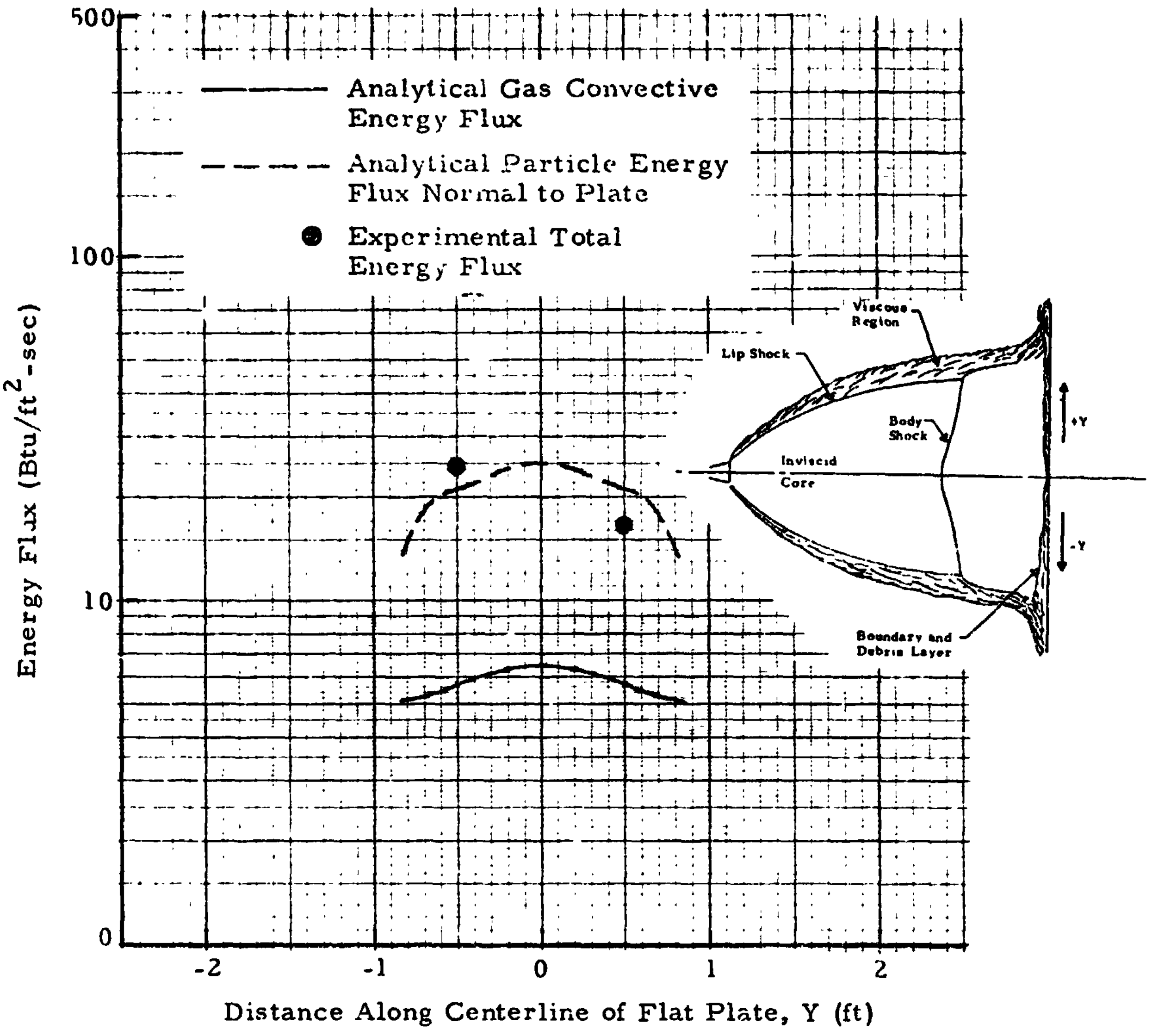

Fig. 93 - Comparison of Experimental and Analytical Energy Flux Along Centerline of Flat Plate for 2% Al Propellant at $x/D_{exit} = 20$, $\psi = 90$ deg, and a Simulated Altitude of 100,000 ft

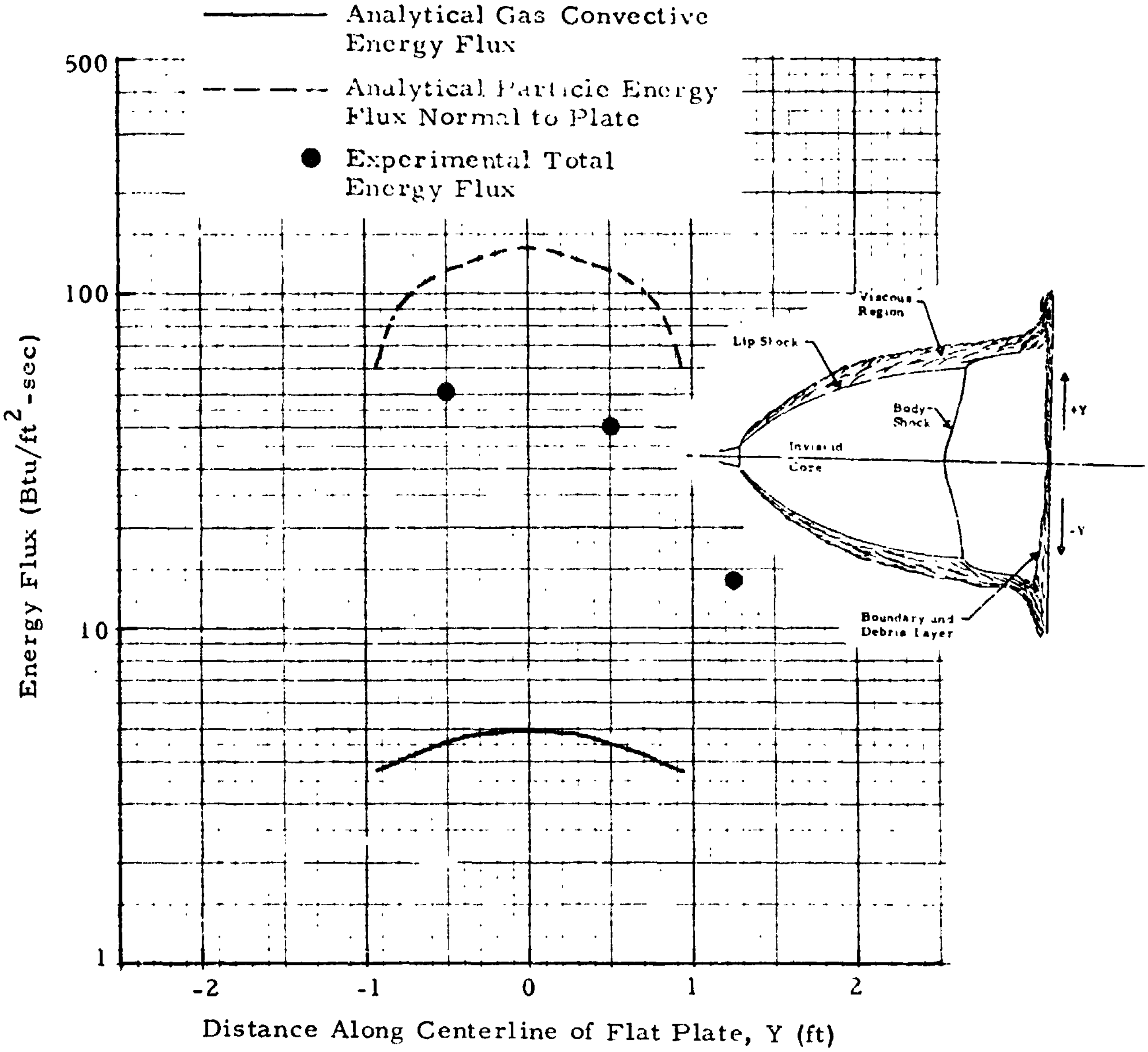

Fig. 94 - Comparison of Experimental and Analytical Energy Flux Along Centerline of Flat Plate for 10% Al Propellant at $x/D_{exit} = 20$, $\psi = 90$ deg, and a Simulated Altitude of 100,000 ft

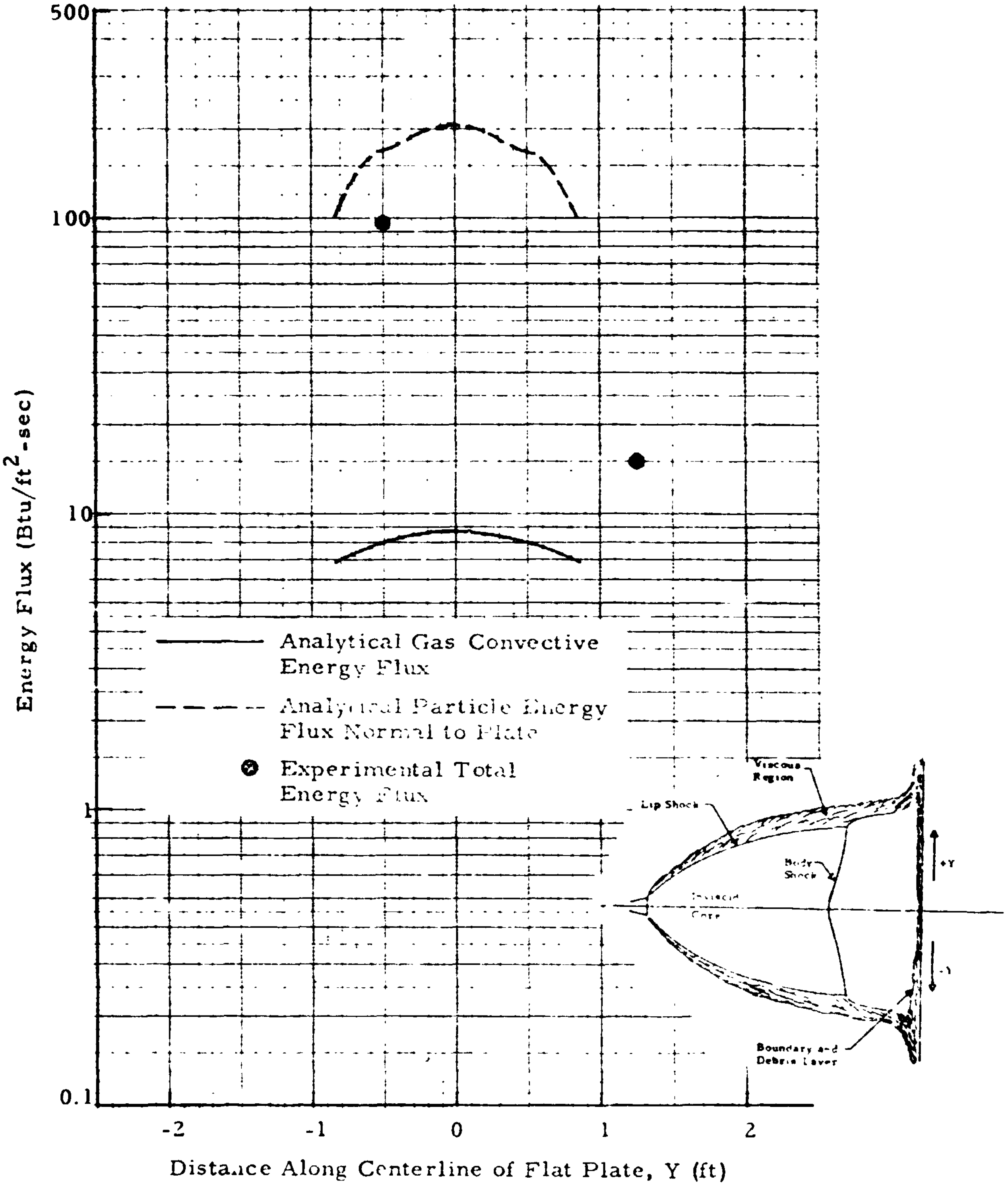

Fig. 95 - Comparison of Experimental and Analytical Energy Flux Along Centerline of Flat Plate for 15% $A\ell$ Propellant at $x/D_{exit} = 20$, $\psi = 90$ deg, and a Simulated Altitude of 100,000 ft